Public Health Impacts from Fires in Tropical Landscapes

Miriam E. Marlier

Submitted in partial fulfillment of the
requirements for the degree of
Doctor of Philosophy
in the Graduate School of Arts and Sciences

COLUMBIA UNIVERSITY

2014

ABSTRACT

Public Health Impacts from Fires in Tropical Landscapes

Miriam E. Marlier

Fires are the primary method of deforestation and agricultural management in the tropics, but associated emissions such as aerosols, ozone, and carbon monoxide can have negative impacts on ecosystems, climate, and public health. Recent advances in satellite monitoring of fire activity, including using thermal anomalies for active fire detections and burn scar mapping of post-fire effects, have offered an unprecedented level of detail in understanding the magnitude and extent of fire activity. This dissertation aims to quantify the human health impact across populations in tropical regions by determining which areas are the most susceptible to transported fire emissions and how this exposure varies over time. The following chapters can be used to highlight critical conservation regions, not only for conserving ecosystems for biodiversity and climate benefits, but also for protecting public health.

To address how fire emissions can affect regional populations, satellite observations of fire activity are combined with models of how tropical fire emissions are transported in the atmosphere. Satellites provide two primary pieces of information for this approach: 1) measurements of the distribution and magnitude of fire activity, and 2) categorization of fire types (such as agricultural burning or deforestation) by overlaying observed fire

patterns on land use maps. Atmospheric models perform the crucial step of simulating how emissions evolve and where they are transported after release into the atmosphere.

The following dissertation chapters are linked through exploration of fire emissions impacts from continental to local scales, including implementing fire emissions inventories into atmospheric models, quantifying population exposure to fire activity in Equatorial Asia, and projecting fire emissions associated with various future land use scenarios in Sumatra. Model estimates of aerosol concentrations are more influenced than trace gases by using finer temporal resolution fire emissions, due to interactions between emissions and modeled meteorology and transport. This in turn can impact air quality estimates by permitting higher peak concentrations. In addition, model results show that population exposure to fire emissions in Equatorial Asia is highly variable over time depending on the phase of the El Niño cycle; strong El Niño years can have fire contributions to fine particulate matter of up to 200 $\mu g/m^3$ near fire sources, corresponding to 200 additional days per year over the World Health Organization 50 $\mu g/m^3$ 24-hour fine particulate matter air quality target. These risks are not confined to people living near fire sources, but expose broad regional populations due to the atmospheric transport of emissions. Health impacts also depend on underlying fuel characteristics, with the future magnitude of Equatorial Asian fire emissions estimated to be strongly dependent on the level of protection given to fuel-rich peatswamp forests (contributing 33-48% of future emissions in the absence of protection). Collectively, these chapters emphasize variability in how tropical fire emissions affect regional population exposures to outdoor air pollution, and the need to consider the dependence of this public health effect on different fuel types and

year-to-year variations in climate. The results described in this dissertation quantify direct benefits of conservation for people living near fire areas.

TABLE OF CONTENTS

LIST OF TABLES

Chapter 2

Chapter 3

Chapter 4

LIST OF FIGURES

Chapter 2

Chapter 3

Chapter 4

ACKNOWLEDGMENTS

I would first like to thank my advisor, Dr. Ruth DeFries, for her guidance and patience during the process of researching and writing this dissertation. I have been incredibly fortunate to join her as a member of the DeFries lab and the GFED team during my time at Columbia, and the helpful discussions that I have had with these groups regarding this research and its applications. I am also grateful to my other advisors, especially Drs. Kevin Griffin, Drew Shindell, Patrick Kinney, and Apostolos Voulgarakis. Special thanks to Meha Jain, Amir Jina, Mary Heskel, Matthew Fagan, Marcia Macedo, and Su-Jen Roberts for their friendship, advice, and support during graduate school. Funding for this work was provided by the National Science Foundation Graduate Research Fellowship Program, Columbia, NASA, and the Rockefeller Foundation.

DEDICATION

I dedicate this work to my parents, John & Joyce Marlier, my sister, Jessica Campora, and my fiancé, Jeffrey Suer, whose encouragement made this possible.

CHAPTER ONE

Introduction

Global biomass burning emissions averaged 2 Pg C per year over the past decade [*van der Werf et al.*, 2010], with emissions from tropical deforestation and land use contributing approximately 1 Pg C per year [*Baccini et al.*, 2012]. Fire is often used during land management, as it is typically one of the cheapest and most effective methods for land clearing and maintenance. In some tropical countries, such as Indonesia, the magnitude of fire emissions is comparable to fossil fuels [*van der Werf et al.*, 2008]; accurate quantification of how emissions are distributed spatially and temporally is therefore crucial to estimate and understand the potential impacts. While conservation policies aimed at limiting fire-driven land use change have primarily focused on benefits for carbon storage and biodiversity protection, the overall value of protecting natural ecosystems can benefit from including direct human impacts, such as how fire emissions jeopardize public health. In addition, while the negative consequences of exposure to indoor biomass burning are comparatively better understood [*Lim et al.*, 2012], less is known about the magnitude and variability of the public health response due to landscape fires. By asking which populations in tropical regions are the most susceptible to fire emissions exposure and how this varies over time, my dissertation helps to fill in this knowledge gap and presents potential policy options for protecting future public health.

Similar to industrial sources, fires release a variety of emissions products including carbon dioxide (CO_2), ozone (O_3) precursors such as carbon monoxide (CO), nitrous oxides

(NO_x) and volatile organic compounds (VOCs), sulfur-containing compounds, and particulates, such as black carbon (BC) and organic carbon (OC) [*Andreae and Merlet*, 2001]. These different emissions can cause a variety of effects, including contributing to air quality degradation, altering the oxidizing capacity of the atmosphere, changing atmospheric heating profiles, blocking radiation from the surface, and altering the ratio of direct to diffuse radiation (with subsequent effects on the hydrological cycle and ecosystem functioning) [*Crutzen and Andreae*, 1990]. The following chapters describe how to measure the various air quality and public health impacts of biomass burning in tropical regions (Chapters 2 and 3), as well as projections of future fire emissions from land use change for a case study in Indonesia (Chapter 4).

Biomass burning estimates have greatly improved with recent satellite advances, which permit repeating, near-global coverage of fire activity. My dissertation utilizes a satellite-based estimate of fire emissions called the Global Fire Emissions Database (GFED), which is available since 1997 at 0.5° × 0.5° spatial resolution. GFED combines multiple satellite detections of active fires, which are based on thermal detection anomalies, with burned area observations, which measure changes in surface reflectance [*Giglio et al.*, 2010; *van der Werf et al.*, 2010]. This information drives a biogeochemical model that estimates fuel loads, combustion completeness, and speciated emissions. GFED emissions vary by fuel type, with fine grassy fuels emitting more oxidized species (such as CO_2) and dense fuels like woody biomass and peat emitting more reduced forms (such as CO and methane (CH_4)) [*van der Werf et al.*, 2010]. We account for the transport of emissions from source regions to exposed populations with atmospheric models that simulate the physical and chemical mechanisms that affect atmospheric constituents, such as wind, precipitation,

and chemical reactions. In the following chapters, we use GFED emissions as an input dataset for two different modeling systems: a chemistry-composition model, GISS-E2-PUCCINI [*Shindell et al.*, 2013a], and a chemical transport model, GEOS-Chem [*Bey et al.*, 2001].

Simulations of fire emissions in the atmosphere depend on many factors, and in Chapter 2, I question how the temporal resolution of the emissions inventories themselves could alter interactions between fire emissions and physical parameters in the models, which often operate at a much finer temporal resolution. For example, while GFED is available with the same bulk monthly emissions totals at a monthly, daily, and 3-hourly resolution from 2001-onward (monthly only from 1997-2001), these different temporal resolutions could have different interactions with the modeled precipitation or wind [*Mu et al.*, 2011]. Chapter 2 describes how using monthly versus daily resolution fire emissions alters simulations of atmospheric chemistry, air quality and climate in the tropics, and how this differs among trace gases and aerosols over a five-year study period from 2005-2009. We find that simulations of aerosols are more dependent on this temporal resolution of fire emissions than trace gases, and that this changes model estimates of atmospheric concentrations and how fire emissions degrade air quality.

In Chapters 3 and 4, we focus our analysis to fire activity in Equatorial Asia, which can make large contributions to global fire emission totals. This region is characterized by strong interannual variability in fire activity that is linked to changes in the El Niño-Southern Oscillation (ENSO); emissions during the 1997 El Niño were 1069 Tg C per year but only 21 Tg C per year during the 2000 La Niña [*van der Werf et al.*, 2010]. In addition, Equatorial Asia has aboveground biomass stored in wet tropical forests and rich

belowground carbon stocks in peatlands that are susceptible to fire after drainage. Due to these high fuel loads, Equatorial Asia on average represents only 2.5% of global burned area but 15% of global carbon emissions (and 36% of CH_4, a reduced form of carbon that is oxidized in the atmosphere to CO_2) [*van der Werf et al.*, 2010]. Chapter 3 estimates the public health impact of fire emissions in Equatorial Asia from 1997-2008. In order to include the 1997 El Niño event, we use the monthly temporal resolution GFED3 emissions dataset (daily resolution emissions are only available since 2001) and transport emissions with the two different atmospheric models described above, GISS-E2-PUCCINI and GEOS-Chem. We quantify exceedances over World Health Organization air quality guidelines and adult cause-specific mortality (due to cardiovascular disease and lung cancer) for fine particulate matter ($PM_{2.5}$) and O_3. Although fire activity is predominately from the Indonesian islands of Sumatra and Kalimantan (Indonesian Borneo), we demonstrate that the public health impact is experienced away from fire sources due to atmospheric transport. We also observe a link between mortality attributable to fire emissions exposure and the ENSO cycle.

Chapter 4 describes fire emissions associated with potential land use change trajectories for Indonesia over the coming decades, which is expected to have continued rapid expansion of oil palm and timber plantations in the absence of significant conservation interventions [*Miettinen et al.*, 2012a]. This work is part of a broader collaborative effort that will ultimately quantify the public health impact associated with future fire emissions within the Southeast Asian regional "airshed." We use spatially explicit models of land use change that were created by the World Wildlife Fund (WWF), including projections for baseline conditions, peatswamp protection, high rates of oil palm

plantation expansion, and a green vision of sustainable development and ecosystem conservation for Sumatra. To estimate future emissions, we first overlay GFED fire emissions over the past decade with observed land use change, which helps us to identify the specific land use transitions that are contributing to emissions, and how this varies with meteorological conditions. This relationship is then used to estimate future emissions associated with future land use change scenarios. With this approach, we find that emissions from fires in peatswamp forests dominate the total emissions for Sumatra unless these areas are protected from conversion and fires are blocked from highly susceptible degraded lands.

My dissertation brings together a multidisciplinary analysis of the health impacts of biomass burning emissions by integrating the fields of remote sensing, atmospheric science, public health, and ecology. Opposed to the sometimes more intangible impacts of climate change, the public health effects of exposure to fire emissions represent a direct impact of environmental change. The following chapters describe the critical importance of considering how tropical fire emissions contribute to the public health burden due to outdoor air pollution.

CHAPTER TWO

The role of temporal evolution in modeling atmospheric emissions from tropical fires

Miriam E. Marlier, Apostolos Voulgarakis, Drew T. Shindell, Greg Faluvegi, Candise L. Henry, and James T. Randerson

In review, submitted to *Atmospheric Environment* on October 7th, 2013.

Abstract

Fire emissions associated with tropical land use change and maintenance influence atmospheric composition, air quality, and climate. In this study, we explore the effects of representing fire emissions at daily versus monthly resolution in a global composition-climate model. We find that simulations of aerosols are impacted more by the temporal resolution of fire emissions than trace gases such as carbon monoxide or ozone. Daily-resolved datasets concentrate emissions from fire events over shorter time periods and allow them to more realistically interact with model meteorology, reducing how often emissions are concurrently released with precipitation events and in turn increasing peak aerosol concentrations. The magnitude of this effect varies across tropical ecosystem types, ranging from smaller changes in modeling the low intensity, frequent burning typical of savanna ecosystems to larger differences when modeling the short-term, intense fires that characterize deforestation events. The utility of modeling fire emissions at a daily resolution also depends on the application, such as modeling exceedances of particulate matter concentrations over air quality guidelines or simulating regional atmospheric heating patterns.

1. Introduction

Fires are widely used throughout the tropics to create and maintain areas for agricultural systems, but are also significant contributors to atmospheric trace gas and aerosol concentrations [*Andreae and Merlet*, 2001]. Emissions associated with deforestation averaged 1 Pg carbon per year over the past decade [*Baccini et al.*, 2012], while also adding to atmospheric ozone (O_3) precursors such as CO, NO_x and VOCs, sulfur-

containing compounds, and particulates [*Langmann et al.*, 2009]. In addition to the diversity in the type of emissions, the timing and magnitude of fire activity also varies interannually and by biome. This suggests that representing fire emissions at different temporal resolutions in atmospheric models could alter interactions between emissions and atmospheric chemistry and transport, which also vary significantly on several timescales.

The tropics comprise a critical region for global fire activity, but have varying fire behavior characteristics [*van der Werf et al.*, 2010]. Frequent but lower intensity fires are typical in savanna areas in Africa and South America [*van der Werf et al.*, 2010]. Fire emissions from Southern Hemisphere Africa are dominated by savanna burning, but the Amazon includes a mix of savanna and deforestation fires, which leads to higher rates of fuel consumption and fewer fire days per year (when emissions are aggregated at a 0.5° spatial resolution). Equatorial Asia has even fewer average fire days per year and higher daily rates of fuel consumption [*Mu et al.*, 2011]. On longer timescales, carbon-rich Equatorial Asian peatland forest fires have higher interannual variability than other biomes [*van der Werf et al.*, 2010], with large pulses of emissions during El Niño droughts [*van der Werf et al.*, 2008]. These regional differences in emissions characteristics suggest that fire emissions inventories with monthly resolution may be able to adequately resolve dominant modes of variability of fire behavior in certain biomes, but could be insufficient in other areas. An important challenge for the atmospheric sciences community is to understand how this variability in fire behavior influences chemistry, radiative forcing, and air quality.

Monthly global gridded fire emissions inventories typically combine information from satellite observations of burned area, active fire detections, underlying vegetation

characteristics, and meteorology. One example is the Global Fire Emissions Database version 3 (GFED3), which is available at a monthly resolution from 1997-2011 [*van der Werf et al.*, 2010]. From November 2000 onwards, it detects changes in 500-m Moderate Resolution Imaging Spectroradiometer (MODIS) surface reflectance and 1-km MODIS active fires to inform an automated hybrid burned area mapping algorithm [*Giglio et al.*, 2009]. Before 2000, active fire detections from Tropical Rainfall Measuring Mission (TRMM) Visible and Infrared Scanner (VIRS) and the Along-Track Scanning Radiometer (ATSR) are used to estimate burned area by means of a regression with MODIS burned area during overlap periods, which necessitates the dataset's monthly resolution [*Giglio et al.*, 2010]. Duncan et al. [2003] used active fire data from ATSR and the Advanced Very High Resolution Radiometer (AVHRR) to estimate seasonal fire variability, with the Total Ozone Mapping Spectrometer (TOMS) Aerosol Index serving as a proxy for interannual variability in selected regions, which then scaled an existing biomass burning inventory. While these datasets capture important information on seasonal and interannual variability in fire activity, they may have important limitations when implemented into modeling systems which otherwise operate at sub-daily increments.

Recognizing these potential limitations, several fire emissions inventories at daily or sub-daily resolution are also available, using satellite active fire detections to represent emissions at a finer temporal resolution. Mu et al. [2011] recently applied active fire counts from MODIS and the Geostationary Operational Environmental Satellite (GOES) Wildfire Automated Biomass Burning Algorithm (WF_ABBA) to create daily and 3-hourly emissions inventories, respectively, from the original GFED3 monthly dataset. Heald et al. [2003] applied AVHRR active fire observations to the Duncan et al. [2003] inventory to create a

daily emissions dataset for early 2001. The Fire Inventory from NCAR (FINN) is a daily 1-km global dataset of trace gas and particulate emissions from fires, available from 2005-10 [*Wiedinmyer et al.*, 2011]. FINN primarily uses MODIS active fire detections, an assumed burned area per detection (to allow the product to be released close to real-time), and MODIS land cover types to estimate fuel loadings. Fire Locating and Modeling of Burning Emissions (FLAMBE) combines GOES WF_ABBA, near real-time MODIS active fire products, and 1-km AVHRR land cover maps to create hourly emissions inventories, from 2005 onwards [*Reid et al.*, 2009]. Kaiser et al. [2012] developed the 0.5 × 0.5° Global Fire Assimilation System (GFASv1.0), available from 2003, by calculating biomass burning emissions based on MODIS fire radiative power and land cover-specific combustion factors derived from the GFED3 emissions inventory.

Many daily or sub-daily emissions products rely on MODIS active fire detections and are therefore only available since late 2002, when both Terra and Aqua were in operation together. Therefore, for modeling studies before the MODIS era, monthly inventories may still be the only option. Some chemical transport models are moving towards using daily or hourly fire emissions [*Mu et al.*, 2011], although most global composition-climate models currently implement monthly resolution emissions [*Lee et al.*, 2013]. It remains unclear which aspects of atmospheric modeling are most sensitive to this choice of temporal resolution, because in previous studies, using finer temporal resolution emissions over coarser resolution datasets have offered variable improvements when compared with observations. Model simulations focusing on CO have found improvements with daily over monthly fire emissions but not sub-daily resolution emissions [*Mu et al.*, 2011], monthly over climatological, but not daily [*Heald et al.*, 2003], and 8-day instead of monthly, but not

diurnal [*Chen et al.*, 2009]. Simulations of shorter-lived species like NO_2 improve from sub-daily emissions that capture the afternoon peak of biomass burning emissions [*Boersma et al.*, 2008]. In boreal North America, Chen et al. [2009] found that aerosols were more sensitive to using 8-day versus monthly resolution emissions than was found with CO (also without further improvements with diurnal resolution). In areas such as Singapore, where biomass burning aerosol transport from Indonesia is highly variable over the fire season, both with respect to shifts in geographic patterns of burning and atmospheric transport patterns, detailed temporal resolution of fire emissions inventories may improve modeled regional aerosol concentrations [*Atwood et al.*, 2013]. Modeling the interactions between smoke aerosols by changing absorption patterns of radiation can also vary strongly on sub-daily timescales [*Wang and Christopher*, 2006; *Wu et al.*, 2011].

In this study, we examine the sensitivity of multiple endpoints to using daily and monthly resolution fire emissions: modeling trace gases and aerosols, assessing air quality and public health effects, and estimating climate impacts. We hypothesize that changing from monthly to daily fire emissions will: 1) produce a varied response throughout the tropics, depending on biome-specific fire behavior (for example, continuous low intensity fires would lead to smaller atmospheric differences in savanna regions), 2) allow for higher peak concentrations since short-lived fire events can be concentrated over several days and not averaged over a month, and 3) more realistically synchronize emissions with meteorology, with fires predominately occurring on sunny, precipitation-free days, which would lower wet deposition of aerosols and could increase the speed of some chemical reactions. Section 2 describes the model framework and observational datasets; Section 3

presents our results for atmospheric composition, air quality, and radiative forcing; Section 4 describes our conclusions.

2.1 Materials and Methods

2.1.1 Model Set-up

Baseline monthly fire emissions estimates were from GFED3, which combines surface reflectance and active fire detections from several satellites to detect the spatiotemporal variability of burned area [*Giglio et al.*, 2010]. This drives a biogeochemical model that estimates fuel loads, combustion completeness, and emissions [*van der Werf et al.*, 2010]. GFED3 is available for 1997 onwards at 0.5° × 0.5° horizontal resolution. This dataset comprised the fire input for our monthly fire emissions (MF) run.

To isolate the influence of the temporal resolution of fire emissions instead of variations among fire emissions inventories, we used a daily emissions dataset with the same bulk total emissions as the monthly GFED3 dataset. Mu et al. [2011] used MODIS active fire detections aboard the Terra and Aqua satellites to parse the monthly GFED3 emissions to a daily resolution. Due to gaps in satellite overpasses in the tropics, they applied a three day smoothing filter between 25°N and 25°S. This dataset comprised our daily fire emissions (DF) run. Both fire emissions datasets are publicly available (http://www.globalfiredata.org).

Simulations were run with GISS-E2-PUCCINI, which is the latest version of the NASA GISS ModelE climate model, including interactive chemistry and aerosols [*Shindell et al.*, 2013a]. Following a two year spin-up, it was run at 2° × 2.5° resolution with 40 vertical

layers from 2005-2009. We conducted three simulations: 1) MF, 2) DF, and 3) NF (no fire emissions).

Our simulations included interactive constituents in the PUCCINI model for chemistry, aerosols (sulfate, carbonaceous, nitrate, dust and sea salt), and an aerosol indirect effect parameterization [*Koch et al.*, 2006; *Shindell et al.*, 2013a]. GFED3 emissions were mixed uniformly through the boundary layer. Monthly emissions were linearly interpolated to daily values for the MF simulation while the daily fractions from the Mu et al. [2011] product were used for the DF simulation. Annually and monthly-varying GFED3 emissions were used for CO, ammonia, black carbon (BC), organic carbon (OC), sulfur dioxide, non-methane hydrocarbons, and NO_x. Present-day anthropogenic emissions were re-gridded to 2° × 2.5° spatial resolution based on Lamarque et al. [2010], which was produced to provide input to models being run in support of the IPCC Fifth Assessment Report (AR5). Methane in the lowest model layer was kept to observed values for each year and lightning NO_x was generated internally based on an updated version of Price et al. [1997]. Climate-sensitive isoprene emissions were based on Guenther et al. [1995; 2006]; vegetation alkene and paraffin emissions from the GEIA dataset are based on Guenther et al. [1995]. Model winds were linearly relaxed towards reanalysis based on meteorological observations [*Rienecker et al.*, 2011]. Sea-surface temperatures and sea ice were from monthly observational datasets [*Rayner et al.*, 2003].

We focused on several key trace gases and aerosol species to illustrate the changes between the DF and MF simulations. Trace gases included CO, O_3, and OH to understand how the model simulates atmospheric composition; both O_3 and CO are major pollutants, while O_3 and OH are also directly and indirectly important, respectively, to climate. For

aerosols, we focused on BC and OC, which are the main components of particulate matter to which fire emissions contribute [*Andreae and Merlet*, 2001].

2.1.2 Ground and Satellite Observations

We compared model output with ground-based (Table 1) and satellite measurements of O_3, CO, and aerosol optical depth (AOD). Observations were generally selected within primary tropical fire regions as defined in by GFED [*van der Werf et al.*, 2010]: Southern Hemisphere South America, Southern Hemisphere Africa, and Equatorial Asia, although we expanded the regions slightly depending on station coverage. Of the 14 GFED regions, these three contributed more than 50% of global emissions over 2005-2009 [*van der Werf et al.*, 2010].

The World Data Centre for Greenhouse Gases (WDCGG) maintains station trace gas observations (http://ds.data.jma.go.jp/gmd/wdcgg/). We used 24-hour averages of surface O_3 and CO concentrations for comparison with surface model output. As described in Table 1, CO and/or O_3 data were available from 8 stations for variable time periods within 2005-2009.

NASA's AErosol RObotic NETwork (AERONET) is a global ground-based sun photometer network (http://aeronet.gsfc.nasa.gov) [*Holben et al.*, 1998]. Column AOD is calculated from direct solar radiation measurements. We used Version 2, Level 2.0 24-hour average data, which is the highest quality screened product available. There were 24 available stations.

We also compared modeled AOD with MODIS and Multi-angle Imaging SpectroRadiometer (MISR) daily satellite AOD products. We averaged modeled

instantaneous AOD values for 12pm and 3pm to correspond with the 1:30pm Aqua satellite overpass for MODIS and 9am to 12pm to correspond with the 10:30am Terra satellite overpass for MISR. AOD retrievals from MODIS take advantage of a wide spectral range, daily coverage of the globe, and high spatial resolution. We used the daily MODIS 1° × 1° Level 3, Collection 5 monthly AOD (MOD08 D3) product (http://modis.gsfc.nasa.gov). MISR (http://www-misr.jpl.nasa.gov) simultaneously observes the Earth at nine different angles and four spectral bands, with global coverage every nine days at the equator. We used the gridded 0.5° × 0.5° Level 3 daily AOD product (MIL3DAE) from the green (555 nm) band.

2.1.3 Air Quality

The World Health Organization (WHO) combines results from epidemiological studies on the public health risks of air pollutants and publishes air quality guidelines [*World Health Organization*, 2006]. These guidelines serve as goals for countries to improve air quality, and are published along with higher interim targets levels (ITs) that have additional expected health risks. We examined how modeling population exposure in the tropics changed with DF versus MF by testing changes in peak concentrations through exceedances over 24-hour $PM_{2.5}$ and 8-hour maximum O_3 ITs.

Annual cardiovascular disease (CVD) mortality burdens were estimated for exposure to fire $PM_{2.5}$ with a power-law relationship that describes how relative risk (RR) changes over a baseline value of 1:

(1) $RR=1+ \alpha(I*C)^{\beta}$

We used published values for α and β from a reanalysis of studies that include exposure to ambient air pollution, second-hand smoke, and cigarette smoke. For CVD disease, α=0.2685

and β=0.2730 [*Pope et al.*, 2011]. Annual average total mass $PM_{2.5}$ surface concentrations were used for (C), assuming a constant average inhalation rate (I) of 18 m^3/day to convert to $PM_{2.5}$ dose (in mg). The attributable fraction (AF) and annual mortality (ΔM) were estimated by:

(2) $AF = (RR-1)/RR$

(3) $\Delta M_{annual} = M_b * P * (AF_{fire} - AF_{nofire})$

where the average annual baseline mortality rate (M_b) was calculated from adult deaths due to cardiovascular disease [*Ostro*, 2004], averaged over the countries within each region [*World Health Organization, Department of Measurement and Health Information*, 2011]. The fraction of people over 30 years was from the UN Population Division [*UN*, 2011] and baseline population was from CIESIN's Gridded Population of the World version 3 for 2005 [*CIESIN*, 2005a] and Future Estimates for 2010 [*CIESIN*, 2005b]; both the adult fraction and population were linearly interpolated from 5 yearly to annual estimates.

2.1.4 Radiative Forcing

To evaluate the potential climate implications of our results, we calculated differences between surface and top-of-atmosphere (TOA) instantaneous long-wave and shortwave radiative forcing for several constituents affected by biomass burning. Radiative forcing, in W/m^2, was evaluated for BC, OC, and O_3 in each simulation, as these are the most radiatively active species that are affected by fires. Radiative forcing was calculated online as an average over time during the simulations; calculations were performed twice at each point in time, with the only difference in the two calculations being the constituent field (e.g. BC, O_3, etc).

3. Results

3.1 Atmospheric Composition

3.1.1 Aerosols

Figure 1a shows the difference in the 2005-09 average of surface carbonaceous aerosols (BC+OC) between the DF and MF simulations (Fig. S1 shows relative differences). There was a mixed response in South America (within +/-10%), with increases from the DF simulation in western and interior regions of the Amazon, and decreases across savanna regions in the south and east. In Africa, daily emissions increased surface concentrations across tropical forests in the Congo basin, but decreased concentrations closer to source regions in savannas north and south of the equator (within +/-10%). DF also led to increased transport of aerosols from Africa to the tropical North Atlantic (+20%). In Equatorial Asia, the differences were the strongest in Borneo and to the north of Borneo (up to +30%), while staying within -10% over source regions in Sumatra. In general, the spatial patterns across the three continents were consistent with reduced surface concentrations near source regions and enhanced long-range transport of aerosols into more remote regions.

We compared modeled aerosol concentrations with ground and satellite observations. Linear correlations (R^2) between 24-hour model and AERONET AOD are in Table 2 and correlations generally improved with DF over MF. It is important to note that AERONET stations had variable temporal coverage over 2005-09 and were located at a range of distances from fire activity. When we limited results to sites that had correlations between modeled concentrations and observations that were significant at the 0.05 level

and with R^2>0.1 (for both simulations), there were improvements in 5 out of 6 South American stations, 4 out of 5 African stations, and 0 out of 2 Equatorial Asian stations (for DF versus MF). The NF correlations suggested how much fires contribute to AOD at each site. When fire emissions were excluded (NF), the statistically significant stations with R^2>0.1 decreased on average from R^2 of 0.47 to 0.07 for DF to NF for South America, from 0.28 to 0.12 for Africa, and from 0.13 to 0.22 for Equatorial Asia. Aside from fire emissions, other emissions were not resolved at the daily scale. This can explain some of the low observed correlations, since grid cells in or near cities, for example, could have clear differences in weekday versus weekend emissions due to changes in vehicle and industry emissions. In addition, we compared point measurements with large model grid boxes.

We isolated single grid cells near high fire activity (determined by 5-year average carbonaceous fire aerosol concentrations) to compare daily model with MODIS and MISR satellite AOD (Fig. 2). These locations also corresponded to AERONET stations. For South America, at the Cuiba Miranda station, the DF simulations increased the R^2 from 0.49 to 0.56 for MISR (relative to MF), from 0.21 to 0.25 for MODIS, and from 0.45 to 0.72 for AERONET. For the Mongu station in Africa, there was improvement in the DF simulations from 0.21 to 0.25 for MISR, from 0.11 to 0.16 for MODIS, and from 0.39 to 0.45 for AERONET. Marbel University, in Equatorial Asia, showed no correlations between either satellite and model data. The model simulations of the AERONET AOD data improved from 0.42 to 0.64 for MF to DF, based on only one month of data. Overall, we only saw clear improvements with MISR data at Cuiba Miranda. The differences between MISR and MODIS could be related to the satellite products' spatial resolution (0.5° for MISR vs. 1.0° for

MODIS) or the order of magnitude difference in available daily data for the three locations (430 days for MISR versus 3,329 days for MODIS).

To elucidate mechanisms driving differences in aerosol concentrations between DF and MF, we investigated whether daily fire emissions are better synchronized with model meteorology than monthly emissions, which, for example, would limit how often fire emissions are released during precipitation events. Note that there were not substantial changes in monthly precipitation totals between DF and MF, due to the meteorology being constrained. Figure 3 shows the distribution of monthly wet deposition, normalized by total mass concentrations, for BC emitted from biomass burning. The features for OC (not shown) are very similar. All three tropical GFED regions (top row) and smaller analysis regions (bottom row) have more months with lower wet deposition in DF compared to MF (negative values); this effect is most pronounced in Equatorial Asia. These results suggest: 1) the DF run may simulate more intuitive fire emissions transport and removal processes, with increased fire emissions occurring on low precipitation days, leading to reduced wet removal of aerosol particles from the atmosphere and hence longer lifetimes (Tables 3+4), and 2) the response to emissions from certain fire types, such as in tropical peat forests in Equatorial Asia, are more strongly influenced by the temporal resolution of fire emissions. This is partly reflected in the higher DF concentrations found in much of the region, though some parts of it (most of Sumatra) feature decreased DF concentrations (Fig. 1).

3.1.2 Trace Gases

The difference between DF and MF 2005-09 average surface CO exhibited similar spatial patterns to the carbonaceous aerosol distribution (Fig. 1b). Since aerosols and CO

do not share common underlying chemistry or removal mechanisms, the distributions suggest transport-related differences between DF and MF. In boreal North America, Chen et al. [2009] found that using fire emissions finer than monthly resolution tended to increase long-range transport while decreasing both CO and aerosol concentrations near source regions. The changes in 5-year average surface CO between DF and MF were generally within 10%, with a maximum approaching +20% in DF over Borneo and Singapore (Fig. S1). We did not find significant changes in the global CO lifetime or transport (Tables 3+4).

There were not significant improvements in CO comparisons with ground observations, except for Bukit Koto Tabang in Equatorial Asia (Table 2). Due to their distance from fire sources, some stations (Cape Point and Ushuaia) also had little improvement over NF. We also performed comparisons with TES satellite CO and O_3 observations. However, because free tropospheric CO and O_3 differences between the two simulations are minimal and applying the TES averaging kernels (e.g. see Voulgarakis et al. [2011]) provides a weighting towards the middle to upper troposphere, there were undetectable differences at multiple levels in the troposphere between the two simulations when compared to TES.

Surface O_3 and OH concentrations largely decreased in all three tropical GFED regions (Fig. 1c+d, and S1). There was less than a 10% decrease in O_3 for the DF versus MF run, and up to 15% decrease for OH. Table 2 shows the negligible effect of the fire emissions dataset on modeled O_3 correlations with station observations. As with CO, several stations did not see any improvement compared to NF. There were negligible changes on O_3 lifetime and transport (Tables 3+4). OH concentrations are determined by O_3 levels, but also by water vapor availability and by O_3 photolysis rates [*Voulgarakis et al.*,

2013]. Here, the two latter factors either did not change significantly (water vapor) or changed towards the opposite direction (photolysis rates), suggesting that O_3 decreases drove OH changes. The O_3 decrease may be driven by faster O_3 photolysis rates at low altitudes, but the photolysis changes were small compared with O_3 concentration changes. With aerosol emissions concentrated over shorter time periods in DF, there could be an increase in photolysis rates during non-fire conditions, with less smoke pollution blocking radiation from reaching the surface. Another possible contributing factor is that with MF, fire emissions are released during storms with lightning emissions (including O_3 precursors), causing increased O_3 production. We found that daily aerosol emissions were less affected by wet deposition, which would support fewer fire emissions concurrently emitted during lightning events. This requires further investigation.

3.2 Air Quality

Exceedances over WHO ITs showed additional days with higher $PM_{2.5}$ concentrations in the DF versus MF simulations. MF emissions are averaged over an entire month even if fires occur on a few days, limiting model simulations of extreme concentrations. Figure 4 (top row) shows the distribution of exceedance days for 2005-09 over WHO IT-3 (75 μg/m^3 24-hour $PM_{2.5}$) for each of the three regions of high fire activity, which are delineated by red boxes in Figure 2a. The largest differences between the two runs were found at high $PM_{2.5}$ concentrations (> 100 μg/m^3), as shown in South America (Fig. 5). The differences were less pronounced for the 240 μg/m^3 O_3 WHO IT and showed some slight declines with DF (Fig. 4, bottom row), which follows the concentration results described in the previous section.

We also assessed the changes in cardiovascular disease mortality attributable to annual $PM_{2.5}$ exposure (Fig. 6). The changes were relatively minor for all tropical regions (which correspond to the high fire activity areas in Fig. 2a). The largest changes, which were still less than 10%, were only observed in years with high fire activity, such as the 2006 fire season in Equatorial Asia. The non-linear shape of the concentration-response function that is used to estimate mortality dampens the effect of changes in high concentrations on mortality estimates.

3.3 Radiative Forcing

Global 5-year average combined shortwave and longwave radiative forcing was 10% and 6% higher at the top of atmosphere and surface, respectively, in DF versus MF when we considered only the BC (or OC) tracer from biomass burning (see Shindell et al. [2013b] for an overview of global aerosol radiative forcing). The effect was much smaller when we consider BC (or OC) as a whole, because there is no change in the other BC (or OC) components (fossil and bio fuel emissions). Figure 7 shows maps of the combined shortwave and longwave radiative forcing (DF-MF and DF only) for the surface and top of atmosphere (in 10^{-2} W/m^2) for BC from biomass burning. Relative changes in the forcing were largest in Equatorial Asia (~+75% in DF over much of the region at the top of atmosphere and over 80% north of Sumatra and Borneo at the surface); Africa and South America show mixed changes generally within +/- 30%. Changes in atmospheric heating (TOA-surface forcing) followed the observed TOA patterns (maps not shown). There was little change (~1%) in hemispheric or global ozone forcing and no change in sulfate forcing.

4. Discussion

We observed both increases and decreases of aerosol concentrations in response to changing the temporal resolution of fire emissions, though the changes generally support our three hypotheses. Compared with ground-based AERONET observations, we found that correlations between simulated and observed AOD tend to improve with DF over MF (Table 2), but found less improvement when model simulations were compared with satellite AOD. Improvements were more pronounced in South America and Equatorial Asia than savanna-dominated Southern Hemisphere Africa, which is expected from the ability of DF to capture fire events that are concentrated over several days in these biomes. Analysis into the mechanism behind these changes lends support to our hypothesis that the daily fire emissions are better timed with meteorology. For example, wet deposition of BC was much lower with daily fire emissions (Fig. 3) and the global lifetime was 10% higher (Table 3), suggesting that the fire emissions were not released as frequently during rainy days or were emitted into faster-moving air masses that could carry more emissions to higher altitudes.

The impacts of daily emissions on trace gases were generally smaller, likely due to several interactions in affected chemical processes, and to the longer lifetime of the gases examined compared to aerosols. As with aerosols, we observe both increases and decreases of CO after implementing daily resolution fires (increases in Borneo, Singapore, and western Africa; slight decreases elsewhere), which was similar to the spatial pattern of aerosols but smaller in magnitude. In contrast, O_3 and OH decreased in all tropical source regions, but with relatively small changes. Comparisons to ground-based observations were inconclusive because tropical WDCGG station coverage was much lower than for

AERONET, which made it difficult to find stations close to fires. This could be due to the stations not collecting measurements during peak fire times during 2005-09, or to the stations being located far enough away from burning regions that either fires did not influence concentrations or the signal was thoroughly mixed before reaching the station.

$PM_{2.5}$ air quality metrics were more affected by the changes in fire emissions temporal resolution than O_3, and with more changes in exceedance days >75 $\mu g/m^3$ $PM_{2.5}$ in South America and Equatorial Asia than in Africa. The increase in extreme concentrations evident in DF is likely strongly influenced by the increase in peak fire emissions (Figure 5). Monthly average fire emissions cannot resolve these extreme emissions with as much detail (see Figure 4 in Mu et al. [2011]). While this was important for modeling population exposure to $PM_{2.5}$ above WHO-designated thresholds, we did not find substantial differences in the mortality burden between the two emissions datasets or with threshold exceedances for O_3. Regardless, many countries, including the United States, determine compliance with air quality standards by calculating the number of days that exceed given thresholds for certain pollutants (http://www.epa.gov/air/criteria.html). Our results suggest that for modeling exceedances over $PM_{2.5}$ guidelines, it is important to recognize how the fire emissions input dataset itself may modify the determination of compliance for different mitigation or future change scenarios.

Resulting changes in radiative forcing estimates could alter model estimates of how fires impact the hydrological cycle and atmospheric heating or cooling, among other effects. There were large regional changes in radiative forcing for biomass burning components of BC or OC (between -30% to +50% in localized areas of Equatorial Asia). These regional

changes in atmospheric absorption can strongly influence model representations of changes in local temperature and precipitation.

This analysis showed how the temporal variability of fire emissions could cause uncertainty in modeling the atmospheric impacts of fires. Aerosols were more strongly influenced by the emissions temporal resolution, which can have important effects in understanding how well models reproduce constituent observations, estimating exceedances over air quality thresholds, and predicting regional radiative forcing effects. Further investigation will explore the robustness of these results to different atmospheric models and the sensitivity to using diurnal resolution fire emissions.

Acknowledgements

The authors would like to thank Ruth DeFries for helpful discussions regarding this work. We acknowledge support from the NSF Graduate Research Fellowship Program, NASA MAP and ACMAP programs, and the NASA High-End Computing (HEC) Program through the NASA Center for Climate Simulation (NCCS).

TABLES AND FIGURES

Table 1. Description of ground-based validation data for intercomparison with model simulations. WDCGG= World Data Centre for Greenhouse Gases, Aeronet=Aerosol Robotic Network, AOD=Aerosol Optical Depth, SHSA=Southern Hemisphere South America, SHAF=Southern Hemisphere Africa, EQAS=Equatorial Asia. Time period lists data beginning and ending dates, irrespective of gaps.

Source	Species	Region	Location	Time Period
WDCGG	CO	SHSA	Arembepe, Brazil (-12.8, -38.2)	10/2006-12/2009
	CO, O_3	SHSA	Ushuaia, Argentina (-54.8, -68.3)	3/2005-1/2009
	O_3	SHSA	San Lorenzo, Paraguay (-25.4, -57.6)	3/2005-10/2007
	CO, O_3	SHAF	Cape Point, South Africa (-34.4, 18.5)	CO: 1/2007-12/2009 O_3: 1/2005-12/2009
	CO, O_3	SHAF	Mt. Kenya, Kenya (-0.1, 37.3)	CO: 1/2005-5/2006 O_3: 3/2005-5/2006
	CO	SHAF	Gobabeb, Namibia (-23.6, 15.0)	8/2006-12/2009
	CO, O_3	EQAS	Bukit Koto Tabang, Indonesia (-0.2, 100.3)	CO: 1/2005-12/2009 O_3: 1/2005-12/2007
	O_3	EQAS	Danum Valley, Malaysia (5.0, 117.8)	1/2007-5/2008
Aeronet	AOD	SHSA	Abracos Hill (-10.8, -62.4)	1/2005-10/2005
			Alta Floresta (-9.9, -56.1)	1/2005-12/2009
			Belterra (-2.6, -55.0)	1/2005-4/2005
			Campo Grande (-20.4, -54.5)	1/2005-12/2009
			Cuiba Miranda (-15.7, -56.0)	1/2005-6/2009
			Petrolina Sonda (-9.4, -40.5)	1/2005-9/2009
			Rio Branco (-10.0, -67.9)	1/2005-12/2009
			Santa Cruz (-17.8, -63.2)	2/2005-12/2009
			Santa Cruz Utepsa (-17.9, -63.2)	9/2006-11/2008
			Sao Paulo (-23.6, -46.7)	1/2005-12/2009
	AOD	SHAF	ICIPE-Mbita (-0.4, 34.2)	3/2006-8/2008
			Ilorin (8.3, 4.3)	1/2005-12/2009
			Kibale (0.6, 30.4)	12/2006-1/2007
			Mongu (-15.3, 23.2)	1/2005-12/2009
			Nairobi (-1.3, 36.9)	12/2005-6/2009
			Niamey (13.5, 2.2)	8/2006-1/2007
			Skukuza (-25.0, 31.6)	1/2005-12/2009
	AOD	EQAS	Jabiru (-12.7, 132.9)	5/2005-12/2009
			Bandung (-6.9, 107.6)	5/2009-12/2009
			Puspiptek (-6.4, 106.7)	8/2007-11/2007
			Singapore (1.3, 103.8)	11/2006-12/2009
			Bac Lieu (9.3, 105.7)	5/2006-7/2009
			ND Marbel University (6.5, 124.8)	12/2009
			Songkhla (7.2, 100.6)	1/2007-12/2009

Table 2. Linear correlation coefficient (R^2) between 24-hour ground-based AERONET and WDCGG observations and model simulations. Italicized results are not statistically significant at the 0.05 level using a student's t-test. Summary rows indicate how many stations showed improvement for DF versus MF, only when MF and DF were both significant and with R^2>0.10. SHSA=Southern Hemisphere South America, SHAF=Southern Hemisphere Africa, EQAS=Equatorial Asia.

Species	Region	Location	DF	MF	NF
CO	SHSA	Ushuaia	0.31	0.32	0.16
		Arembepe	*0.36*	*0.37*	0.11
		Summary	**0/1 D>M**		
	SHAF	Cape Point	*0.32*	*0.33*	0.32
		Mt. Kenya	0.22	0.26	0.054
		Gobabeb	0.15	0.18	0.11
		Summary	**0/2 D>M**		
	EQAS	Bukit Koto Tabang	0.43	0.34	0.073
		Summary	**1/1 D>M**		
O_3	SHSA	San Lorenzo	0.27	0.29	0.0071
		Ushuaia	0.60	0.60	0.58
		Summary	**0/1 D>M**		
	SHAF	Cape Point	0.61	0.61	0.55
		Mt. Kenya	0.057	0.065	0.014
		Summary	**0/0 D>M**		
	EQAS	Danum Valley	0.28	0.28	*0.27*
		Bukit Koto Tabang	0.18	0.21	0.16
		Summary	**0/1 D>M**		
AOD	SHSA	Abracos Hill	0.62	0.56	0.048
		Alta Floresta	0.48	0.50	0.12
		Belterra	0.46	0.18	0.14
		Campo Grande	0.52	0.40	0.024
		Cuiba Miranda	0.72	0.45	0.024
		Petrolina Sonda	0.092	0.090	0.073
		Rio Branco	0.41	0.52	0.067
		Santa Cruz	0.59	*0.49*	0.0007
		Santa Cruz Utepsa	*0.50*	*0.56*	0.13
		Sao Paulo	0.24	0.14	*0.024*
		Summary	**5/7 D>M**		
	SHAF	ICIPE-Mbita	0.048	0.029	0.025
		Ilorin	0.19	0.18	0.087
		Kibale	0.26	0.43	0.078
		Mongu	0.45	0.39	0.053
		Nairobi	0.13	0.11	0.15
		Niamey	0.44	0.44	0.30
		Skukuza	0.23	0.20	0.079
		Summary	**4/5 D>M**		
	EQAS	Jabiru	0.32	0.32	*0.17*
		Bandung	0.0015	0.018	0.033
		Puspiptek	0.0041	0.070	0.052
		Singapore	0.083	0.044	0.0042
		Bac Lieu	0.15	0.088	0.063
		ND Marbel University	*0.64*	*0.42*	*0.44*
		Songkhla	0.12	0.13	0.088
		Summary	**0/2 D>M**		

Table 3. Global average annual lifetimes for BCB, OCB, CO, and O_3 for DF and MF model runs. CO lifetime is for the tropical troposphere only; O_3 is represented by the global tropospheric burden, in Tg.

Species	DF	MF
BCB	5.2 days	4.7 days
OCB	4.7 days	4.3 days
CO	43.4 days	43.3 days
O_3	221.9 Tg	222.2 Tg

Table 4. BCB, CO, and O_3 fluxes for the small analysis regions outlined in Fig. 2a. Positive u-flux is eastward and positive v-flux is northward.

		U-flux		V-flux	
	Region	DF	MF	DF	MF
BCB (10^{-1} kg/s)	S. America	15.3	15.1	21.6	19.7
	Africa	-21.5	-19.2	-18.0	-16.7
	Eq. Asia	-4.7	-4.5	4.3	2.9
CO (10^3 kg/s)	S. America	0.98	0.97	2.4	2.4
	Africa	-1.6	-1.6	-0.57	-0.54
	Eq. Asia	-0.79	-0.81	0.78	0.78
O_3 (10^3 kg/s)	S. America	4.1	4.1	3.7	3.7
	Africa	-0.72	-0.71	0.27	0.30
	Eq. Asia	-1.4	-1.4	0.002	0.007

Figure 1. 2005-09 average differences for surface aerosol and trace gas concentrations (DF – MF emissions global model runs), including all biomass burning sources. a) Carbonaceous aerosols (OC+BC), b) carbon monoxide (CO), c) ozone (O_3), and d) the hydroxyl radical (OH).

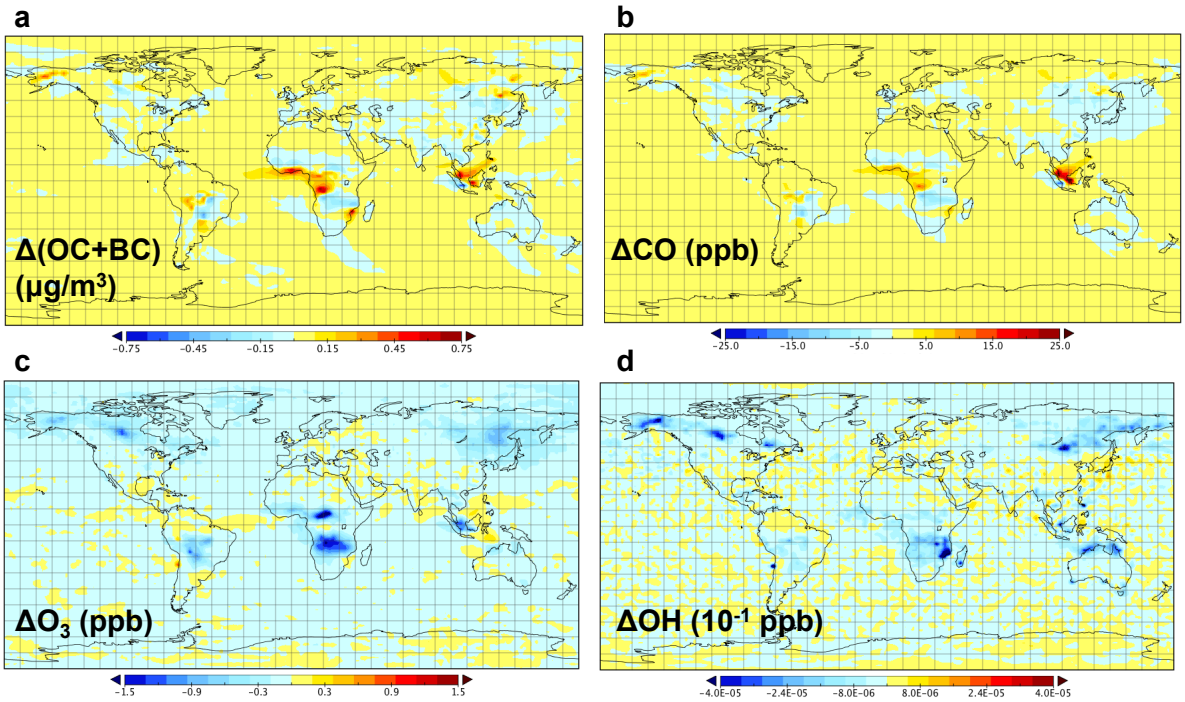

Figure 2. a) Regions of analysis for model-data intercomparisons. Locations for comparisons of model AOD with MODIS and MISR satellite AOD observations (black stars), GFED basis regions (dotted black boxes) and small target regions for analysis (red). Underlying map shows the 2005-09 average carbonaceous surface aerosol concentrations due to fires only, using daily fire emissions. b) Daily mean satellite AOD (MODIS, top row, and MISR, bottom row) versus modeled AOD for 2005-2009.

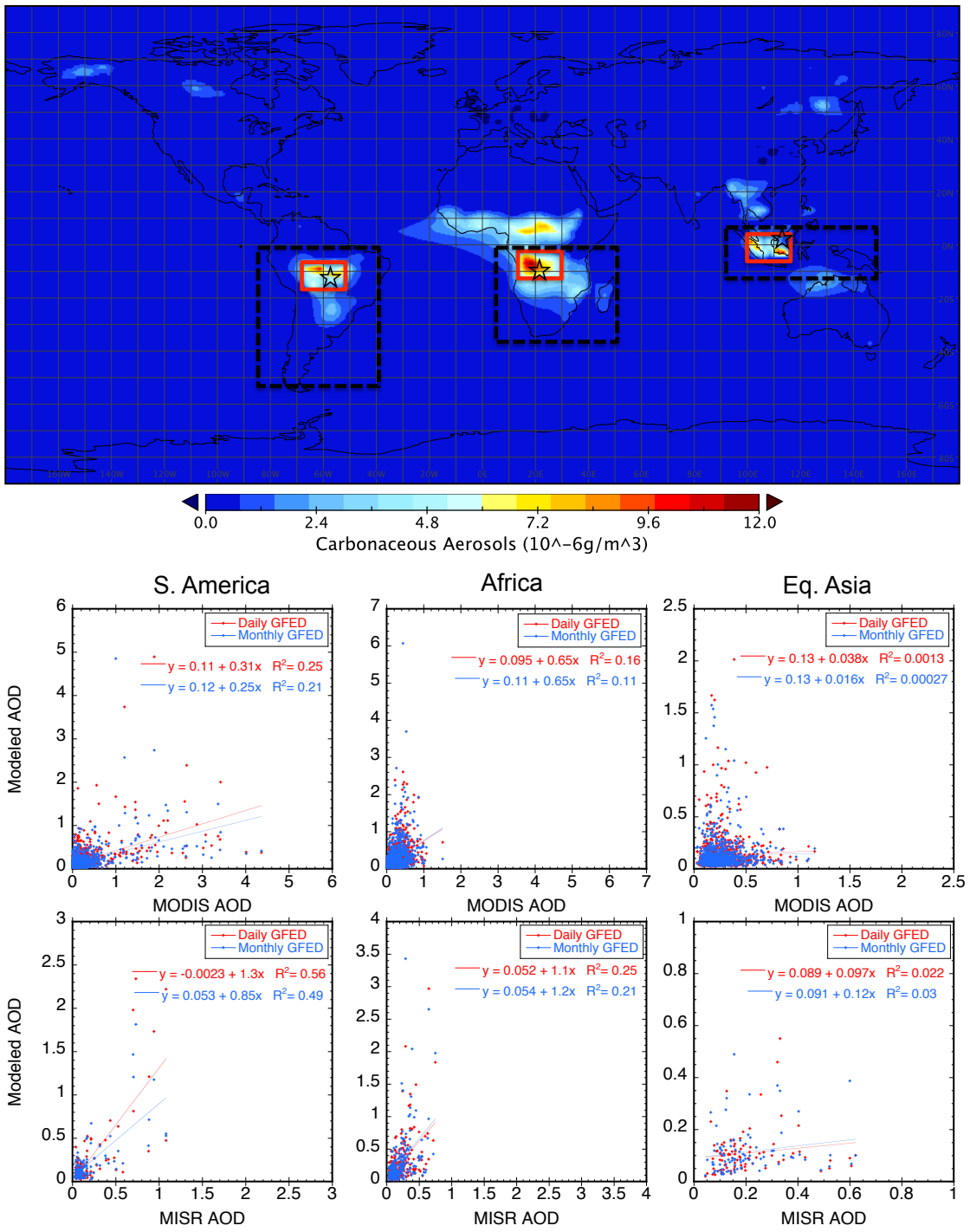

Figure 3. Difference in monthly wet deposition, normalized by concentrations, for black carbon from biomass burning. Negative values indicate that there was less wet deposition in DF for that month. Locations refer to boxes in Fig. 2a; top row represents GFED regions and bottom row represents smaller target regions.

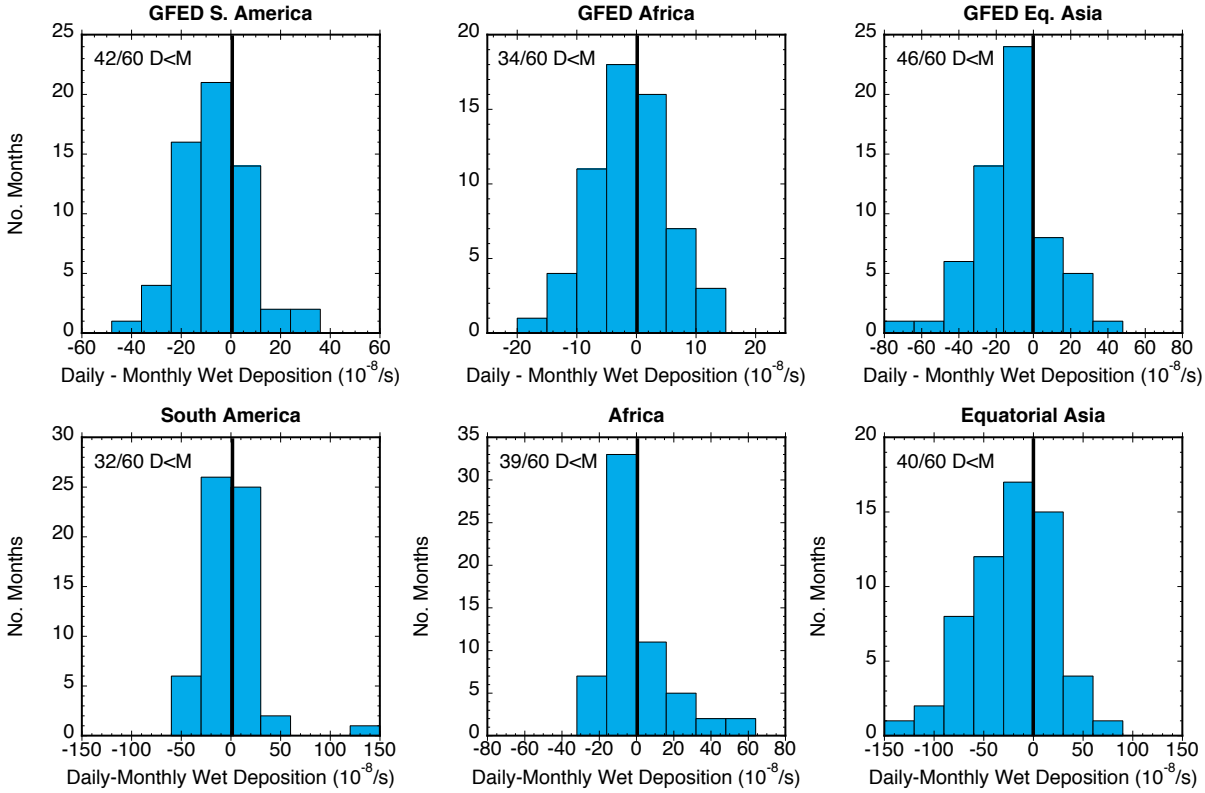

Figure 4. Accumulated daily exceedances over WHO interim targets for 2005-09, for small target regions shown in Fig. 2a. Top row are exceedances over the 75 μg/m^3 24-hour $PM_{2.5}$ target; bottom row are exceedances over the 240 μg/m^3 8-hour maximum O_3 target.

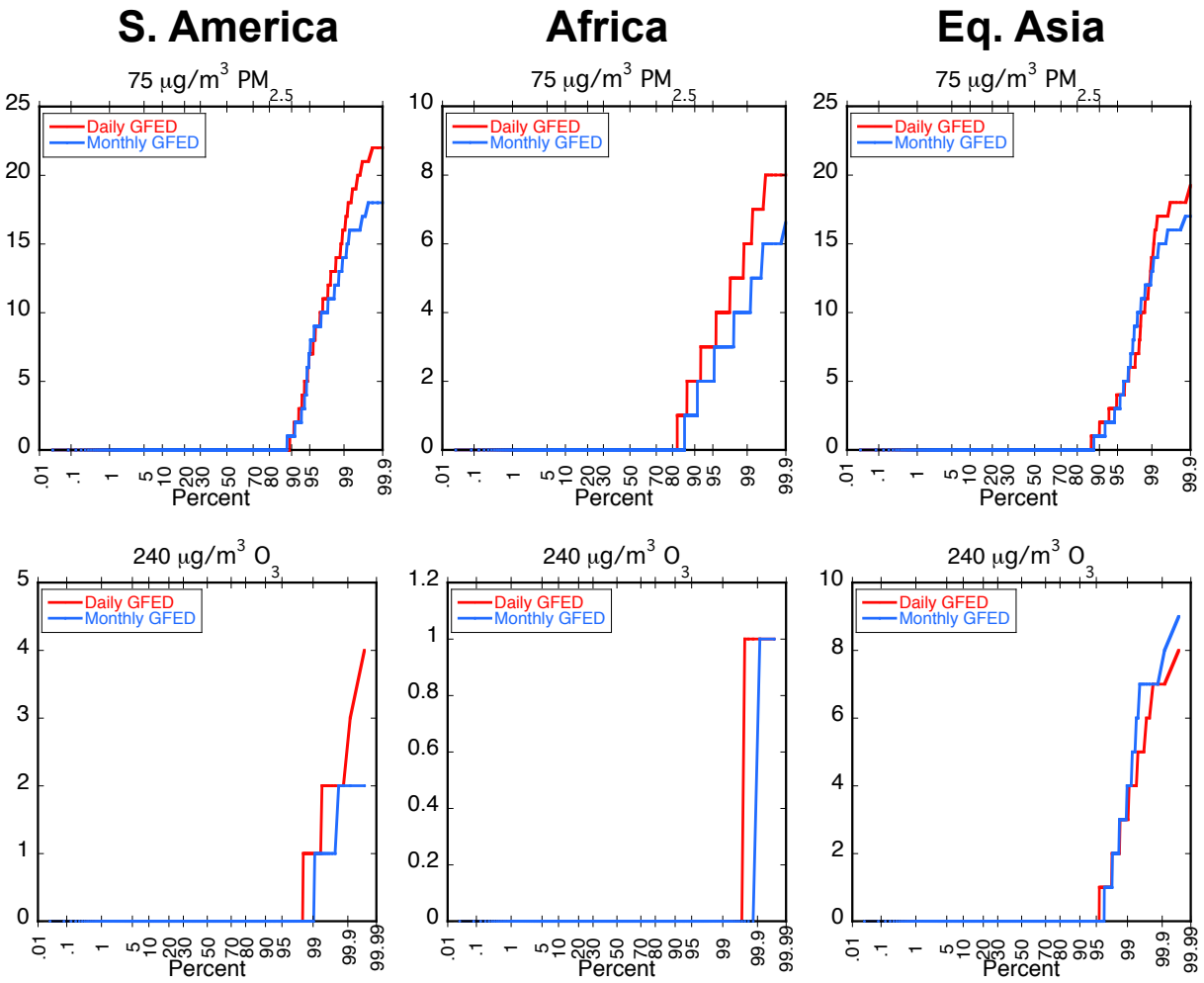

Figure 5. Difference between 24 hour DF and MF (y-axis) versus DF $PM_{2.5}$ concentrations (x-axis). Note log scale on x-axis.

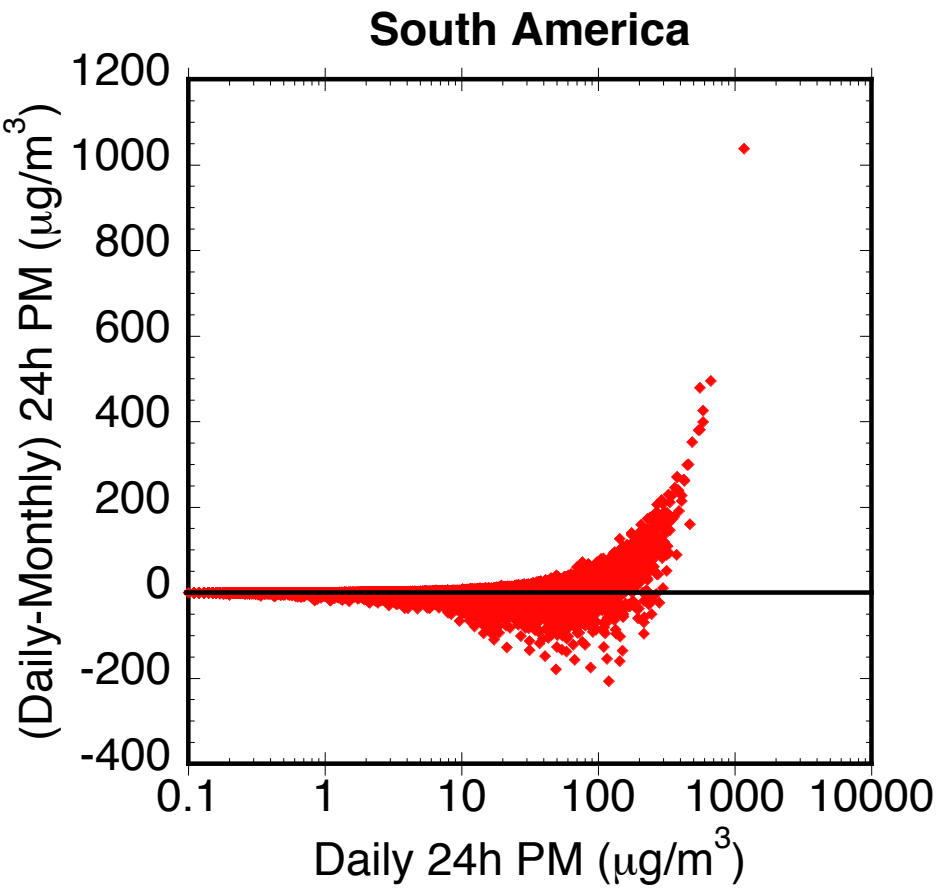

Figure 6. Annual 2005-09 cardiovascular disease (CVD) mortality due to annual $PM_{2.5}$ exposure to fires-only pollution for DF and MF. Locations correspond to small target regions in Fig. 2a.

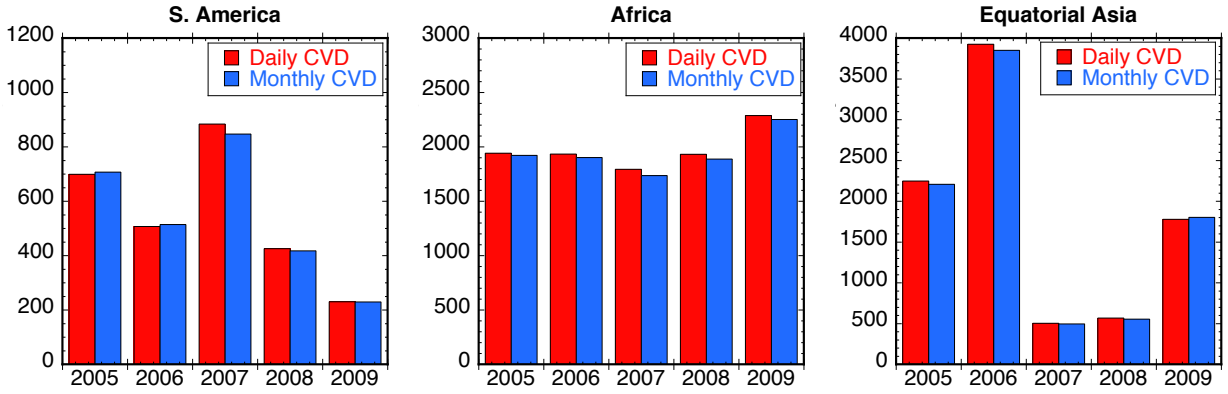

Figure 7. Radiative forcing (combined shortwave and longwave) for black carbon from biomass burning only at the surface and top of atmosphere (TOA). Units are in 10^{-2} W/m^2.

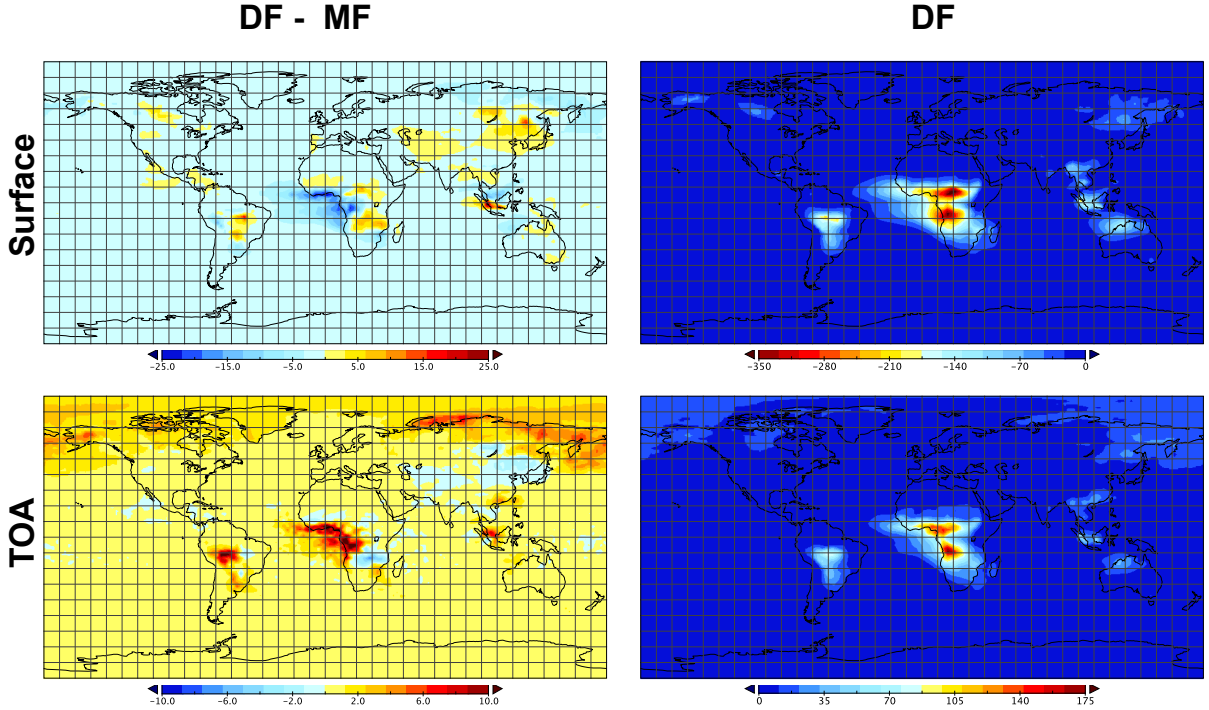

Supplementary Figure S1. 2005-09 average relative differences for aerosol and trace gas concentrations ((DF – MF)/MF emissions global model runs), including all biomass burning sources. a) Carbonaceous aerosols (OC+BC), b) carbon monoxide (CO), c) ozone (O_3), and d) the hydroxyl radical (OH). Note changes in scale.

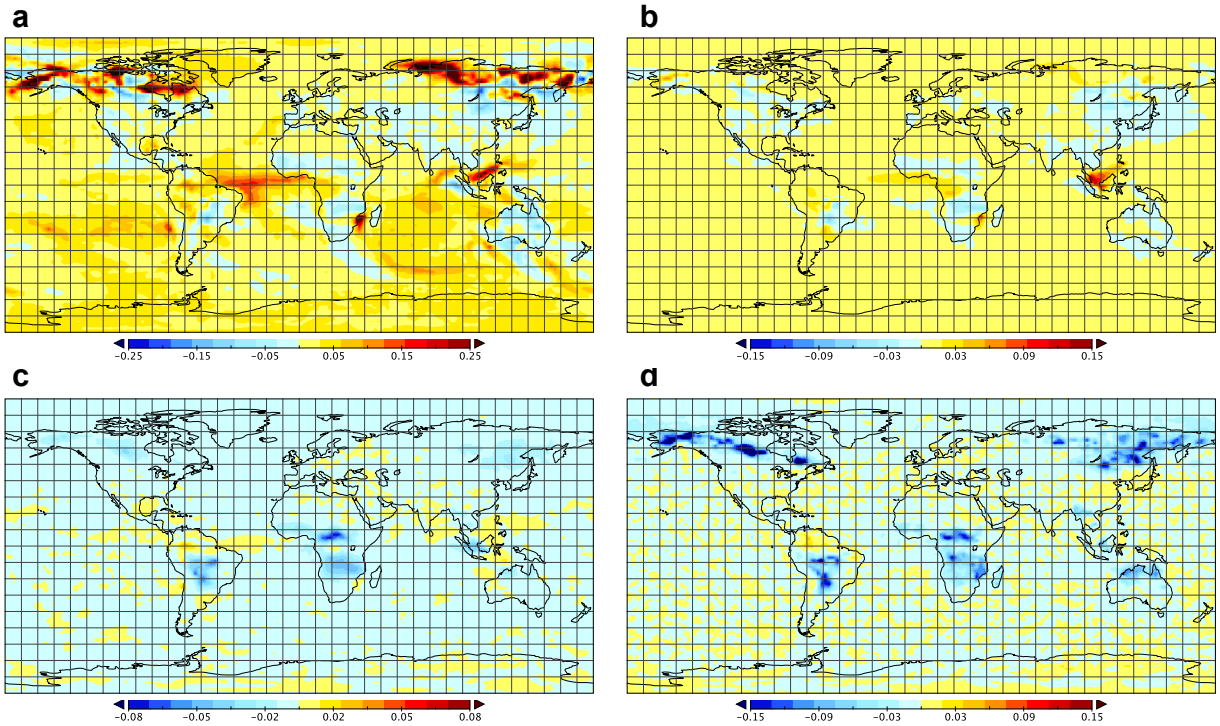

CHAPTER THREE

El Niño and health risks from landscape fire emissions in Southeast Asia

Miriam E. Marlier, Ruth S. DeFries, Apostolos Voulgarakis, Patrick L. Kinney, James T. Randerson, Drew T. Shindell, Yang Chen, and Greg Faluvegi

Published in *Nature Climate Change (2013), 3, 131-136.*

Abstract

Emissions from landscape fires affect both climate and air quality [*Langmann et al.*, 2009]. In this study, we combine satellite-derived fire estimates and atmospheric modeling to quantify health effects from fire emissions in Southeast Asia from 1997 to 2006. This region has large interannual variability in fire activity due to coupling between El Niño-induced droughts and anthropogenic land use change [*Jones*, 2006; *Field and Shen*, 2008]. We show that during strong El Niño years, fires contribute up to 200 $\mu g/m^3$ and 50 ppb in annual average fine particulate matter ($PM_{2.5}$) and ozone (O_3) surface concentrations near fire sources, respectively. This corresponds to a fire contribution of 200 additional days per year that exceed the World Health Organization (WHO) 50 $\mu g/m^3$ 24-hour $PM_{2.5}$ interim target (IT-2) [*World Health Organization*, 2006] and an estimated 10,800 (6,800-14,300) person (~2%) annual increase in regional adult cardiovascular mortality. Our results indicate that reducing regional deforestation and degradation fires would improve public health along with widely established benefits from reducing carbon emissions, preserving biodiversity, and maintaining ecosystem services.

Introduction

Fires are pervasive instruments of land management in the tropics for clearing debris in the process of deforestation and agricultural management. These fires enable an economical and effective method for expanding and maintaining agricultural production, but release gases (including O_3 precursors) and aerosols (mostly black and organic carbon) that interact with the climate system [*Tosca et al.*, 2010], degrade surface air quality [*Langmann et al.*, 2009], and jeopardize public health [*Heil and Goldammer*, 2001]. Fires

associated with deforestation emitted ~1.0 Pg C/yr from 2000-10 [*Baccini et al.*, 2012], with considerable interannual variability from droughts in tropical forests [*van der Werf et al.*, 2010]. Fires also contribute to $PM_{2.5}$ and O_3 increases, which are both detrimental to public health [*World Health Organization*, 2006; *Langmann et al.*, 2009]. Projections of greater fire activity in a warming climate [*Pechony and Shindell*, 2010] suggest increasing contributions to atmospheric concentrations and population exposure.

Globally, most fires occur in Africa and South America [*van der Werf et al.*, 2010], but recent studies have highlighted the importance of Southeast Asia because of high population densities near high fire activity [*Johnston et al.*, 2012]. Regional emissions may differ by a factor of 50 between opposite phases of the El Niño-Southern Oscillation (ENSO). In the Global Fire Emissions Database version 3 (GFED3), regional fire emissions were 1069 Tg C during the 1997 El Niño but only 21 Tg C during the 2000 La Niña [*van der Werf et al.*, 2010], illustrating the nonlinearity between fires and drought [*van der Werf et al.*, 2008]. During the warm phase of ENSO and the Indian Ocean Dipole, cool sea surface temperature anomalies near Indonesia decrease regional rainfall [*Field and Shen*, 2008; *Wooster et al.*, 2012]. Landowners ignite fires to clear land and manage agricultural areas [*Jones*, 2006], and although typically too wet to combust, deforestation and degradation have enhanced the susceptibility of peatland forests (with carbon-rich peat deposits) to human-ignited fire during droughts [*Siegert et al.*, 2001].

$PM_{2.5}$ and O_3 exposure increases hospital admissions and mortality from respiratory and cardiovascular diseases, even at low concentrations [*World Health Organization*, 2006]. During the 1997-98 fires in Southeast Asia, daily ground-level PM concentrations reached hazardous levels [*Heil and Goldammer*, 2001], with concomitant negative impacts on

respiratory and general health [*Frankenberg et al.*, 2005]. Increases in respiratory illnesses were also reported in Singapore from transported emissions [*Emmanuel*, 2000]. While these studies offer some information on the health effects of fires, they have been confined to specific locations or time periods by limited data availability.

We expand on these local studies by using satellite data and two atmospheric models, NASA GISS-E2-PUCCINI general circulation model (GCM) and Harvard University's GEOS-Chem chemical transport model (CTM) to estimate pollutant concentrations and corresponding regional mortality from 1997 to 2006, applying existing concentration-response functions from the epidemiological literature (See Methods). Atmospheric models simulate the transport of fire emissions and formation of pollutants, offer a continuous spatiotemporal dataset in a region with limited ground monitoring but large rural populations, and allow us to examine how climate and emissions influence aerosol and trace gas concentrations interannually.

Our study region is a 50°x30° area (92.5°E-142.5°E, 20°N-10°S) encompassing the Association of Southeast Asian Nations (ASEAN). In 2005, the population was approximately 540 million (Fig. 1a). Fire activity, predominately in the Indonesia islands of Sumatra and Borneo (Fig. 1b), peaks during the dry southern monsoon of September and October, along with potential spring burning [*Heil and Goldammer*, 2001; *Field and Shen*, 2008].

Results

The additional contribution of fires to annual surface $PM_{2.5}$ and O_3 concentrations in 1997, a strong El Niño year, greatly increases the number of days that exceeded the WHO

interim targets of 50 μg/m^3 24-hour $PM_{2.5}$ (IT-2) and 80 ppb 8-hour maximum O_3 (IT-1), which are both twice the WHO's air quality guidelines (Fig. 2; Supplementary Table S1). In 1997, both models show two distinct areas of fire-derived $PM_{2.5}$ over Sumatra and Borneo with concentrations elevated by 50-200 μg/m^3 and with increases of 50-150 days over the WHO interim targets. O_3, in contrast, had widely distributed increases of 25-50 ppb and up to 150 exceedance days. Corresponding results with all sources in 1997 are in Supplementary Fig. S1, this simulation captured the general temporal evolution seen in ground observations (Supplementary Figs. S2, S3, S4; Supplementary Table S2).

We explored how modeled concentrations with and without fire emissions affect population exposure to WHO interim targets (Supplementary Table S1) [*World Health Organization*, 2006]. Decadal exposure over these interim targets, along with the fraction of exposure due to fire, shows how the major influence of fires was not confined to the 1997-98 El Niño (Fig. 3). Interannual variability in exposure for both short- and long-term guidelines is dominated by the fire contribution of $PM_{2.5}$ and O_3; the WHO's 25 μg/m^3 annual $PM_{2.5}$ interim target (IT-2) is never exceeded without including fire emissions.

We also tested the sensitivity of regional health impacts, including exceedances and cardiovascular disease mortality, to using the original model or satellite-scaled model $PM_{2.5}$ estimates (Supplementary Figure S5). The mortality estimates combine modeled pollutant concentration changes from fires with published epidemiological relationships between exposure to O_3 or $PM_{2.5}$ total mass and cause-specific mortality (See Methods). In Table 1, 1997 and 2000 highlight the considerable differences in health effects between years with high and low fire contributions. For example, $PM_{2.5}$ annual exposure in 2000 hardly exceeds the WHO interim target and O_3 exposure is 100 times lower than in 1997. During

high fire years, fire emissions increase the adult cardiovascular disease mortality burden by approximately 10,800 (6,800-14,300) annual deaths from $PM_{2.5}$ exposure and an additional 4,100 (2,300-5,900) annual deaths from O_3.

Modeled annual adult cardiovascular disease mortality shows a strong correlation with the multivariate El Niño Index (MEI) [*Wolter*, n.d.], which was averaged over the July to October dry season (Fig. 4). We present the most conservative mortality estimates, but this relationship holds with varying relative risk (RR) relationships or durations of exposure (Supplementary Fig. S6). Reduced convection during El Niño years likely increases exposure by elevating emissions [*Tosca et al.*, 2010] and increasing aerosol lifetimes by reducing wet deposition.

Uncertainty in our health effect estimates comes primarily from: 1) the fire emissions dataset, 2) atmospheric modeling, and 3) concentration-response equations. First, van der Werf et al. [2010] estimated fire carbon emissions uncertainty at 20% globally, though higher in equatorial Asia due to peat carbon stock uncertainties and in years before MODIS data. Second, although the lack of ground stations precludes an in-depth evaluation, available ground data and satellite AOD indicate that both models are likely conservative (Supplementary Figs. S3, S4, S5). The range between the two model scenarios ($PM_{2.5}$ and O_3) and two satellite AOD optimized results ($PM_{2.5}$ only) provide some insight about uncertainty related to transport and deposition processes. There is up to a factor of two difference between models (less among satellite-optimized estimates), but this range is expected given previous findings that model physics and parameterizations drive more variation in aerosols than emissions [*Textor et al.*, 2007]. Differences in our $PM_{2.5}$ concentrations are primarily driven by lower precipitation and wet deposition in the

GISS model, which increase aerosol lifetime relative to GEOS-Chem (data not shown). However, for the purposes of health impacts the results are much closer (Table 1). This is due to the nonlinear relationship between the RR and exposure, which reduces differences between mortality estimates at high concentrations. Finally, we address mortality equation uncertainties through 95% confidence intervals around the concentration-response estimates (Table 1) and various estimates of the RR and $PM_{2.5}$ exposure relationship (Supplementary Tables S3 and S4; Supplementary Fig. S6). Additional epidemiological factors that we did not address are extrapolation of RR equations to high concentrations and applying equations developed in the U.S. to non-U.S. populations. In addition, evidence for potential differences in $PM_{2.5}$ toxicity between urban pollution in U.S. cities and Southeast Asian fire emissions is too limited to warrant using separate epidemiological equations [*Naeher et al.*, 2007], so we assume that total $PM_{2.5}$ mass is the most appropriate metric.

These uncertainties and additional factors contribute to our substantially lower regional $PM_{2.5}$ mortality estimates relative to the global analysis of Johnston et al. [2012]. The two estimates are not directly comparable. Our conservative estimates (Supplementary Table S5) are based on a tailored regional analysis for ASEAN countries and use updated fire emissions, multiple atmospheric models, epidemiological equations developed over a wide concentration range, and cause-specific disease estimates (Supplementary Table S6). We did not include children since the epidemiological equations were developed for adults over 30 years; this cuts out more than half of the population and ignores risks to infants and children.

Discussion

While previous work in Borneo has emphasized the value of avoided deforestation in terms of carbon emissions [*Naidoo et al.*, 2009], it is important to also account for health. By demonstrating the direct link between climate variability and health impacts from fire emissions throughout Southeast Asia, we offer additional support for policies that use regional climate forecasts to restrict burning during high fire risk seasons. Fire emissions during 1997 to 2006 repeatedly exposed 1-11% of the population in Southeast Asia to $PM_{2.5}$ and O_3 above WHO interim targets during El Niño years. Although the regional influence of climate change is uncertain [*Collins et al.*, 2010], these observed trends would be exacerbated by the potential for more frequent droughts related to El Niño and increased baseline cardiovascular disease caused by demographic shifts towards sedentary lifestyles and increased animal product consumption. Reducing fires from deforestation and land management would benefit public health in addition to global-scale benefits for carbon storage and biodiversity.

Methods

Fire emissions estimates are from GFED3, a global gridded monthly emissions dataset that combines surface reflectance and active fire detection data from several satellites to detect the spatiotemporal variability of burned area [*Giglio et al.*, 2010]. This drives a biogeochemical model that estimates fuel loads, combustion completeness, and emissions [*van der Werf et al.*, 2010]. GFED3 is available since 1997 at 0.5°x0.5°. We define landscape fires to include all burning sources; in Southeast Asia this includes peat, forest, agricultural waste burning, deforestation and degradation.

We use two models: the NASA GISS-E2-PUCCINI GCM from 1997-2007 and Harvard University's GEOS-Chem CTM [*Bey et al.*, 2001] from 1997-2006. See Supplementary Information for descriptions of the models, spin-up, and boundary conditions. Both were run at 2°x2.5°, including a control run without fire emissions and a perturbed run with GFED3 emissions. We define years from July 1st to June 30th to avoid splitting a burning season into two years. Since meteorological fields for GEOS-Chem are available through December 2006, we only have a complete 2006 "fire-year" from GISS. For $PM_{2.5}$, we analyzed 24-hour and annual average concentrations. For O_3, we used 1-2pm concentrations as a proxy for the 8-hour maximum (Supplementary Fig. S4) and 24-hour concentrations for mortality calculations.

Aerosol optical depth (AOD) data from MISR and MODIS satellite instruments, available from 2001-2006, were used to scale modeled AOD; these scaling factors were then applied to modeled $PM_{2.5}$ (Supplementary Fig. S5). While AOD represents total column aerosol loading, it is often closely related with surface abundance [*Van Donkelaar et al.*, 2010], and hence provides some measure of large-scale biases in the models. Scaling factors were applied to surface $PM_{2.5}$ for all grid boxes, maintaining the modeled spatial and temporal distribution of aerosols.

We evaluate health effects by estimating: 1) exposure above WHO short-term and annual air quality targets, and 2) cause-specific adult mortality. Mortality attributable to fires combines the relative risk (RR) from changes in pollutant exposure with baseline observed mortality rates. We focus on cardiovascular disease because it is a proximal outcome from exposure that will be experienced annually. However, this underestimates

total mortality due to other long-term effects and short-term exposure. The equations that we use were developed for adults (less than half of the regional population [*UN*, 2011]).

We applied a power-law relationship between RR and $PM_{2.5}$. Due to the lack of data on differential health effects of biomass smoke particles [*Naeher et al.*, 2007], we use an equation developed for total $PM_{2.5}$ mass:

(1) Cardiovascular $RR=1+\alpha(I*C)^{\beta}$

which describes the relationship between $PM_{2.5}$ exposure and cardiovascular disease mortality risk over a large concentration range [*Pope et al.*, 2011]. Pope et al. [2011] published values for α and β by reanalyzing previous estimates of RR and dose of $PM_{2.5}$ (in mg) from ambient air pollution, second-hand smoke, and cigarette smoke. For cardiovascular disease, α=0.2685 and β=0.2730. Although ambient $PM_{2.5}$ concentrations from fires will not reach the cigarette smoke doses included in Pope et al. [2011], this equation was essential due to our high ambient concentrations above the range of other studies. Since 95% confidence intervals were given for each individual study but not the overall relationship, we refit a power-law relationship to approximate the uncertainty based on the individual studies' upper or lower limits, respectively. The annual average of 24-hour total mass $PM_{2.5}$ concentrations were used for (C), assuming a constant average inhalation rate (I) of 18 m^3/day to convert to $PM_{2.5}$ dose (in mg) [*Pope et al.*, 2011]. We separately calculated the RR using concentrations with and without fires due to the equation's nonlinearity. We then followed the approach of Ostro et al. [2004] to calculate the attributable fraction (AF) and annual mortality (ΔM):

(2) $AF= (RR-1)/RR$

(3) $\Delta M_{annual}= M_b*P*(AF_{fire} - AF_{nofire})$

where the average annual baseline mortality rate (M_b) was calculated from adult deaths due to cardiovascular disease, averaged over the countries in ASEAN [*World Health Organization, Department of Measurement and Health Information*, 2011]. Population with ages greater than 30 years was from the UN Population Division [*UN*, 2011] and CIESIN's Gridded Population of the World version 3 and Future Estimates, aggregated to the model resolution [*CIESIN*, 2005a; 2005b]; both were interpolated from 5 yearly data to annual estimates.

For O_3, the linear RR is given by:

(4) Cardiovascular RR= $\exp[\delta(C_{fire} - C_{nofire})]$

where δ=1.11 (0.68-1.53) is the percent increase in cardiovascular disease morality per 10 ppb increase in 24-hour O_3 concentrations, based on a meta-analysis of U.S. and non-U.S. studies [*Bell et al.*, 2005]. Daily mortality due to fire pollution is then estimated with:

(5) $\Delta M_{daily} = (M_b/365)*P*(AF_{fire} - AF_{nofire})$

using the population characteristics described above. We assume that mortality is evenly spread throughout the year (M_b is not year-specific so we divide consistently by 365), and sum by days per year to obtain annual estimates. GEOS-Chem includes leap years, but GISS uses a fixed 365 day calendar. Bell et al. [2005] concluded that the O_3 mortality burden was insensitive to PM, indicating that this is separate from $PM_{2.5}$ mortality.

Acknowledgments

We are grateful to Prasad Kasibhatla for his help with the GEOS-Chem model runs. We also thank the local staffs at Bukit Koto Tabang and Tanah Rata for the WDCGG O_3 data, Michael Brauer for the annual $PM_{2.5}$ data, and Klaus Wolter at NOAA for the El Niño index. This

work was supported by a National Sciences Foundation graduate research fellowship and NASA award NNX11AF96G. GFED3 is publicly available at http://www.globalfiredata.org.

Author Contributions

R.S.D., A.V., and M.E.M. designed the study. G.F., A.V., and M.E.M. conducted the model runs, R.S.D., A.V., J.T.R., D.T.S., Y.C., and M.E.M. contributed to the model analysis, P.L.K. and M.E.M. conducted the health estimates. All authors contributed to the writing of the manuscript.

TABLES AND FIGURES

Table 1. Fires-only concentration, exposure, and mortality using different models for an El Niño (1997) and La Niña (2000). Average ASEAN annual concentration due to fires only (from 24-hour $PM_{2.5}$ and 8-hour maximum O_3); additional exposure due to fires above the annual 25 μg/m^3 $PM_{2.5}$ interim target (IT-2; x10^6 person-years) and above the 80 ppb daily 8-hour maximum O_3 interim target (IT-1; x10^7 person-days); cardiovascular mortality due to fires only (x10^3 people), with the range from 95% confidence intervals from epidemiological studies. GISS refers to GISS-E2-PUCCINI and G-C refers to GEOS-Chem, also with satellite scaling factors.

a) $PM_{2.5}$

	Concentration (μg/m^3)		**Exposure above IT-2 (x10^6 person-years)**		**Mortality (x10^3 people)**	
	1997	*2000*	*1997*	*2000*	*1997*	*2000*
GISS	7.8	0.3	55.6	0.0	9.9 (8.0-11.4)	1.0 (0.8-1.2)
G-C	3.7	0.2	25.8	0.0	8.7 (6.8-10.7)	1.5 (1.1-1.9)
GISS MISR	10.7	0.4	57.0	0.0	11.2 (9.6-13.5)	1.3 (1.0-1.6)
G-C MISR	7.4	0.5	59.1	4.7	10.1 (8.1-11.8)	1.7 (1.4-2.1)
GISS MODIS	12.0	0.4	66.6	0.0	12.5 (10.1-14.2)	1.5 (1.1-1.8)
G-C MODIS	8.3	0.5	50.3	0.0	12.1 (9.7-14.3)	2.3 (1.8-2.8)
AVERAGE	**8.3**	**0.4**	**52.4**	**0.8**	**10.8 (6.8-14.3)***	**1.6 (0.8-2.8)***

*Maximum error range.

b) O_3

	Concentration (ppb)		**Exposure above IT-1 (x10^6 person-days)**		**Mortality (x10^3 people)**	
	1997	*2000*	*1997*	*2000*	*1997*	*2000*
GISS	9.0	1.4	395	3.5	4.3 (2.6-5.9)	1.0 (0.6-1.4)
G-C	7.1	1.3	346	0.0	3.8 (2.3-5.2)	1.0 (0.6-1.4)
AVERAGE	**8.0**	**1.4**	**371**	**1.8**	**4.1 (2.3-5.9)***	**1.0 (0.6-1.4)***

Figure 1. Study area population and locations of fire activity. a, 2005 population density, in persons per km^2, for countries belonging to the Association of Southeast Asian Nations (ASEAN). Data from CIESIN GPWv3 [*CIESIN*, 2005b] at 0.25° resolution. **b**, 1997-2006 mean fire emissions, in g C/m^2/month at 0.5° resolution, from the Global Fire Emissions Database version 3 [*van der Werf et al.*, 2010].

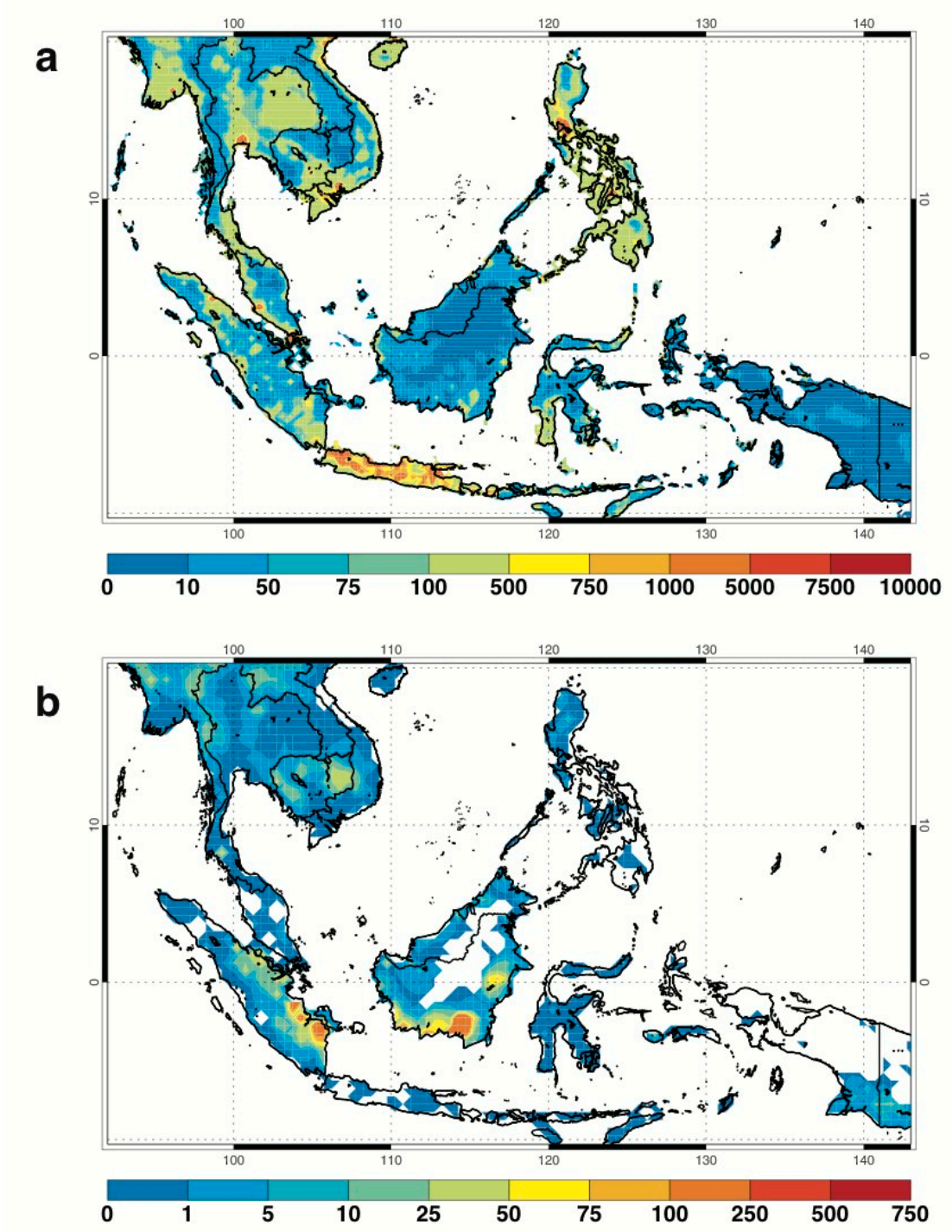

Figure 2. Modeled annual mean 1997 surface concentrations and corresponding additional daily exceedances in 1997 due to fires only. **a**, $PM_{2.5}$ **b**, O_3 annual concentrations and daily exceedances over World Health Organization (WHO) interim targets (50 μg/m^3 daily $PM_{2.5}$ (IT-2) and 80 ppb 8-hour maximum O_3 (IT-1)). Annual concentrations are from 24-hour $PM_{2.5}$ and 8-hour maximum O_3. GISS refers to GISS-E2-PUCCINI and G-C refers to GEOS-Chem.

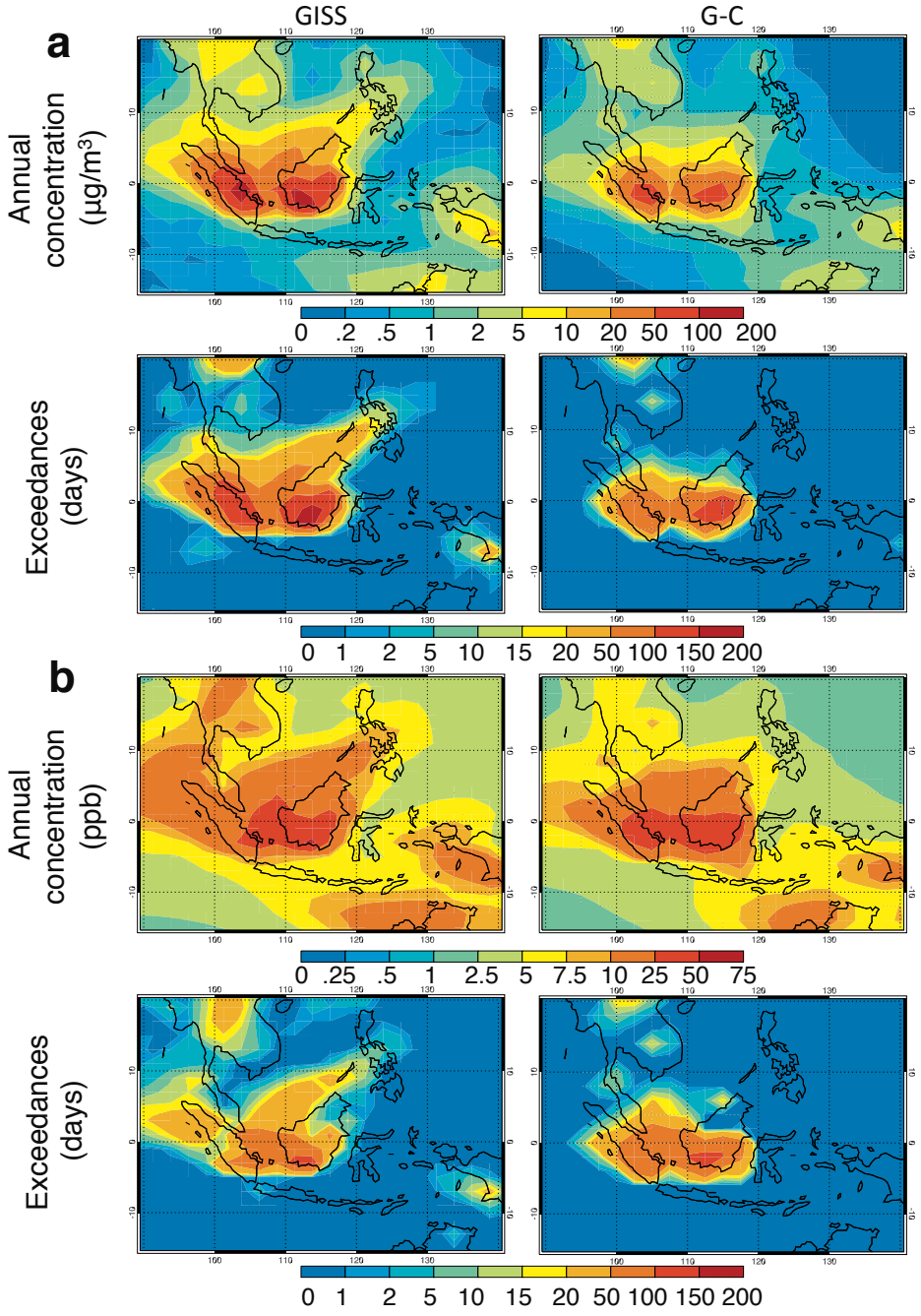

Figure 3. Population exposure above World Health Organization (WHO) interim targets. a, Exposure over 50 μg/m^3 24-hour $PM_{2.5}$ interim target (IT-2). **b**, Exposure over 25 μg/m^3 annual $PM_{2.5}$ interim target (IT-2). **c**, Exposure over 80 ppb 8-hour maximum O_3 interim target (IT-1). **d**, Fraction of population exposure above each WHO interim target that is attributable to fires. Each case is calculated with and without GFED3 fire emissions using GISS-E2-PUCCINI results, which was close to the average concentration estimate. Refer to Supplementary Table S1 for estimated health effects. Note the logarithmic scale for (**a**) and (**c**).

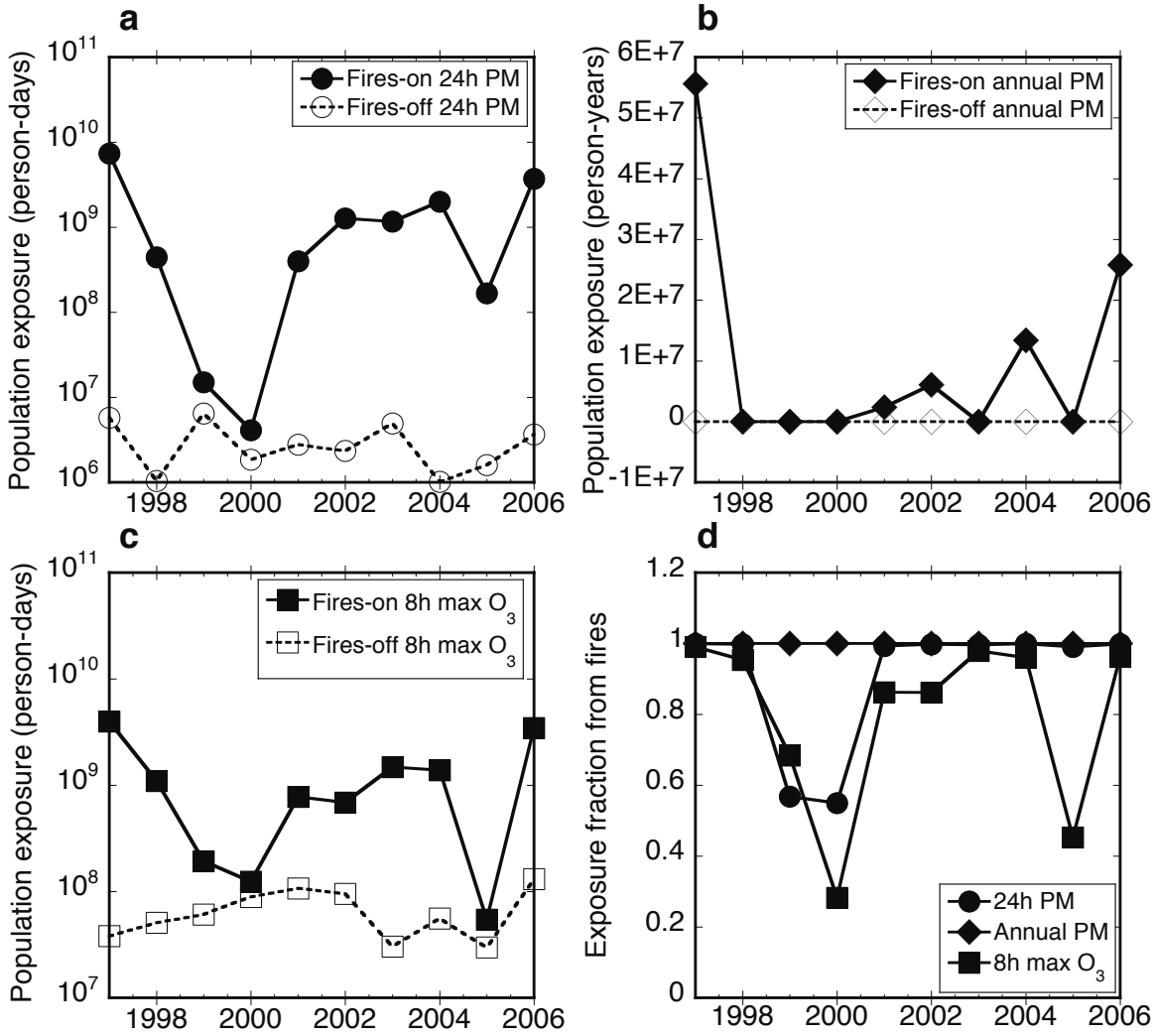

Figure 4. Additional annual cardiovascular disease (CVD) mortality from exposure to fire-contributed annual $PM_{2.5}$ and 24-hour O_3, along with the Multivariate El Niño Index (MEI) [*Wolter*, n.d.]**.** Results for 1997-2006 are from the baseline GISS-E2-PUCCINI and GEOS-Chem concentrations, with the power-law RR relationship for CVD mortality. R^2=0.87-0.91 for $PM_{2.5}$ and R^2=0.82-0.89 for O_3. AOD-scaled results and sensitivity analysis are in Table 1, Supplementary Table S4, and Supplementary Fig. S6.

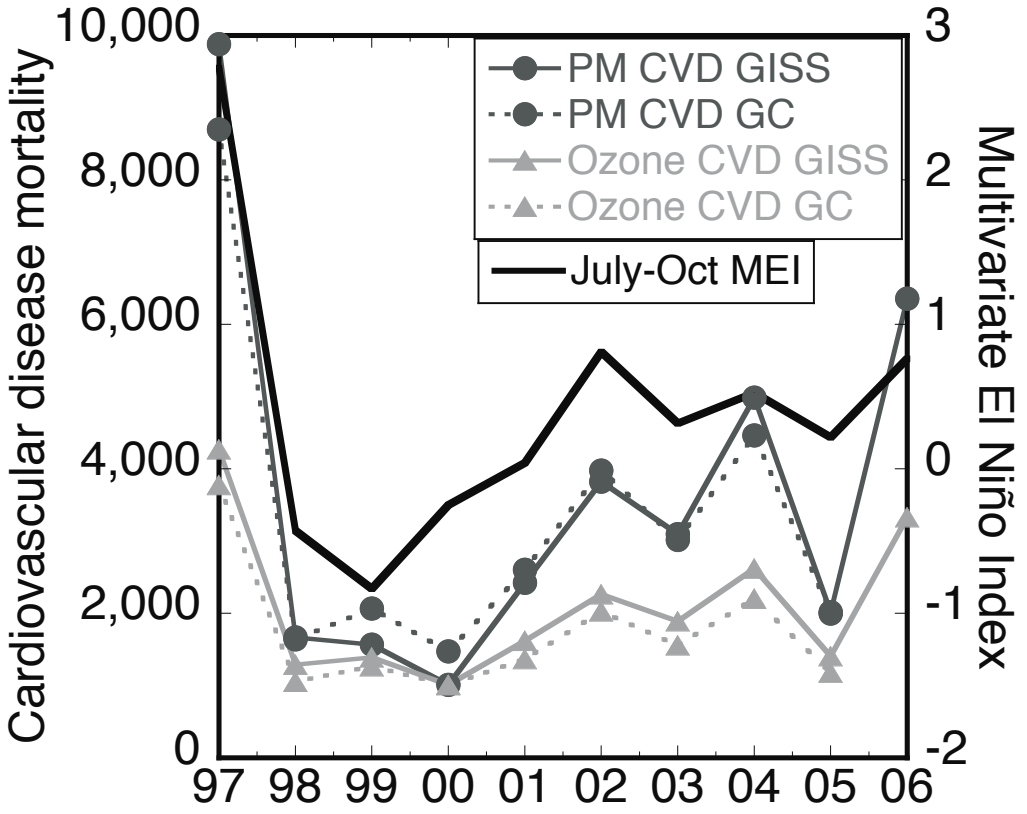

SUPPORTING INFORMATION

Model Set-up

GISS-E2-Puccini is the new version of the NASA GISS ModelE general circulation model (http://www.giss.nasa.gov/tools/modelE/). It was run at 2°x2.5° resolution with 40 vertical layers from 1997-2007; we focused on model output that approximately corresponds with the Earth's surface. With our two year spin-up period, we expect any influence of initial conditions on the nonlinear formation of O_3 to be small.

Our simulations included interactive constituents in the PUCCINI model for chemistry, aerosols (sulfate, carbonaceous, nitrate, dust and sea salt), and an aerosol indirect effect parameterization [*Koch et al.*, 2006; *Shindell et al.*, 2006]. We ran the model without fires and with GFED3 emissions mixed uniformly through the boundary layer. This assumption for the height of smoke injection is justified by previous work by Tosca et al. [2011] with satellite observations of smoke plume heights in Indonesia; 96% of all fire plumes on Sumatra and Borneo were within 500 m of the top of the planetary boundary layer during the morning (10:30 am) MISR overpass [*Tosca et al.*, 2011]. Annually and monthly-varying GFED3 emissions were used for the species available, otherwise we scaled from time-varying CO emissions. Fires do not directly emit the pollutants that we focus on for health effects: $PM_{2.5}$ and O_3. For $PM_{2.5}$, GFED3 emissions contribute black and organic carbon, which can combine with other sources of aerosols (such as sea salt, dust, and sulfate) in our modeled concentrations. GFED3 also contributes O_3 precursors, such as NO_x, CO, and VOC's, which secondarily produce O_3 in photochemical reactions. Present-day anthropogenic emissions were re-gridded to 2°x2.5° resolution based on Lamarque et al.

[2010], which was produced to provide input to models being run in support of the IPCC Fifth Assessment Report (AR5). Methane in the lowest model layer was kept to observed values for each year and lightning NO_x was generated internally based on an updated version of Price et al. [1997]. Isoprene emissions were based on Guenther et al. [1995; 2006]; vegetation alkene and paraffin emissions from the GEIA dataset are based on Guenther et al. [1995]. Model winds were linearly relaxed towards reanalysis based on meteorological observations [*Rienecker et al.*, 2011].

GEOS-Chem (http://acmg.seas.harvard.edu/geos/index.html) is an off-line atmospheric chemical transport model driven by GEOS-4 meteorological fields from NASA GMAO. We use version v9-01-01 at 2°x2.5° resolution and 30 vertical layers from 1997-2006, with a two year spin-up. Surface values correspond to the middle of the lowest model layer (about 0.06 km, on average). The GEOS-Chem model includes a comprehensive treatment of tropospheric NO_x-hydrocarbon-O_x chemistry, and a simplified treatment of aerosols including black and organic carbon, dust, sea salt, and sulfate-nitrate-ammonium aerosols. Annually and monthly varying fire emissions were scaled from GFED3 carbon emissions and were emitted into the surface layer and mixed throughout. Anthropogenic gas-phase emissions from fossil-fuel use are based on a hybrid of the global GEIA [*Piccot et al.*, 1992; *Benkovitz et al.*, 1996; *Wang et al.*, 1998] and EDGAR datasets [*Olivier and Berdowski*, 2001], overwritten by regional datasets for the United States, Canada, Mexico, Europe, and Southeast Asia. Emissions from biofuel combustion are from Yevich and Logan [2003], with regional updates over North America and Southeast Asia. Biogenic emissions from terrestrial vegetation are from the Model of Emissions of Gases and Aerosols from Nature (MEGAN) [*Guenther et al.*, 2006; *Guenther and Wiedinmyer*, 2007;

Sakulyanontvittaya et al., 2008]. Emissions of SO_2 (non-fossil-fuel combustion) and NH_3 are as in Park et al. [2004]. Other aerosol sources include elemental and organic carbon [*Bond et al.*, 2007], dust [*Fairlie et al.*, 2007], and sea salt [*Alexander et al.*, 2005].

Supplementary Figure S1 is analogous to Figure 2 in the main text, but shows total concentrations and subsequent exceedances in 1997 due to fires and all other sources. The spatial patterns of both $PM_{2.5}$ and O_3 are similar to the fires-only concentrations presented in the main text, indicating the strong influence of fire emissions relative to other sources on total concentrations.

Model Validation

Our model validation comes from three sources: daily visibility observations, annual $PM_{2.5}$, and hourly O_3 measurements (Supplementary Fig. S2). Due to the lack of long-term $PM_{2.5}$ ground monitoring stations in this region, visibility estimates are used to indicate changes in air quality degradation. Daily visibility data are available from the National Climatic Data Center Global Summary of the Day [*NCDC*, 2010]; we then reduced the impact of precipitation and human error on measurements with a monthly filter [*Husar et al.*, 2000]. Modeled $PM_{2.5}$ includes contributions from biomass burning and all other sources. There were 19 stations located in 13 grid cells; we averaged station data for the 6 grid cells with more than one station. Monthly modeled $PM_{2.5}$ values correlated well with the extinction coefficient derived from visibility measurements. The median R^2 was 0.42-0.67 for GISS-E2-Puccini and GEOS-Chem, with a slightly wider range of correlations for the GISS-E2-Puccini model (Supplementary Table S2). We also averaged Borneo stations and non-Borneo stations and plotted monthly time series comparisons between model

estimates and ground observations (Supplementary Fig. S3a). Modeled $PM_{2.5}$ concentrations reproduced the months with peak fire activity from the extinction coefficient time series, though the relative increases over baseline values in ground observations were better captured by the GISS-E2-Puccini model during the extreme 1997-98 concentrations.

Annual-average $PM_{2.5}$ values for 2005 were recorded at six urban ground stations in Indonesia, Malaysia, Thailand, and Vietnam from a set of observations assembled in support of the Global Burden of Disease Study (GBD 2010, http://www.globalburden.org/index.html) and compared with annual averages from each model (Supplementary Fig. S3b). Each model was generally low compared to station data but with only six stations available only in urban areas, data is too limited to draw firm conclusions. For example, without the single ground station observation of ~50 $\mu g/m^3$, ground observations and model data would become negatively correlated, illustrating the need for a larger set of validation data. We conclude that both models are producing conservative $PM_{2.5}$ concentrations in densely populated areas, consistent with the expectation that values would be higher from stations located in urban areas instead of large model grid boxes.

The World Data Centre for Greenhouse Gases maintains hourly O_3 measurements at two ground stations in our study area (http://gaw.kishou.go.jp/wdcgg/wdcgg.html). The Indonesian station is available from 1/1997-12/2007 and the Malaysian station is available from 9/1997-12/2001 (see Supplementary Fig. S2 for locations). Due to data storage constraints, we saved 1-2pm O_3 data for the GEOS-Chem model, 12-3pm O_3 from the GISS-

E2-Puccini model (the finest temporal interval available for output), and 24-hour averages from both models.

For calculating exceedances over WHO air quality guidelines and interim targets (Table S1), we used the 1-2pm concentrations as a proxy for the 8-hour maximum concentrations. Figure S4a shows the strong correlation between 1-2pm O_3 and the 8-hour maximum values, using the hourly values available from ground station data. For calculating O_3-related mortality, we used the 24-hour average concentrations as described in Bell et al. [2005]. We also compared monthly averages of 24-hour O_3 data with reported monthly O_3 station data (with a median of 24 days per month with station data). In the time series comparison, both models reproduce the monthly concentrations seen at the Indonesian site, which was closer to the fire source (Supplementary Fig. S4b). GEOS-Chem was consistently higher at both stations.

$PM_{2.5}$ Scaling Factors

We use satellite observations to help correct for model biases that arise from uncertainties in fire emissions and the representation of aerosol transport in our forward model estimates (Supplementary Fig. S5). While other studies have used satellite AOD to estimate surface-level $PM_{2.5}$ [*Van Donkelaar et al.*, 2010], we also incorporate differences between fire and non-fire aerosols by calculating separate scaling factors for each source. In our model runs, aerosol components include sulfate, black carbon, organic carbon, sea salt, and dust. Monthly column AOD from each model was first computed from runs with and without GFED3 fire emissions. After re-gridding satellite observations to model resolution, scaling factors for column-integrated fire and non-fire aerosols were calculated

separately for the top one-third of our spatial domain that had the highest mean annual levels of AOD, following the approach described in the Supplementary Material of Johnston et al. [2012]. The non-fire aerosol scaling factor was estimated from the 4 months of the annual cycle with the lowest contribution of fire aerosols to the total aerosol burden (1.02-1.05 for GISS and 1.56-1.96 for GEOS-Chem); the fire aerosol scaling factor was then estimated for the highest 4 months (1.36-1.53 for GISS and 2.01-2.26 for GEOS-Chem; Supplementary Fig. S5).

This method assumes that these areas and time periods are representative of the entire region and time period, although the composition of aerosol sources may differ. In addition, since satellites measure the quantity of aerosols in the atmospheric column, we must develop scaling factors from models based on column estimates. These factors are then applied to modeled surface concentrations that are of interest to population exposure, although the relationship may differ at the surface. We assume that aerosol emissions do not change the vertical profile of the aerosol mass concentration, and therefore the ratio of column AOD to surface aerosol concentration remains constant for a given region during the same season. This assumption may be invalid if the sources of the aerosol particles change substantially, either spatially or temporally. Compared to previous methods using AOD to scale the surface concentration, our approach treats fire and non-fire aerosols separately, which may partly reduce the uncertainty caused by this assumption. The difference between MODIS and MISR AOD also indicates some of the sampling issues with satellite-derived AOD. Satellite observations are made under clear-sky conditions that can be affected by various parameters such as cloud cover, biomass burning, and mineral dust

[*Van Donkelaar et al.*, 2010], which can cause gaps in AOD observations and bias monthly averages.

Additional Mortality Estimates

In order to provide a plausible range of mortality estimates and to present how sensitive our calculations are to the selected relative risk (RR) equation and choice of cause-specific mortality, we also evaluate the mortality burden due to 1) changes in the shape of the RR equation, 2) additional projected lung cancer deaths, and 3) short-term all-cause mortality summed over each year. These equations and the relationships that we use in the main text are summarized in Supplementary Table S3. We focus on cause-specific baseline mortality rates when possible because they are likely more similar than all-cause rates between developed countries at temperate latitudes (where most large-scale epidemiology studies are conducted) and tropical regions [*Ostro*, 2004].

First, in addition to the power-law relationship that we present in the main text, we compute cardiopulmonary mortality based on logarithmic and linear relationships between RR and exposure to $PM_{2.5}$. These alternative equations have been more widely used but do not account for extreme $PM_{2.5}$ concentrations; the epidemiological studies that they are based on did not have $PM_{2.5}$ observations more than 30 $\mu g/m^3$. For consistency, we recalculated the power-law relationship using baseline cardiopulmonary disease mortality rates (combination of cardiovascular and respiratory diseases) [*World Health Organization, Department of Measurement and Health Information*, 2011].

We first calculated cardiopulmonary mortality based on a log-linear relationship between RR and annual $PM_{2.5}$ concentrations following the approach given in the Environmental Burden of Disease study [*Ostro*, 2004]. This is given by:

(S1) Cardiopulmonary $RR=[(C_{fire}+1)/(C_{nofire}+1)]^{\gamma}$

where γ =0.1551 (0.05624-0.2541) [*Ostro*, 2004] and C_{fire} and C_{nofire} are annual average concentrations from our model results with and without GFED3 emissions. Excess mortality due to fire pollution is then calculated with equations (2) and (3) from the main text.

We then used a linear form of the RR equation, given by:

(S2) Cardiopulmonary $RR= \exp[\delta(C_{fire} - C_{nofire})]$

where δ=0.0128 (0.0077-0.0182) [*Krewski et al.*, 2009], applied only between the observed concentration range in the original epidemiological study of 5.8-30 $\mu g/m^3$. We then used equations (2) and (3) from the main text to calculate attributable cardiopulmonary disease mortality, which was between the log-linear and power-law results (Supplementary Fig. S6a and Table S4).

We also quantify the effect of long-term exposure on lung cancer mortality with three RR estimates. First, we use equations (1) through (3) from the main text with the power-law relationship between risk and $PM_{2.5}$ dose, but with α=0.3195 and β=0.7433 and baseline mortality rates for lung cancer [*Pope et al.*, 2011]. In addition, we separately calculate lung cancer mortality using the log-linear relationship from equation (S1), but with γ=0.232179 (0.08563-0.37873) [*Ostro*, 2004] and the linear relationship from equation (S2), but with δ=0.0142 (0.0057-0.0234) [*Krewski et al.*, 2009] and truncated between 5.8-30 $\mu g/m^3$. Mortality due to lung cancer was lower than cardiovascular disease;

the power-law relationship was generally more conservative than both log-linear and linear RR (Supplementary Fig. S6b and Table S4).

Finally, we calculate the burden of short-term exposure to air pollution on daily all-cause mortality, summed over each year. This helps us to understand how exposure to extreme daily concentrations impacts public health, in addition to specific outcomes from long-term exposure presented above [*Ostro*, 2004]. These all-cause results are not comparable to the results from Johnston et al. [2012] because this analysis uses daily exposure and corresponding RR only. The RR term is a linear relationship with an upper threshold of 125 $\mu g/m^3$ and follows equation (4) in the main text, but with δ=1% (0.6-1.5%) per 10 $\mu g/m^3$ increase in PM_{10} [*Ostro*, 2004]. We calculate attributable mortality with equations (2) and (5) from the main text. We convert $PM_{2.5}$ to PM_{10} using a ratio of 0.6 [*Cohen et al.*, 2004; *Ostro*, 2004] and apply to adults over 30 years, to remain consistent with our other estimates (Supplementary Fig. S6c and Table S4).

Comparison With Previous Estimates

Table S5 presents a summary of the methods used in our health impact analysis and assumptions that were made at each stage, using the best available methodologies. In addition, the following is a comparison of mortality estimates from Southeast Asia attributable to landscape fires in the global analysis of Johnston et al. [2012] and this region-specific paper (refer to Table 1 in Johnston et al. [2012] and Supplementary Table S6). The numbers are not directly comparable because they estimate different mortality burdens for different study regions: all-cause, all-age mortality for the WHO Southeast Asian region [*Johnston et al.*, 2012] versus cause-specific, adults-only mortality for the

ASEAN region. However, both studies show a remarkable correspondence in the difference between phases of the ENSO cycle, with approximately a sevenfold increase in mortality during El Niño relative to La Niña. Regardless, the estimates are substantially lower in this paper, largely attributable to the factors described below.

Data for Fire Emissions: Our study presents results from two atmospheric models using GFED3 fire emissions, which were 31% and 17% lower than GFED2 emissions in Southeast Asia and Equatorial Asia (see Van der Werf et al. [2010] for regional definitions).

Method for Concentration Estimates: We calculate health effects from two baseline models (GISS-E2-Puccini and GEOS-Chem) and four satellite-optimized model datasets, in order to retain a wider plausible range of concentrations. Johnston et al. [2012] merge estimates from GEOS-Chem and two satellite-optimized model datasets. The annual average concentrations reported in Table 1 for GEOS-Chem (baseline model and MISR and MODIS scaled results) are most similar to the Johnston et al. [2012] $PM_{2.5}$ estimates. They are on the lower end of our concentration range, but cannot be directly compared because our estimates also incorporate the reduced regional fire emissions in GFED3.

Concentration-Response Functions (CRF's): We used new power-law relationships between RR and $PM_{2.5}$ concentrations, which were developed only for cardiovascular disease and lung cancer mortality [*Pope et al.*, 2011]. This relationship is more conservative than using a linear CRF; by explicitly including data from very high concentrations of $PM_{2.5}$ based on studies of exposure to secondhand smoke and cigarette smoke, it avoids extrapolation of linear relationships to high concentrations that can overestimate mortality effects. This accounts for extreme pollutant concentrations that are

not observed in ambient air pollution concentrations in the U.S. (which are used to develop epidemiological relationships), but can be experienced in areas close to high fire activity.

Like some previous studies [*Anenberg et al.*, 2010], we do not include annual all-cause mortality because of the large differences in underlying conditions that drive baseline all-cause mortality rates between U.S.-based epidemiological studies and our study area. Furthermore, we applied this equation only to the adult population (~40% of the population [*UN*, 2011]), instead of to all ages as in Johnston et al. [2012]. The reason is that the power-law function was specifically derived from data for adults.

Our sensitivity analysis with a linear CRF [*Krewski et al.*, 2009] also follows a conservative approach and is not directly comparable to the results from Johnston et al. [2012]. We use a new linear CRF estimate and limit the effect between 5.8-30 $\mu g/m^3$, which was the concentration range observed in the original epidemiological study. Johnston et al. [2012] used an upper bound threshold of 50 $\mu g/m^3$ in the principal analysis.

Region Designation: Our mortality results have different regional definitions than Johnston et al. [2012]. The latter global study is separated by 21 WHO subregions; we use a rectangular delineation around ASEAN countries. While these are similar (see Fig. 2 of Johnston et al. [2012] and Fig. 1 in the main text), our study does not include the northern parts of this region, which border China and Bangladesh. The large model grid boxes make it difficult to partition countries within or outside of the study area; these areas have both high concentrations of fire emissions and high populations, so their inclusion will increase mortality estimates in the Johnston et al. [2012] estimates.

Estimate of Annual Mortality: We followed the approach of other modeling studies of pollution health impacts [*Ostro*, 2004; *Anenberg et al.*, 2010; *Schmidt et al.*, 2011]

that use the concept of the attributable fraction to attribute health impacts to a given increase in air pollutant concentrations. Johnston et al. [2012] instead determined whether areas were sporadically or chronically affected by fire, along with a counterfactual level of exposure (theoretical minimum).

Our estimates present 95% confidence intervals around the power-law relationship between RR and mortality. Since the Pope et al. [2011] study did not include confidence intervals for the reported relationship, we re-calculated the relationship using the upper and lower bounds around the individual RR estimates used in this study.

Additional Health Effects: In addition to annual mortality, we estimate the effect of fire concentrations on other health endpoints by analyzing the spatial distribution of daily exceedances over $PM_{2.5}$ and O_3 concentration thresholds. This is based on annual and 24-hour average $PM_{2.5}$ and 8-hour maximum O_3 concentrations, instead of only using longer-term average model output. Exceedances reference WHO air quality guidelines and interim targets, which combine the results of many epidemiological studies [*World Health Organization*, 2006].

Table S1. World Health Organization (WHO) $PM_{2.5}$ and O_3 air quality guidelines (AQGs, in bold) and higher interim target (IT) concentration levels. The WHO uses IT levels to summarize expected health risks for countries that cannot immediately achieve AQGs. Note that these guidelines are published by the WHO to assist policymakers in developing standards, but there is no clear evidence for thresholds below which no impacts can be expected [*World Health Organization*, 2006].

	Level	Averaging Time	Effects
$PM_{2.5}$	**25 µg/m³**	**24-hour**	**Air Quality Guideline (AQG)**
	37.5 µg/m³	24-hour	IT-3: 1.2% increase in short-term mortality over AQG
	50 µg/m³	24-hour	IT-2: 2.5% increase in short-term mortality over AQG
	75 µg/m³	24-hour	IT-1: 5% increase in short-term mortality over AQG
$PM_{2.5}$	**10 µg/m³**	**Annual**	**AQG**
	15 µg/m³	Annual	IT-3: Reduces mortality risk 6% over 25 µg/m³ IT-2.
	25 µg/m³	Annual	IT-2: Reduces mortality risk 6% over 35 µg/m³ IT-1
	35 µg/m³	Annual	IT-1: 15% long-term mortality risk increase over AQG
O_3*	**100 µg/m³***	**Max. daily 8-hour**	**AQG**
	160 µg/m³	Max. daily 8-hour	IT-1: 3-5% increase in mortality over AQG
	240 µg/m³	Max. daily 8-hour	High levels: 5-9% increase in mortality over AQG

*O_3 concentration: 50 ppb ≈ 100 µg/m³.

Table S2. R^2 values for monthly GISS-E2-PUCCINI and GEOS-Chem $PM_{2.5}$ with the monthly extinction coefficient from visibility observations. Results are presented for stations located in Borneo and other sites in the region, refer to Supplementary Figure S2 for specific locations.

	Location (°)	GISS	G-C
Non-Borneo	2.27, 102.25	0.66	0.63
	-6.08, 141.18	0.40	0.16
	0.47, 101.45	0.42	0.84
	Median	**0.42**	**0.63**
Borneo	1.22, 111.45	0.76	0.39
	4.93, 114.93	0.43	0.65
	1.48, 110.33	0.66	0.78
	2.12, 117.45	0.43	0.37
	-0.35, 111.78	0.75	0.71
	-0.95, 114.90	0.79	0.57
	-0.62, 117.15	0.11	0.14
	-1.85, 109.97	0.84	0.82
	-1.27, 116.90	0.19	0.20
	-3.43, 114.75	0.67	0.72
	Median	**0.67**	**0.61**

Table S3. Summary of the equations used to estimate mortality due to $PM_{2.5}$ exposure. Abbreviations are defined in main text and Supplementary Information.

Equation	Details	Source
Cardiovascular RR= $1+ \alpha(I*C)^{\beta}$	Equation developed for use over wide $PM_{2.5}$ dose range; apply to fire and no-fire runs separately to account for nonlinearity	Pope et al. (2011)
Cardiopulmonary RR= $[(C_{fire}+1)/(C_{nofire}+1)]^{\gamma}$	Log-linear relationship between RR and $PM_{2.5}$ exposure decreases risk at high concentrations relative to linear relationship	Ostro et al. (2004)
Cardiopulmonary RR= $\exp[\delta(C_{fire} - C_{nofire})]$	Truncated linear effect between observed concentrations in original study	Krewski et al. (2009)
Lung Cancer Mortality	Estimates an additional long-term cause-specific health impact due to $PM_{2.5}$ exposure	See above studies
All-Cause RR= $\exp[\delta(C_{fire} - C_{nofire})]$	Estimates short-term health impacts; daily $PM_{2.5}$ exposure relationship was developed for all-cause mortality	Ostro et al. (2004)

Table S4. Fires-only mortality using different $PM_{2.5}$ estimates for a strong El Niño year (1997) and La Niña year (2000). Total ASEAN cardiopulmonary disease (CPD) and lung cancer (LC) mortality due to fires only (x10^3 people), calculated from three separate equations (see Supplementary Table S3) with the range from 95% confidence intervals. GISS refers to GISS-E2-PUCCINI and G-C refers GEOS-Chem, both also with MISR and MODIS satellite scaling factors.

		Mortality (x10^3 people)			
		1997		*2000*	
		CPD	*LC*	*CPD*	*LC*
GISS	*Power*	12.1 (9.7-14.0)	1.7 (1.3-2.1)	1.2 (1.0-1.5)	0.1 (0.1-0.2)
	Log-linear	42.3 (16.5-64.8)	4.2 (1.7-6.2)	5.2 (1.9-8.4)	0.5 (0.2-0.9)
	Linear	30.9 (19.8-41.3)	2.3 (1.0-3.5)	0.0 (0.0-0.0)	0.0 (0.0-0.0)
G-C	*Power*	10.6 (8.3-13.1)	1.1 (0.8-1.5)	1.8 (1.4-2.3)	0.1 (0.1-0.2)
	Log-linear	41.2 (15.7-64.2)	4.1 (1.6-6.3)	7.8 (2.9-12.7)	0.8 (0.3-1.3)
	Linear	17.6 (11.2-23.6)	1.3 (0.6-2.0)	0.0 (0.0-0.0)	0.0 (0.0-0.0)
GISS MISR	*Power*	14.4 (11.7-16.5)	2.1 (1.7-2.6)	1.6 (1.3-2.0)	0.2 (0.1-0.2)
	Log-linear	49.4 (19.4-75.3)	4.8 (2.0-7.2)	6.8 (2.5-11.0)	0.7 (0.3-1.1)
	Linear	36.3 (23.2-48.6)	2.7 (1.2-4.1)	0.0 (0.0-0.0)	0.0 (0.0-0.0)
G-C MISR	*Power*	12.3 (9.9-14.4)	1.7 (1.3-2.1)	2.1 (1.7-2.6)	0.2 (0.2-0.3)
	Log-linear	45.1 (17.3-70.2)	4.5 (1.8-6.8)	8.9 (3.3-14.5)	0.9 (0.3-1.5)
	Linear	28.0 (17.9-37.6)	2.1 (0.9-3.2)	0.0 (0.0-0.0)	0.0 (0.0-0.0)
GISS MODIS	*Power*	15.2 (12.4-17.4)	2.3 (1.8-2.8)	1.8 (1.4-2.1)	0.2 (0.2-0.3)
	Log-linear	51.8 (20.3-79.0)	5.1 (2.1-7.5)	7.3 (2.7-11.9)	0.8 (0.3-1.2)
	Linear	40.5 (25.7-54.3)	3.1 (1.3-4.6)	0.0 (0.0-0.0)	0.0 (0.0-0.0)
G-C MODIS	*Power*	14.8 (11.8-17.5)	1.9 (1.5-2.4)	2.8 (2.2-3.4)	0.3 (0.2-0.4)
	Log-linear	54.4 (21.0-84.3)	5.4 (2.2-8.2)	11.9 (4.3-19.3)	1.2 (0.5-2.0)
	Linear	32.6 (20.7-43.8)	2.5 (1.1-3.7)	0.0 (0.0-0.0)	0.0 (0.0-0.0)
AVERAGE	***Power****	**13.2 (8.3-17.5)**	**1.8 (0.8-2.8)**	**1.9 (1.0-3.4)**	**0.2 (0.1-0.4)**
	Log-linear*	**47.4 (15.7-79.0)**	**4.7 (1.6-8.2)**	**8.0 (1.9-19.3)**	**0.8 (0.2-2.0)**
	Linear*	**31.0 (11.2-54.3)**	**2.3 (0.6-4.6)**	0.0 (0.0-0.0)	0.0 (0.0-0.0)

*Maximum error range.

Table S5. Summary of each stage of methods, the assumptions that were made, and the probable influence on our health impact estimates.

Method	Assumption	Direction of Uncertainty
Fire Emissions	Burned area detects most fires in the region	Uncertain; perhaps underestimate because missing small fires
Model structure	Large grid boxes representative of exposure	Mixed: possible underestimate in urban areas, overestimate in rural areas
Model concentration	Model accurately simulates surface concentrations	Potential underestimate: satellite AOD and ground $PM_{2.5}$ observations higher than model
PM Toxicity	Toxicity of fire $PM_{2.5}$ is similar to urban $PM_{2.5}$ from epidemiological studies	Uncertain: data is too limited on toxicity differences to use a specific biomass burning smoke equation
WHO guidelines	Concentration levels indicative of health effects	Underestimate: health effects likely occur below guideline levels
Cause-specific mortality	Focusing on diseases with direct impacts of fire emissions	Underestimate: impacts multiple additional health conditions
Adults-only mortality	Epidemiological equations were developed for adults, cannot apply to entire population	Underestimate: population under 30 years is a large fraction of population and infants and children are highly susceptible to air pollution
Concentration-response function	Power-law function is the best representation of mortality response	Possible underestimate: power-law function reduced mortality estimates compared with linear or log-linear functions

Table S6. Comparison of mortality estimation approach used by Johnston et al. (2012) and this study. Highlights the different components used to calculate the mortality burden for the Southeast Asian estimates given in the global analysis [*Johnston et al.*, 2012] and our results.

	Johnston et al. (2012)	**This paper**
Data for fire emissions	GFED2	GFED3
Method for concentration estimates	Merge GEOS-Chem model with two satellite AOD optimized results	Separate GISS and GEOS-Chem models, each with additional satellite AOD optimized results
Concentration-response function	Linear for all ages	Power law for adults only
Mortality included	All-cause (A-C)	Cardiovascular (CVD); Lung cancer (LC)
Region designation	WHO subregion	Rectangular area including ASEAN countries
Estimate of annual mortality	El Niño*: 296,000 A-C La Niña*: 43,000 A-C	El Niño**: 10,800 (6,800-14,300) CVD 1,800 (800-2,800) LC La Niña**: 1,600 (800-2,800) CVD 200 (0-800) LC

*September to August; **July to June

Figure S1. Modeled annual mean 1997 surface concentrations and corresponding daily exceedances in 1997 due to all emissions sources, including fires. a, $PM_{2.5}$ **b**, O_3 annual concentrations due to all sources and daily exceedances over World Health Organization interim targets (50 μg/m^3 daily $PM_{2.5}$ (IT-2) and 80 ppb 8-hour maximum O_3 (IT-1)). Annual concentrations are from 24-hour $PM_{2.5}$ and 8-hour maximum O_3. GISS refers to GISS-E2-PUCCINI and G-C refers to GEOS-Chem.

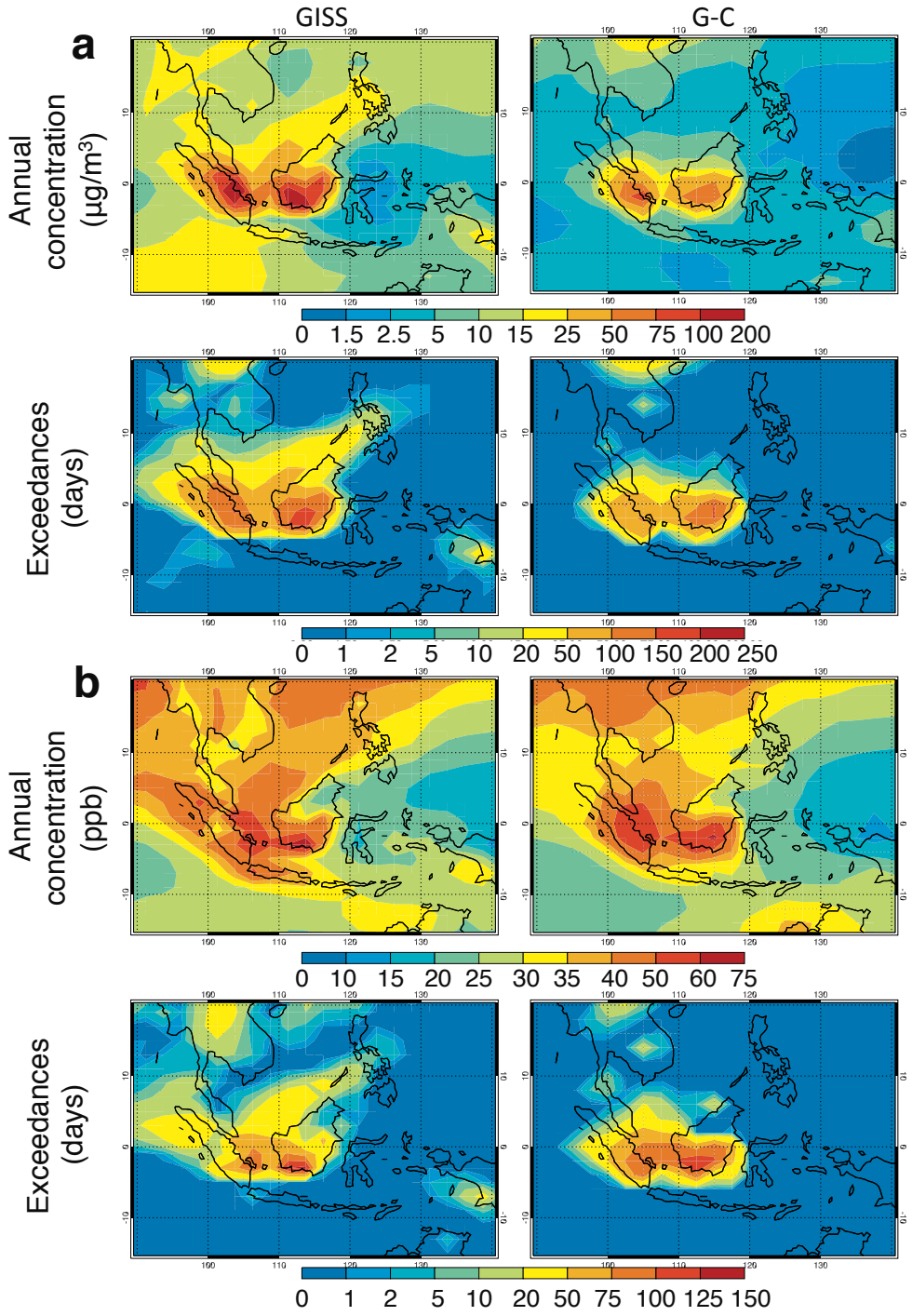

Figure S2. Locations of ground validation data. O_3 stations (white), urban $PM_{2.5}$ stations (gray), and visibility observations (black) are overlaid on the GISS-E2-PUCCINI fires-only 1997 annual average $PM_{2.5}$ concentrations for reference.

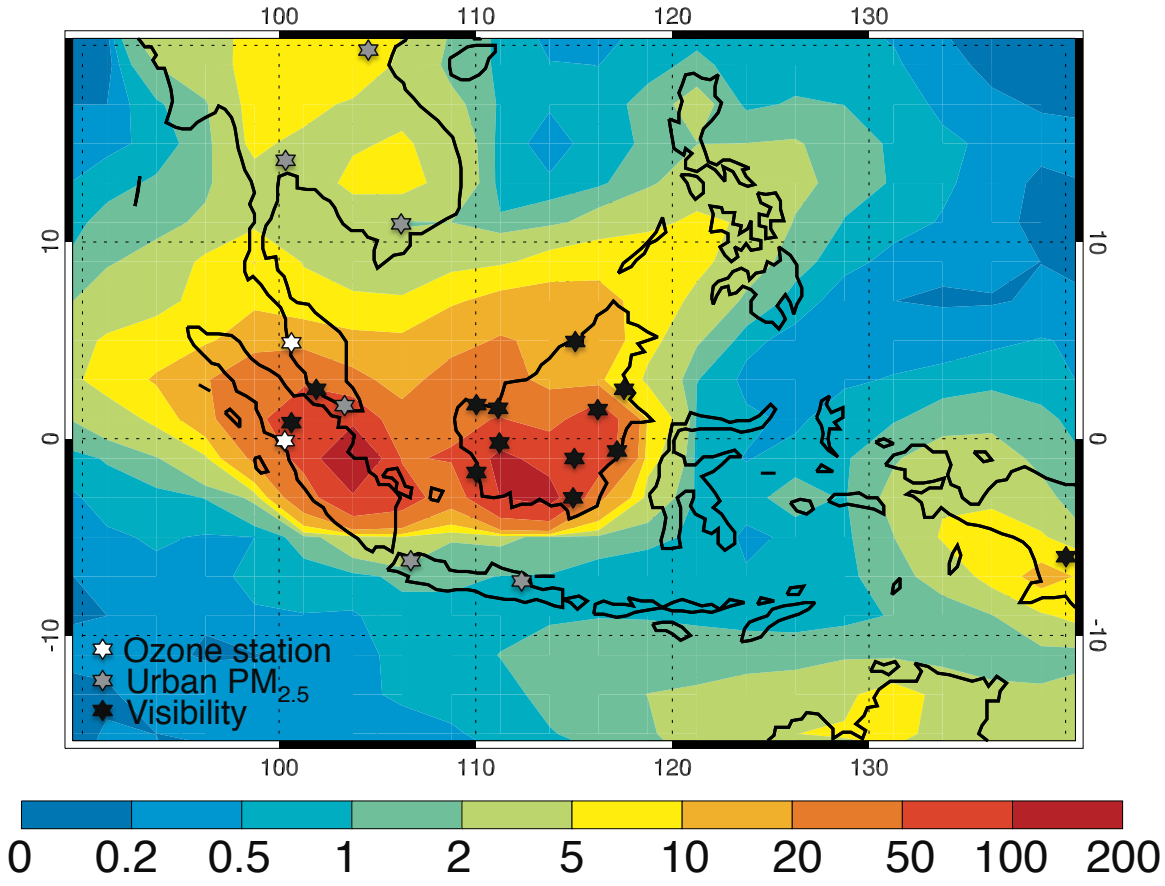

Figure S3. Modeled $PM_{2.5}$ comparison with monthly visibility observations and annual urban $PM_{2.5}$ stations. a, Monthly time series of the observed visibility extinction coefficient (in km^{-1}) and modeled $PM_{2.5}$ for Borneo stations (top) and non-Borneo stations (bottom). Ground observations from the National Climatic Data Center [*NCDC*, 2010]. **b**, 2005 annual $PM_{2.5}$ urban station measurements and annual modeled $PM_{2.5}$ results. Station data from the Global Burden of Disease study (GBD 2010, http://www.globalburden.org/index.html). Satellite-scaled estimates not shown.

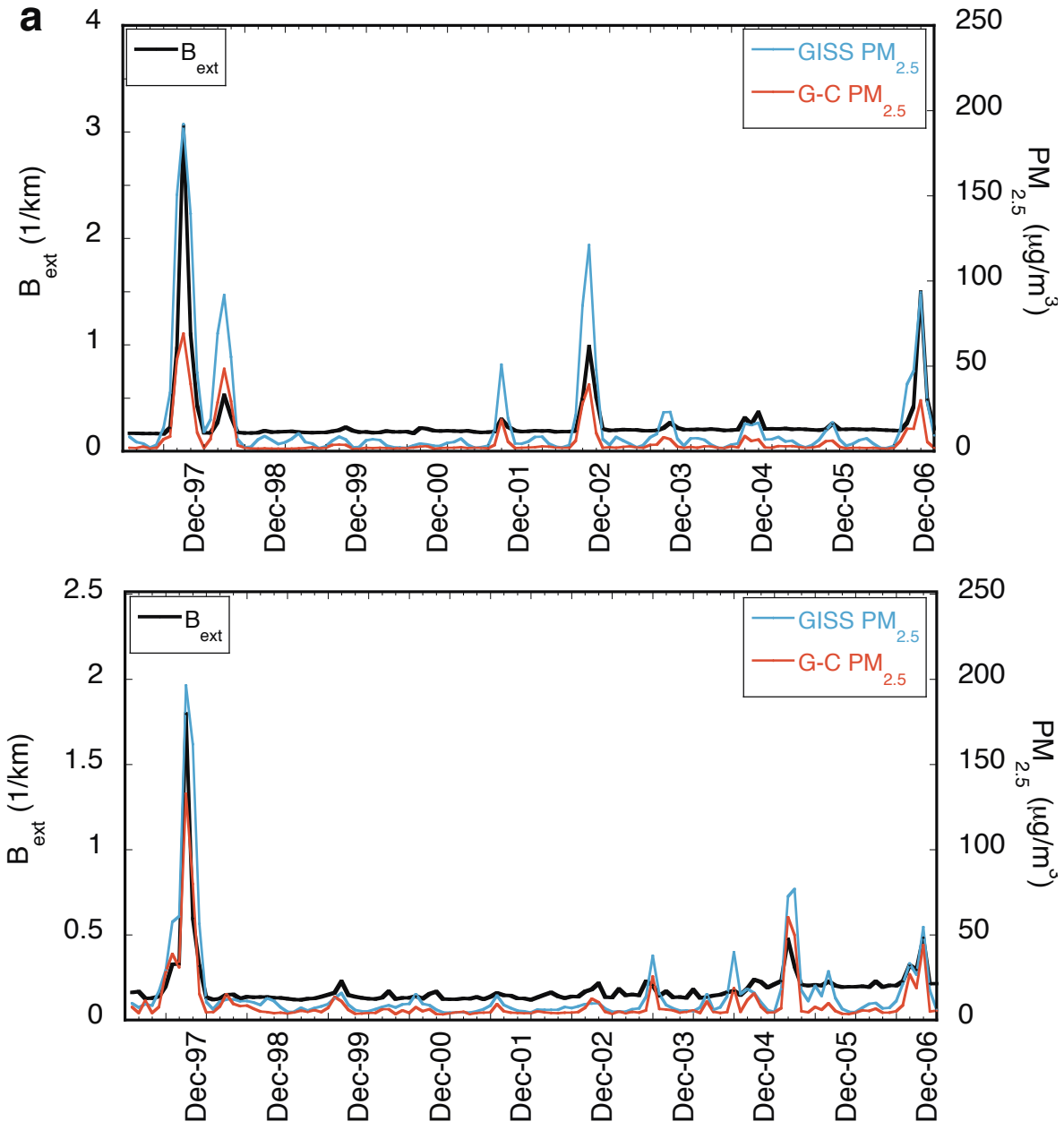

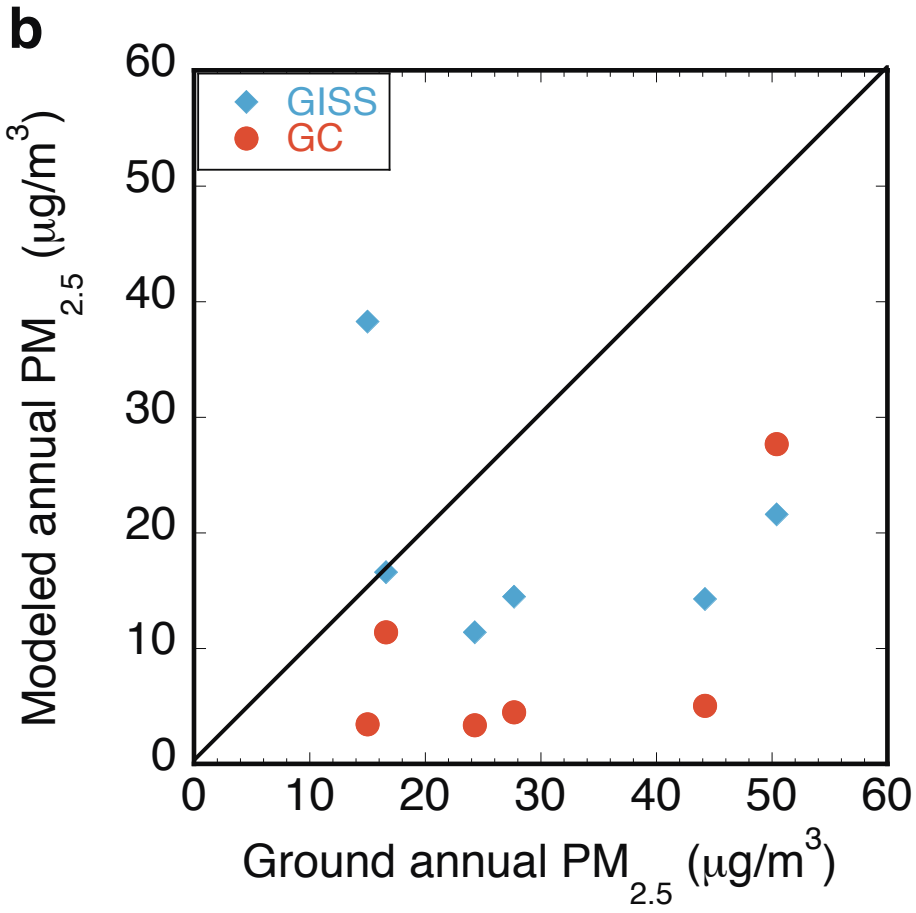
b
GISS
GC
Modeled annual PM2.5 (μg/m3)
Ground annual PM2.5 (μg/m3)
0
10
20
30
40
50
60

Figure S4. Modeled O_3 comparison with ground station observations. a, Comparison between 1-2pm and 8-hour maximum O_3 for January (left) and October (right) 1997 at the Bukit, Indonesia ground station. Strong correlation supports our use of modeled 1-2pm values as a proxy for the 8-hour maximum, which is needed for WHO exceedance calculations. **b,** Monthly average ground station and modeled O_3 for 1997-2006 in Bukit, Indonesia (left) and 1997-1999 Tanah Rata, Malaysia (right). Ground station data are from World Data Center for Greenhouse Gases (http://gaw.kishou.go.jp/wdcgg/wdcgg.html). GISS refers to GISS-E2-PUCCINI and G-C refers to GEOS-Chem.

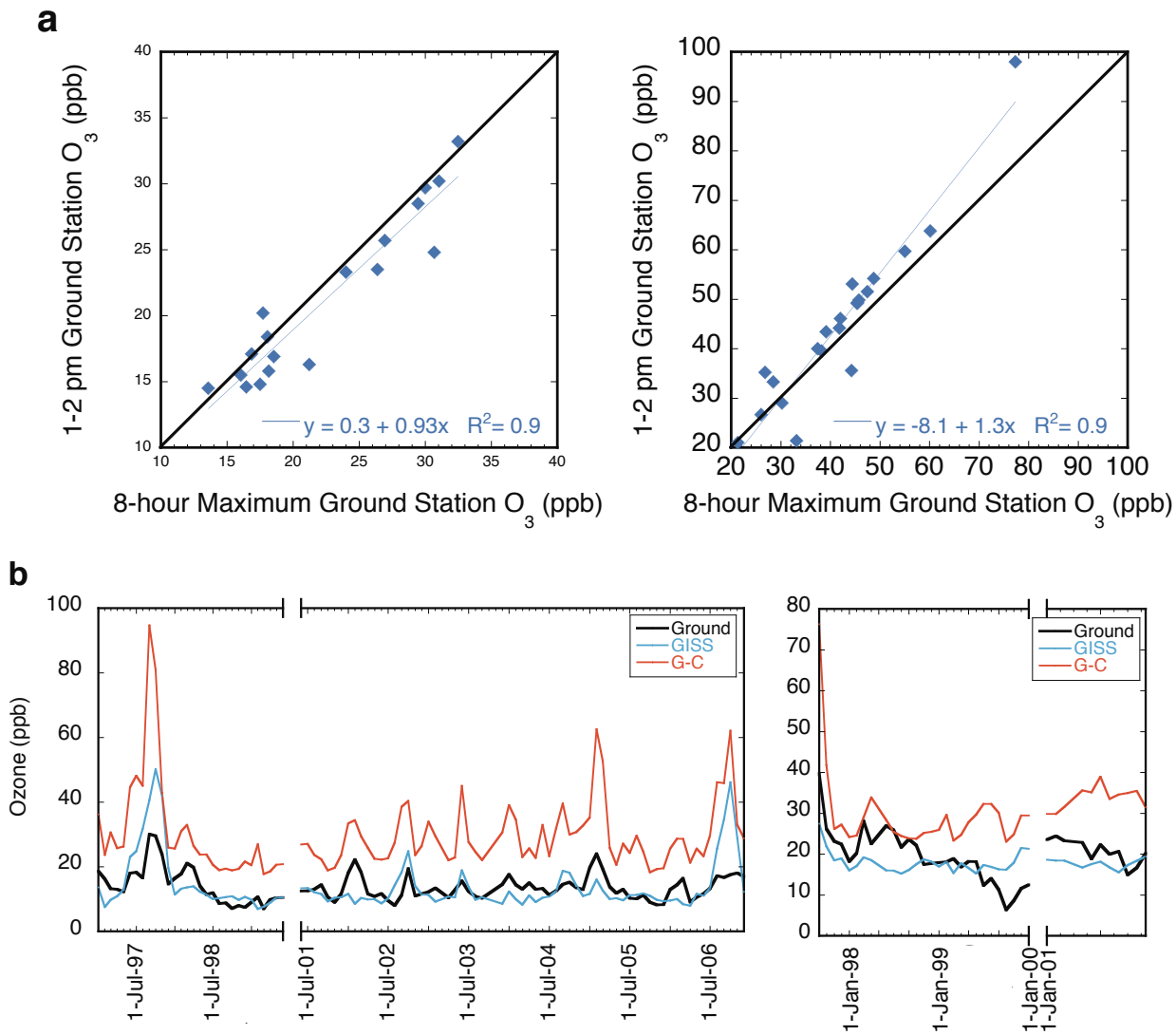

Figure S5. 2001-2006 monthly mean modeled AOD from fires and other sources for the top fire-affected area. a, GISS-E2-PUCCINI (GISS) results. **b**, GEOS-Chem (GC) results. First bar shows baseline model results without scaling factors and second and third bars, respectively, show model results after applying MODIS and MISR satellite constraints. Lines correspond to original MODIS and MISR AOD for reference.

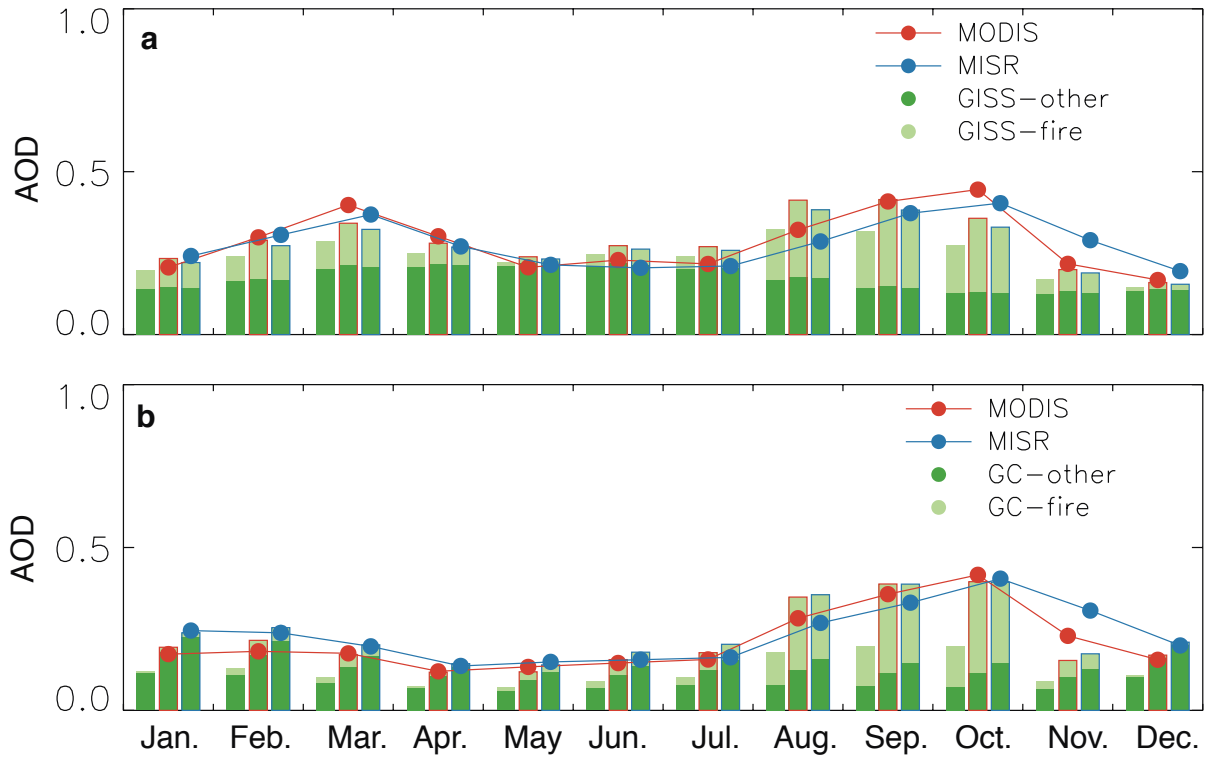

Figure S6. Sensitivity analysis of modeled annual mortality from fires-only $PM_{2.5}$ exposure. a,b, Cardiopulmonary disease (CPD) and lung cancer (LC) mortality from power, logarithmic, and linear relative risk equations. **c**, Annual sum of all-cause mortality from daily exposure. Results are from GISS-E2-PUCCINI only, which was a mid-range concentration estimate.

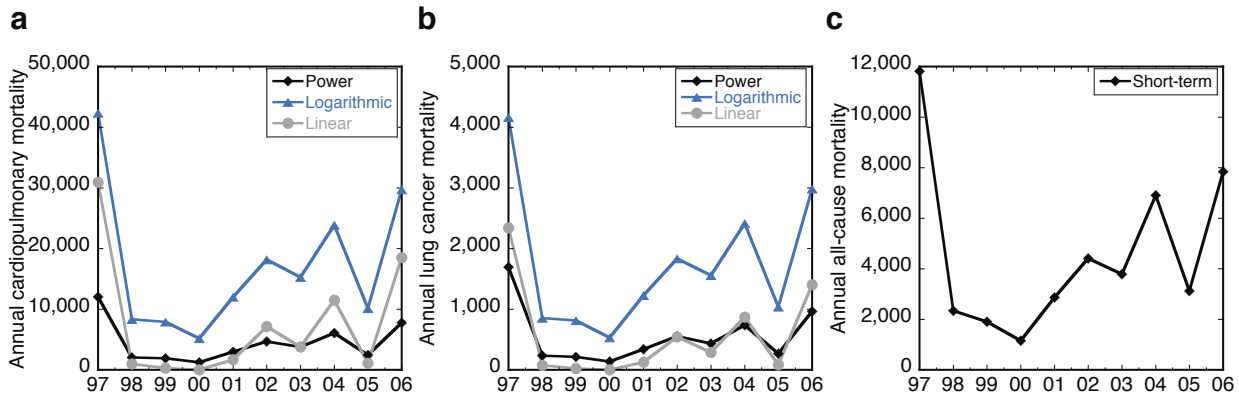

CHAPTER FOUR

Future fire emissions associated with projected land use change in Sumatra

Miriam E. Marlier, Ruth DeFries, Derric Pennington, Erik Nelson, Elsa Ordway, Jeremy Lewis, Shannon Koplitz, and Loretta Mickley

Submitted to *Global Change Biology* on November 25th, 2013

Abstract

Indonesia has experienced rapid land use change in recent decades as many forests and peatswamps have been cleared for more intensively managed land uses, including agriculture and oil palm and timber plantations. Fires are the predominant method of clearing and the subsequent emissions affect public health by contributing to regional particulate matter and ozone concentrations. Here, we examine emissions from fires associated with different land management and land use transition types on the Indonesian island of Sumatra, as well as the emissions' sensitivities to interannual meteorological variability. From 2005 to 2009, we find that a large proportion of Sumatra emissions (>80%) are associated with degradation or land use maintenance instead of immediate land use conversion, especially in dry years. We estimate future Sumatra emissions with five scenarios of land use change for the next two decades, using the Global Fire Emissions Database Version 3 (GFED3), detailed 1-km^2 land use change maps, and MODIS fire radiative power observations. Despite comprising only 16% of the original study area, we predict that the vast majority (33-48%) of future Sumatra emissions from land use change will occur in fuel-rich peatswamps unless this land cover type is protected effectively. This result indicates the importance of targeting remaining peatswamp forests for conservation in order to reduce the impact on future air quality and climate in Equatorial Asia. Results from this paper will be implemented in an atmospheric transport model to quantify the public health impacts from the transport of fire emissions associated with future land use scenarios in Sumatra.

1. Introduction

Equatorial Asia lost approximately 1% of total forest cover and 2.2% of peatswamp forest cover each year from 2000 to 2010, with estimates as high as 5% per year for lowland Sumatra [*Miettinen et al.*, 2011]. Within the Sumatran provinces of Riau, North Sumatra, and Jambi, forest cover declined from 93% to 38% of provincial area between 1977 and 2009. Almost half of this deforestation was attributed to industrial plantation establishment, primarily oil palm and timber plantations, and a further 16% went to smallholder agriculture [*Miettinen et al.*, 2012b]. Oil palm and timber plantation expansion has played an important role throughout Indonesia over the past few decades (Fig. 1). To the extent that these plantations are established on forested lands, fire emissions released during land use conversion can cause local and transboundary impacts on air quality, public health, and climate. Fire emissions from Equatorial Asia (mostly from the islands of Sumatra and Borneo) released an average of 128 Tg C per year between 2000 to 2006 [*van der Werf et al.*, 2008], which is of comparable magnitude to Indonesia's emissions from fossil fuel burning, cement manufacture, and gas flaring [*Boden et al.*, 2011]. Land-clearing fires also release fine particulate matter [*Heil and Goldammer*, 2001; *Marlier et al.*, 2013], which is dangerous from a public health standpoint.

High forest conversion rates in Indonesia are concerning from an emissions perspective not only because of the loss of aboveground biomass, but because tropical peatswamps contain rich belowground carbon stocks. Indonesian peatswamps alone are estimated to store at least 55 Gt C and are susceptible to fire after drainage [*Jaenicke et al.*, 2008]. Recent land use observations indicate that plantations in Sumatra and Kalimantan (Indonesian Borneo) are increasingly established on peatswamps instead of mineral soils

[*Miettinen et al.*, 2011; *Carlson et al.*, 2012]. One-fifth of peatswamps in Sumatra, Peninsular Malaysia, and Borneo (3.1 Mha) were converted to industrial plantations by 2010; 62% of these plantations were in Sumatra and mostly consisted of oil palm and pulpwood plantations [*Miettinen et al.*, 2012a]. Within Sumatra, Koh et al. [2011] estimate that 3.9 Mha of peatswamps were covered by mature oil palm plantations by the early 2000s, dominated by the Riau and South Sumatra provinces.

Fire incidence has increased along with the total area of peatswamps undergoing conversion. Long-term visibility measurements available since the 1960s indicate that major fire events in Indonesia did not occur simply because of droughts [*Field et al.*, 2009]. Instead, fires in wet tropical ecosystems generally require ignition sources from humans (e.g., fires set to clear forests in order to establish oil palm plantations). Further, human land use alters fire regimes by changing fuel availability, altering burning frequency, modifying spatial patterns of vegetation, and forcing regional climate change (at longer timescales) [*Bowman et al.*, 2009]. In Indonesia, direct causes of fire include land clearing, escaped fires, land tenure disputes, and resource extraction, along with underlying causes such as lack of fire-fighting capacity, inappropriate fire use by immigrants, and susceptibility of degraded forests [*Dennis et al.*, 2005] (see Figure 1 in Stolle et al. [2003] for a conceptual model). Native forests in this region are dominated by Dipterocarpaceae, which are not adapted to fires and have difficulty recovering due to thin bark, flammable resin, and low resprouting ability [*Goldammer*, 2006]. Degraded forests, with reduced canopy cover and evidence of logging, are also susceptible to burning due to drier fuels, so fire activity tends to be limited in pristine peatswamp forests and concentrated in heavily degraded areas [*Siegert et al.*, 2001; *Dennis and Colfer*, 2006; *Miettinen et al.*, 2012b]. A case

study in Kalimantan found that during the 1997 to 1998 El Niño 59% of logged forests were affected by fires versus 6% of undisturbed forests, and most burned area was concentrated on timber concessions, plantations, agriculture, and fallow land [*Siegert et al.*, 2001]. In general, degraded forests rarely return to more stable forest cover and generally represent a step on the trajectory of land conversion, by fire or some other clearing method. For example, from the 1970s to 2010 only 20% of Sumatra's degraded forests remained as forest [*Miettinen et al.*, 2012b]. Further, 7.25 of the 7.54 Mha of primary intact Sumatra forests that were deforested over 1990 to 2010 were degraded before being cleared [*Margono et al.*, 2012].

Along with anthropogenic drivers, the magnitude and duration of fire emissions exposure in Equatorial Asia depends on local meteorological conditions, which are strongly influenced by the El Niño-Southern Oscillation (ENSO) [*Marlier et al.*, 2013]. Seasonal precipitation controls groundwater levels and the amount of peat available for drying; the risk of intense fires in southern Sumatra and Kalimantan substantially increases when four month total precipitation drops below critical 350-mm and 650-mm thresholds, respectively [*Field and Shen*, 2008]. During drought stress, trees shed leaves and have lower moisture content [*Goldammer*, 2006]. The effect of the ENSO cycle has been observed in Borneo, where active fire detections can be two to three times higher during strong versus weaker El Niño events [*Wooster et al.*, 2012] and emissions can be up to 30 times higher [*van der Werf et al.*, 2008]. While Sumatra also has higher fire activity during droughts, there is also a trend of increasing fire emissions over time (rising by ~8 Tg C per year over 2000 to 2006) [*van der Werf et al.*, 2008].

Previously published projections of land use change in the region estimate continued rapid plantation development. For Equatorial Asia as a whole, one business-as-usual scenario estimates that 6 to 9 Mha of peatland will be converted to industrial plantations by 2020, compared with 2010 estimates of 3 Mha [*Miettinen et al.*, 2012a]. Several studies have focused on Kalimantan, where 1.1 Mha of deforestation is projected to occur by 2020, with associated carbon emissions strongly depending on the underlying biomass characteristics and assumptions about the spatial distribution of future plantations [*Fuller et al.*, 2011]. Carlson et al. [2013] found a 278% increase in oil palm plantations in Kalimantan from 2000 to 2010 (90% of which involved deforestation), despite 79% of government leases still remaining undeveloped. If all of these leases are developed using fire, oil palm expansion in Kalimantan will contribute 22% of Indonesia's total CO_2 emissions in 2020 [*Carlson et al.*, 2013]. In a recent projection of oil palm expansion from 2010 to 2050 in Indonesia, Malaysia, and Papua New Guinea, net cumulative carbon emissions from land use conversion and peat oxidation are estimated at 15 Pg CO_2 by 2050 under business-as-usual circumstances, with 77% of emissions from drainage of peat on existing or new plantations [*Harris et al.*, 2013].

In this paper, we address the issues raised above for the island of Sumatra, which has experienced rapid deforestation due to large-scale plantation development [*Miettinen et al.*, 2011] and is located near dense population centers. We build upon these prior works by combining spatially explicit economic models of future land use change with detailed estimates of the associated emissions from various types of fire. Specifically, we ask: 1) How are fire emissions associated with different land use management and transitions, 2) How does interannual meteorological variability impact these observed relationships, and

3) What are the projected emissions associated with future land use change scenarios, given various economic and policy assumptions? The future emissions inventories created in this study will be used in future research with a high-resolution atmospheric chemical transport model to estimate public health impacts resulting from transport of these emissions.

2. Materials and methods

We examined patterns of fires and past land use change to predict future fire emissions associated with several land use change scenarios for Sumatra. Our approach relied on five datasets: 1) 1-km^2 land use classifications for 2006 and 2009, 2) a dataset of biophysical and economic productivity information (circa 2004-2006) for each 1-km^2 pixel, 3) Global Fire Emissions Dataset version 3 (GFED3) 0.25° × 0.25° fire emissions for 2005 to 2009, 4) 1-km^2 Moderate Resolution Imaging Spectroradiometer (MODIS) fire radiative power observations (FRP) for 2005 to 2009, and 5) projected 1-km^2 land use at 3-year intervals until 2030. The role of each dataset is described below.

2.1 Past Land Use Observations

30-m^2 land use classifications of Sumatra for 2006 and 2009, based on Landsat and SPOT satellite observations, were produced by the Directorate of Forest Resources Monitoring and Inventory of Indonesia's Ministry of Forestry (MoF) [*MoF*, 2011]. The 2006 classification map was based on satellite images from 2005 and 2006 and the 2009 map was based on satellite images from 2009. MoF land use classification and zoning maps have been used by several previous studies [*Dennis and Colfer*, 2006; *Broich et al.*, 2011; *Gaveau*

et al., 2012; *Margono et al.*, 2012; *Romijn et al.*, 2013]. We simplified the MoF land use maps by condensing from 25 to 15 land use classes (Fig. 2, Table 1) and re-scaling to 1-km^2 resolution by assigning each 1-km^2 pixel the most dominant land use class within its boundaries. The matrix of land use transitions (Table 2) suggested several potential fire-driven transitions, especially from the forest, peatswamp, and savanna classes to the various types of plantations and agriculture. To translate this land use information into a fire emissions inventory, we needed to understand when these transitions occurred at a monthly temporal resolution suitable for atmospheric transport modeling and whether the transitions were likely driven by fire. We explored the role and timing of fires in land use change in the next step.

2.2 Past Fire Detections and Emissions

We associated the 2006 to 2009 land use transitions with concurrent GFED3 emissions. GFED3 is a monthly, 0.25° × 0.25° gridded fire emissions product that combines satellite observations of burned area with a biogeochemical model to estimate trace gas and aerosol emissions. Global average uncertainty is estimated at 20%, but is higher in Equatorial Asia because of uncertainties related to fuel consumption in peat areas and small fires that can be missed by the burned area detection algorithm. We addressed the latter with a correction factor for the contribution of small fires, as described below. GFED partitions emissions among general fire types, including grassland, deforestation, peat, agricultural waste, forest, and woodland [*van der Werf et al.*, 2010]. However, there were many 1-km^2 land use classes and transitions within each 0.25° × 0.25° grid cell, which comprises more than 700 1-km^2 pixels. This density of data necessitated an intermediate

step with finer spatial information on fire activity before attributing GFED3 emissions to detailed land use change.

To achieve this, we overlaid 1-km^2 observations of FRP onto the land use maps. FRP is the rate of electromagnetic energy released by a fire, from MODIS Aqua and Terra (MOD141+MYD14A1 products). FRP describes the rate of fuel consumption and can substitute for estimates of burned area, biomass density, and combustion completeness, although there are uncertainties regarding the partitioning of heat loss among various mechanisms and how this varies with fuel and fire type [*Wooster et al.*, 2005]. Fires in tropical ecosystems tend to peak in the afternoon [*Giglio*, 2007], but we summed FRP detected by both Terra and Aqua to capture a broader observational time period of fire activity (local overpass times of 10:30 am and 1:30 pm). By overlaying FRP with land use transitions (Table 2), we could understand which transitions were likely driven by fires and month-to-month variability in peak fire activity, by transition type. We could also estimate the proportion of 1) fires used during the land use conversion process, 2) maintenance fires that result in stable classes, and 3) unintentional fires that do not increase the economic returns of a given land parcel. We combined maximum FRP from Aqua and Terra for each land use transition class from January 2005 to December 2009 (such as the primary forest to timber plantation transition, for example) to cover the entire time period of the satellite data used in the MoF classification maps.

With this information on finer scale fires and land use transitions, we then incorporated 0.25° × 0.25° GFED3 emissions. First, we applied a correction factor to GFED3 for small fires that may have been missed in the baseline 500-m burned area datasets used in developing GFED3. In Equatorial Asia, this correction increased 2001-10 average fire

carbon emissions by 55% [*Randerson et al.*, 2012], which reflects the large proportion of small burn scars (<25 ha) that have been mapped in Equatorial Asia [*Miettinen and Liew*, 2009]. Each 0.25° × 0.25° GFED3 grid cell can include fire-driven land use transitions, fires that result in stable land use types, and/or transitions not associated with fires. To keep the non-fire transitions (such as manual clearing) from contributing to fire emissions, we allocated GFED fire emissions in proportion to the 1-km^2 FRP observations within the 0.25° grid cell for each land use transition type, so that only land use pixels associated with MODIS fire observations could contribute to our estimated GFED emissions for each land use transition. If active fires were missed by MODIS, estimated emissions will be higher for other active fire observations within the same GFED grid cells. If no active fires were observed in a grid cell with non-zero GFED emissions, then this cell will have no emissions in our downscaled product, though this effect was small (see Results). The downscaled estimates of GFED3 fire emissions were per 1-km^2 per month, for each transition type (225 possible transitions from 15 classes). When we applied these estimates to future scenarios, we assumed that the contribution of fires for driving each transition remains constant.

2.3 Interannual Variability in Emissions

The strong interannual variability in dry season precipitation emission was also reflected in total fire emissions (Table 3). We quantified the difference in emissions during a representative dry year and wet year (2006 and 2010, respectively) in order to appropriately consider this interannual variability in our future emissions estimates. We selected 2010 for this analysis because it is the first year after our 2009 land use map so we could assume that all of the documented change had already occurred. Burned area and

active fire products have different strengths and weaknesses: burned area is more affected by cloud cover, but the signal can persist for longer, whereas active fire detections are dependent on fires coinciding with the satellite overpass. To build on the strengths of each approach to measuring fire extent, we created a fire extent mask by combining the MODIS Burned Area Product (BAP) MCD64A1 data and MODIS FRP information, for the peak fire season of June to November of each year [*Miettinen et al.*, 2013]. Likely owing to the extensive cloud cover and reduced fire activity in 2010, the BAP data did not add any additional fire pixels to the fire extent mask for that year but increased the area by 300% in 2006. This suffices for our analysis since we focus on the relative differences in fire extent and emissions between wet and dry years rather than the absolute amount. By analyzing these results with land use types and transitions, it was possible to obtain a more nuanced understanding of the differences in emissions between dry and years for different land use transitions.

2.4 Future Fires

2.4.1 Future Land Cover Scenarios

We created projected land use maps for Sumatra from 2009 to 2030, with 3-year time steps, using an estimated random utility model (RUM) based on 2006 to 2009 land use change in Sumatra (see Supplementary Information for details about the model set-up). This model assumes the observed land use change is driven by land owners' or users' desire to maximize their land's net revenues (gross revenues less production costs and any land use conversion costs) over each time step, but also allows for unobserved personal preferences and cultural norms that can modify the maximization imperative [*Lawler et al.*,

n.d.]. Because of this unobserved model component, estimated RUMs give probabilistic results. For example, with the estimated RUM we were able to calculate the likelihood of a primary forest 1-km^2 pixel in 2006 remaining in primary forest or converting to secondary forest, plantation use, or agricultural use by 2009. The model did not incorporate climate change effects on land use.

We used modified versions of the 1-km^2 2006 and 2009 land use maps described in section 2.1 as the dependent variable in the RUM [*Nelson et al.*, n.d.]. We first consolidated primary and secondary mangrove forests (together representing ~1% of study area) with primary swamp forest, secondary swamp forest, and swamp classes into a broader peatswamp class. Second, we ignored all pixels classified as urban in either 2006 or 2009. We do not have the economic returns data necessary to model transitions to urban use (Table 1). Finally, the "other" class was removed from further analysis since this class includes clouds, beach, and water, and does not have associated economic data. Therefore, the RUM considered 10 land use possibilities instead of the 15 that exist on the 2006 and 2009 land use maps described in section 2.1.

To simulate land use change from 2006 to 2030 for our "Stable Prices" scenario, we first assigned each pixel its transition matrix vector according to its initial land use (2006 land use), district, soil quality, and zoning category (see Supplementary Information). Then, 2009 land use in each pixel was determined according to the pixel's transition matrix vector. Transition matrix vectors were reassigned across the landscape according to "new" initial land uses (the 2009 land use), districts, soil quality, and zoning categories and 2012 land uses across the island were determined accordingly, and so on. Finally, we overlaid the 0.25° × 0.25° GFED grid on the 1-km^2 maps of land use at each 3-year time step to

calculate the areal mix of land use types in each GFED gird cell at each time step. This scenario is called "Stable Prices" because it assumed that observed prices, zoning, and conservation protection from circa 2006 remain unchanged out to 2030.

To estimate land use change under alternative landscape conditions (e.g., different zoning patterns, different commodity market prices, etc.) we predicted every Sumatra pixel's 2006 to 2009 land use transition probabilities using the previously estimated RUM but with modified landscape data (Table 4). For example, for the "National Spatial Plan" scenario we modified the 2006 to 2009 zoning map according to government documents that detail the Indonesian government's plan for limited and unrestricted production forests, cultivated areas, urban uses, and conservation areas. With the new 2006 to 2009 landscape data, we predicted every Sumatra pixel's 2006 to 2009 land use transition probabilities with the previously estimated RUM and found the average transition possibility vector for each set of pixels grouped according to initial land use (2006 land use), soil quality, zoning category, and district. This new set of average transition possibility vectors became our "National Spatial Plan" transition matrix and was used, as described above for the "Stable Prices" scenario, to calculate the areal mix of land use in each GFED grid cell in 2009, 2012, and so on, out to 2030.

Other alternative scenarios we considered when estimating trajectories of land use at the GFED grid cell level for every three years from 2009 to 2030 include "Green Vision," "Peat Protection," and "High Oil Palm" (Table 4). Under the "Green Vision," 2006 to 2009 zoning maps are modified according to a sustainable development plan focused on ecosystem conservation endorsed by the Indonesian Ministry of Environment, Ministry of Public Works, Ministry of Forestry, and Ministry of Home Affairs, which re-zones areas in

Sumatra into important ecosystems for conservation, production areas with certification principles for sustainable development, and unrestricted development [*Roosita et al.*, 2010]. Under "Peat Protection" all pixels with peatswamp in 2006 were given protected status and fires were blocked from occurring. Finally, under the "High Oil Palm" scenario, we assumed that gross revenues from oil palm production increase by 30% by 2030, which mimics the observed trend since 2009 (http://faostat.fao.org/). See the Supplementary Information and Table 4 for more details on our land use change modeling procedures and land use change scenarios.

2.4.2 Future Fire Emissions

We applied the 1-km^2 estimates of observed fire emissions for each land use transition (as described in Section 2.2) to the future scenarios. We normalized total GFED emissions created by each type of land use transition by the area observed from 2006 to 2009 (Table 2). Although some future transitions will occur without fires (Table 5), we applied the average emissions per unit area to the predicted area of all individual land use changes within the 0.25° GFED grid cell. Separate emission factors (EF's) for deforestation, peatland, woodland, savanna, agricultural waste burning, and forest convert dry matter (DM) emissions to dozens of chemical species, which are provided by Andreae and Merlet [2001]. We matched our more detailed fire types from land use transitions to one of these six EF categories (Table 5).

There is a highly nonlinear relationship between fire emissions and dry season precipitation in this region [*van der Werf et al.*, 2008]; Table 3 shows the interannual variability between 0.5° dry-season precipitation and observed GFED3 emissions

(including small fires) for 2005 to 2010. We used this observed variability to understand how the contribution of different fire types could vary from year to year with future meteorology. The influence of near-term climate change on Equatorial Asia on this short a timescale is uncertain [*Collins*, 2005; *Christensen and Kanicharla*, 2014] and we do not include its effects. Instead we assume that the mean and variability of the meteorology observed during our 2005 to 2009 training period continues until 2030.

3. Results

3.1 Past Land Use Transitions

We estimated the role of fire in specific land use transitions by counting how many pixels within each transition class were associated with at least one MODIS FRP observation over 2005 to 09 (Table 6). This approach allowed us to observe which original 2006 land use classes were associated with the highest fire activity during transitions to other land use classes, as well as which final land use classes in 2009 were either created or maintained with fire. The 2009 land use types associated with the highest average proportion of fire were: secondary peatswamp forest, peatswamp, timber plantation, and clearing (all had fire proportions averaged over all transitions above 30%). Compared with all 2009 classes, the clearing class had the highest mean incidence of observed fires (44%), calculated by averaging all 2006 land uses that resulted in clearing by 2009.

MODIS FRP observations associated with land use transitions varied both among different land use classes and over time (Fig. S1; land use groupings described in Table 1). The time series of monthly FRP, normalized by the area of each transition with concurrent FRP observations, is shown for several examples in Figure 3. The highest FRP per unit area

was found in peatswamp areas (including mangrove forests, primary and secondary peatswamp forests, and peatswamp), and a consistent summer peak was evident in the peatswamp staying as peatswamp or transitioning to plantations. There were moderate FRP values in dryland forest transitions, along with a consistent summer peak near August of every year, and an absolute peak in summer 2006. The stable agriculture and plantation areas did not show as strong a seasonal dependence as did the peatswamp or dryland land use classes. We observed high FRP values in early 2005 in the agriculture, peatswamp, and mixed scrub classes that were unexpected and could be related to land use classification errors as described in Section 3.4. Overall, Figures 3 and S1 reveal three aspects of our FRP downscaling approach: 1) FRP variations by transition, with fuel-rich peatswamp fires contributing more than other fires to observed FRP per unit area, 2) interannual and monthly variations in the magnitude of FRP, and 3) specific land use groupings exhibiting a higher proportion of observed normalized FRP from non-transitions (stable peatswamp or stable dryland forest).

Higher burned area was observed in the dry versus wet year (2006 versus 2010), as we expected (Fig. 4). When stratified by land use transition, we found that a greater proportion of burned area in 2006 occurred in areas that transitioned from classes unassociated with agricultural production (including peatswamp and mixed scrub) than was observed in 2010. In 2010, there was a higher proportion of burned area in areas associated with productive land uses (including plantation and agriculture). This result suggested that higher emissions observed in dry years are more associated with unintentional fires, as indicated by greater correlation with burned areas transitioning to

non-productive land use types, or fires that do not directly result in conversion to productive use within the time period that we observed (Table 3).

3.2 Fire Emissions from Land Use Transitions

Total GFED emissions downscaled by MODIS FRP values indicated both interannual and monthly variation (Fig. 5). Annual emissions for all of Sumatra mirrored the original GFED with small fire emissions that were described in Table 3. Figure 5a shows that most emissions were observed during the dry conditions of 2006, as well as the enhanced contribution of specific land use groupings, especially carbon-rich peatswamp (land use groupings as described in Table 1). These totals show the emissions originating in these five major class groupings and transitioning to any other class. Emissions from the peatswamp class (including mangrove forests, peatswamp forests, and peatswamp) contributed more than 50% of total emissions during 2006, but a smaller fraction of total emissions during wetter years, such as 2005. Emissions from plantation classes remained relatively constant over all of the years. A large proportion of emissions were not associated with land use transitions observable over our time period (Fig. 5c); the peatswamp grouping had the largest proportion of emissions transitioning to another class (mixed scrub). Our estimates assume that non-transition emissions will continue at the same levels as observed during 2005 to 2009.

Sumatra-level emissions for all years (2005 to 2009) within a given month showed the strong variability over the course of the year in overall fire activity and fire type (Fig. 5b). Both the bulk of emissions and the contribution of peatswamp fires peaked during August, September, and October. Emissions from agricultural areas also peak during these

months, and burning in the mixed scrub classes (savanna and scrub, clearing, and urban) contribute the most during September and October. Overall, these results indicate that peatswamp areas will be the most vulnerable during the summer months of dry years.

3.3 Future Emissions from Land Use Change

The trends in total area within each class showed the influence that different land use policies can have for Sumatra, as well as the sensitivities of the RUM model to the economic and policy assumptions implemented in each scenario (Fig. 6). In the "Stable Prices" case (Fig. 6a), peatswamp was projected to continue decreasing over the next two decades, with smaller declines in dryland forests. Agriculture increased the most, followed by timber plantations and mixed scrub. The three land use classes that contain oil palm (oil palm/clearing/tree crop) showed slight increases over time, but not as steep as agriculture. In the "National Spatial Plan" (Fig. 6b), agriculture, timber plantations, and mixed scrub increased at the expense of peatswamp. There was also a large increase in urban areas in 2009 following new plans for urban zones by the Indonesian government, which is reflected in the mixed scrub class. The "Green Vision" scenario (Fig. 6c) had slower declines in peatswamp as well as recovery in dryland forests. Mixed oil palm, clearing, and tree crop, along with mixed scrub slightly decreased, with concurrent increases in timber plantations and agriculture. The "Peat Protection" scenario (Fig. 6d) helped the recovery of peatswamp areas but exhibited declines in dryland forests, while agriculture continued to increase. Finally, the increase in oil palm returns in the "High Oil Palm" scenario (Fig. 6e) drove steep declines in peatswamp and dryland forests (to a lesser degree), with large increases in the oil palm plantation, clearing, and tree crop class.

Figure 7a shows the percentage of forest cover (including dryland, mangrove, and peatswamp forests) for each 0.25° × 0.25° grid cell, for the same scenarios described above. All five scenarios indicated that most of the projected remaining forest is in the western part of Sumatra, which is dominated by dryland forests. There were varying degrees of remaining (mostly peatswamp) forest in the eastern part of Sumatra; the lowest forest cover was in the "High Oil Palm" scenario and the highest in the "Peat Protection" scenario. The "Green Vision" scenario also had higher retention of forests in eastern Sumatra, but since fires could still occur in these areas, fire emissions remained high (Fig. 7a+b).

Cumulative total emissions (2009 to 2030) showed that the eastern part of Sumatra dominated fire emissions over the next two decades due to emissions from peatswamp areas, which contributed to the bulk of emissions in all scenarios (Table 7). Our three-yearly estimates assume that meteorological conditions over our observational period are representative of the next two decades. The highest total emissions (3480 Tg DM from 2009 to 2030) were projected in the "High Oil Palm" scenario due to the increased contribution of fires from the clearing class (which includes logging concessions and oil palm), in addition to peatswamp fires. The "National Spatial Plan" followed with 3143 Tg DM in total emissions. The "Stable Prices" and "Green Vision" scenarios had similar lower emissions (2761 and 2786 Tg DM from 2009 to 2030), with differing contributions from the clearing class or savanna and bush scrub. The similarities were likely due to the "Stable Prices" scenario period of 2006 to 2009 coinciding with the global recession, when many commodity prices declined. The "Peat Protection" scenario had the lowest total emissions, 1435 Tg DM. Emissions time series for the next two decades showed the stark contrast between the "High Oil Palm" and "Peat Protection" scenarios (Fig. 8).

In Figure 9, the three-yearly emissions from the "High Oil Palm" scenario were partitioned into an annual time step, which illustrated the strong impact that applying interannual variability in meteorology can have on peak annual emissions totals. Here, we repeated the 2005 to 2009 meteorology for the next two decades and allowed the contributions of each fire type to vary according to the proportions of each fire type per year, as observed in Figure 5 (these relationships were also supported by our analysis of burned area in Figure 4). For example, for the 2009 to 2011 time period, we assigned meteorological conditions for 2009, 2005, and 2006, in that order. We then calculated the proportion of emissions that each year would contribute if that sequence of meteorology had occurred in the past, and scaled the 2009 to 2011 estimated three-yearly total accordingly. In Figure 9a, spikes in emissions estimates could change estimated population exposures to fire emissions, as opposed to the constant emissions in Figure 9b. The sum of all types of fire emissions is shown in Figure 9c, for constant three-yearly emissions and partitioning these same emissions to an annual time step using 2005 to 2009 meteorology. While we do not expect present-day meteorological conditions to continue into the future, these years offer a feasible representation of the interannual variability in meteorology and its effect on emissions. Future sensitivity cases will test the effect of different meteorological conditions.

3.4 Sensitivity Analysis

The multidisciplinary approach taken in this paper had several limitations. First, although the MoF land use classifications were crucial tools in this analysis, they did not have specific dates associated with the satellite images used for the classification process.

We therefore extended our temporal window from 2005 to 2009 to capture the full range of potential fire emissions associated with land use transitions. In addition, the land use classes comprising agriculture and plantations could be inconsistent across Sumatra because they represent the mix of specific crops, which can vary by province. Although the crops are split into broad groups (rice agriculture, non-rice agriculture together with mixed bush, other plantation, and timber plantation), there may be differences in fire management practices depending on the specific mix of crops.

In the emissions analysis which used FRP to downscale GFED emissions, there were also several potential sources of error. Since it is not possible to have monthly resolution land use maps covering all of Sumatra due to near-constant cloud cover in this region, we overlaid FRP and associated emissions data on the longest possible time period of land use change. We tested the sensitivity of this assumption by assuming that only January 2006 to December 2008 fires were relevant to the land use change maps, and found 34% lower cumulative emissions estimates (Table S2). Also, satellite overpasses may have missed fires or not coincided with the peak burning time, leading to underestimates of the contributions of the 1-km^2 pixels to 0.25° GFED emissions. We partially addressed the latter problem by combining MODIS Aqua and Terra FRP observations. Our downscaling approach did not capture all monthly GFED emissions (Fig. S2); some emissions were missed if there were no MODIS FRP observations within a GFED grid cell, such as when fire emissions were estimated in the GFED product through the burned area algorithm. If we scale our 1-km downscaled emissions estimates to match the monthly 0.25° GFED totals, our cumulative emissions estimates were 15% higher (Table S2). We also overestimated emissions in

January, February, and March because of high FRP values observed in early 2005 (Figs. 3+S1).

Peatswamp emissions were found to drive the majority of emissions in our future scenarios. Peat burning depth ranges from 0 to 50 cm in the GFED model for Indonesia, and was scaled according to soil moisture and fire persistence [*van der Werf et al.*, 2010], with a 30 cm average that compared well with a recent LIDAR study, which estimated an average peat burning depth in Central Kalimantan of 0.33 ±0.18 m [*Ballhorn et al.*, 2009]. We also addressed underestimates by GFED of Equatorial Asian fire emissions with the new dataset that quantifies the contribution of small fires [*Randerson et al.*, 2012].

We created five future scenarios to show how different economic and policy assumptions in the RUM affected our emissions estimates. The similar totals between the "Stable Prices," "National Spatial Plan," and "Green Vision" scenarios (2761-3143 Tg DM from 2009 to 2030) indicated that zoning changes proposed under the two spatial plans would do little to affect overall emissions. Instead, relatively drastic changes in protection of peatland areas ("Peat Protection" scenario) and market prices ("High Oil Palm" scenario) were found to affect emissions much more profoundly. Although the 30% increase in oil palm prices under the "High Oil Palm" scenario may seem extreme, recall that the period 2006 to 2009 (the years used to estimate the RUM of land use change) were global recession years, and prices for many commodities at the time were lower than normal. In a post-recession global economy, 30% higher palm oil prices could become the norm. All told, our five land use change scenarios offer realistic bounds on the Sumatra's 2009 to 2030 emission trajectory.

As mentioned above, we estimated the RUM of 2006 to 2009 land use change with a random sample of pixels. As part of a sensitivity analysis we estimated the RUM using a sample of evenly spaced pixels separated by 10-km. We did this to check whether unexplained spatial processes on the landscape affected our model results. The intuition here was estimating the model with pixels always separated by space would be less affected by spatial autocorrelation then the estimate with a random sample of pixels. However, both estimated coefficient and standard errors were similar with grid or random sampling, indicating spatial autocorrelation issues were minimal (see Table S1).

Finally, in the three scenarios that involved rezoning large protected areas in Sumatra – "Green Vision," "Peat Protection," and "National Spatial Plan" – we recognized that such shifts in supply of land available for commodity production are likely to have an impact on market prices. Increasing land scarcity in Sumatra will not have as much of effect on the prices of plantation products and rice because those products are produced and consumed on a global scale. Therefore, production will tend to move to available areas outside of Sumatra in reaction to stricter land controls rather than become involved in a competition for scarcer land in Sumatra. Local agricultural goods, however, are more likely to be produced and consumed on the island, and competition for land for these uses may be more intense, eventually causing product prices to rise. Therefore, we re-ran leakage cases for the "Green Vision," "Peat Protection," and "National Spatial Plan" scenarios with inflated gross revenues for several working land uses, representing local and global commodities, to reflect each scenario's increasing scarcity of Sumatra land zoned for intensive land use.

We have two gross revenue inflators for each leakage case to account for differences in the nature of produced products on Sumatra: non-rice agriculture (locally-traded

commodity) and rice and plantations (globally-traded commodity). We evaluated a range of percentage increases in revenues for local and global commodities for each alternative scenario. We then selected the percentage increases that resulted in one or more land use types having more area by 2030 relative to the "Stable Prices" scenario. For example, for one re-run of the "Green Vision" scenario, the low leakage scenario, we increased revenues from non-rice agriculture by 8% and revenues from plantations and rice agriculture by 2.5%. This meant that two land uses, timber plantation and non-rice agriculture, had more area on this version of the 2030 map than they did on the "Stable Prices" 2030 land use map. For a second re-run of the "Green Vision" scenario, the high leakage scenario, we increased revenues from non-rice agriculture by 15% and revenues from plantations and rice agriculture by 10%. For this case, three land uses – timber plantation, non-rice agriculture, and logging concessions – had more area on the 2030 "Green Vision" map than on the "Stable Prices" 2030 land use map. The range of cumulative emissions calculated from the two leakage cases was 2782 to 2861 Tg DM, compared to 2786 Tg DM for the "Green Vision" without leakage effects (Table S3).

For leakage analysis of the "Peat Protection" and "National Spatial Plan" scenarios, revenue was increased by 5% for non-rice agriculture and 2.5% for plantation and rice production in one case and 15% and 8%, respectively, in the other case. For the "Peat Protection" scenario, the cumulative emissions from the two leakage cases were 1401 and 1424 Tg DM, compared to 1435 Tg DM without leakage effects (Table S4). For the "National Plan" scenario, the cumulative emissions from the two leakage cases were 3159 and 3206 Tg DM, compared to 3143 without leakage effects (Table S5). While accounting for leakage

almost always increases emissions, it never increases more than 2.7% compared to the versions of these scenarios with no leakage.

4. Discussion

An often ignored issue in tropical land use policies is the public health impact of emissions from fire-driven deforestation. We examined how different market conditions and land use policies to protect natural forests and limit agriculture, forestry, and plantation growth will affect predicted trajectories of fire-based emissions from Sumatra (Fig. 6). As illustrated in Figure 7 and Table 7, the examined land development strategies in Sumatra were associated with varying patterns of forest conservation and potential associated fire emissions from burning. Our analysis makes it clear that cumulative emissions out to 2030 will remain high regardless of the amount of dryland forest protection unless strong protections for peatswamp areas are also implemented. Across the four scenarios that do not include peatswamp conservation, we found a range of 2761 to 3480 Tg DM of cumulative emissions from 2009 to 2030, with peatswamp fires contributing 33-48% of total emissions. When peatswamp areas were protected, 2009 to 2030 cumulative emissions decreased to 1435 Tg DM. These ranges indicated that fire emissions associated with our scenarios are less sensitive to the various economic and policy assumptions than to fires in peatswamp areas with high fuel loads. Compared with the business-as-usual cumulative emissions estimate from land use conversion and peat oxidation of ~2000 Tg DM (converted from reported CO_2 units) for Sumatra by 2050 from Harris et al. [2013], our range of 2761-3480 Tg DM by 2030 (in our scenarios without peat protection) is higher. This can be attributed to including emissions from peat fires,

considering conversion to land uses other than oil palm plantation, and incorporating emissions from fires that do not result in immediate conversion.

Detailed information on how specific land use transitions were associated with fire (Figs. 3+5, Table 5), along with the most vulnerable times for fire activity, could be used to inform on-the-ground policies to restrict burning. While a zero burn policy does not give smallholders alternative methods to clearing land, identifying low risk conditions for burning that help contain fires could reduce the impact [*Dennis et al.*, 2005]. For example, the contribution of emissions from peatswamp and mixed scrub areas peaked in drier years (such as 2006) and during the driest part of the year (September and October). We find that the majority of emissions were not from forest conversion directly, but from fires in highly susceptible degraded areas, which might be unintentional or related to the initial stages of the clearing process. This confirmed previous findings that fires in Sumatra are concentrated in degraded land use types and limited in intact natural ecosystems [*Margono et al.*, 2012; *Miettinen et al.*, 2012b] and protecting these areas from ignition sources is crucial to reducing emissions.

Our research is part of a larger project that will quantify local and transboundary public health benefits associated with ecosystem conservation in Sumatra. To appropriately compare with the economic benefits of plantations, the full value of ecosystem services provided by forests will be undervalued without accurate quantification of the public health costs associated with exposure to emissions from deforestation and degradation fires (other important costs not considered here include depleted carbon stocks, biodiversity declines, and water quality [*Naidoo et al.*, 2009; *Barano et al.*, 2012]). The future fire emissions inventories described in this study will be

used in an atmospheric transport model to simulate future exposure to transported fire emissions and associated public health impact. In these simulations, it is imperative to consider the interactions between future fire emissions and future meteorological conditions (Figure 9). Our three-yearly emissions estimates assumed that the observed meteorological variability from 2005 to 2009 continues until 2030; we will test the sensitivity at the annual level by partitioning emissions according to different combinations of meteorological conditions. For example, a strong drought year followed by two wetter years would be expected to concentrate fire-driven land use change in the first year with less change attributed to the following two years. In addition, the approach taken by this paper can be extended to other parts of Indonesia that constitute the frontier of plantation development, especially Kalimantan and Papua, and to land use fires in other parts of the world.

Acknowledgements

The authors are grateful to Samuel Myers, Daniel Jacob, Joel Schwartz, and Patrick Kim for helpful discussions on this work. We also thank Guido van der Werf, Jim Randerson, and Yang Chen for their assistance with using the GFED3 small fires dataset, Belinda Margono for additional information about the Indonesian Ministry of Forestry classification maps, Mike Anderson assistance with Geographic Information System, and Barano Siswa Sulistyawan and World Wildlife Fund–Indonesia for providing base data. This work was partially supported by the NSF Graduate Research Fellowship Program. We also thank the Health & Ecosystems: Analysis of Linkages (HEAL) program for helping to make this work

possible. We are extremely grateful for support provided to HEAL by The Rockefeller Foundation and the Gordon and Betty Moore Foundation.

TABLES AND FIGURES

Table 1. Land use classes and management assumptions from Indonesian Ministry of Forest 2006 and 2009 classification maps [*MoF*, 2011]**.**

LULC	Dominant Class	Land Management Assumptions	Groupings For Fire Analysis	Classes For Econometric Analysis
1	Primary dryland forest		Dryland forest	Primary dryland forest
2	Secondary dryland forest		Dryland forest	Secondary dryland forest
3	Mangrove forest	Primary and secondary mangrove forests	Peatswamp	Peatswamp
4	Primary swamp forest		Peatswamp	Peatswamp
5	Secondary swamp forest		Peatswamp	Peatswamp
6	Swamp		Peatswamp	Peatswamp
7	Savanna and bush scrub		Mixed scrub	Savanna and bush scrub
8	Timber plantation	Mix of logging: 50% saw logs and 50% pulp	Plantation	Timber plantation
9	Other plantation	Weighted average mix of top 5 tree crops by area; includes oil palm	Plantation	Other plantation (*includes oil palm*)
10	Non-rice agriculture, mixed bush	Average 50% non-rice agriculture and 50% mix of top 5 tree crops by area; includes oil palm.	Agriculture	Non-rice agriculture, mixed bush (*includes oil palm*)
11	Non-rice agriculture	Weighted average mix of top 5 crops by area	Agriculture	Non-rice agriculture
12	Rice agriculture	Rice paddy	Agriculture	Rice agriculture
13	Urban	50% mix crop and bush; 50% developed	Mixed scrub	N/A (assumed static)
14	Clearing	Cleared land, logging for saw logs, and plantations (including oil palm)	Mixed scrub	Clearing (*includes oil palm*)
15	Other	Water, cloud, beach	N/A (no data)	N/A (no data)

Table 2. Area (in km²) for the 15 land use classes in 2006 (rows) and 2009 (columns). Class codes refer to descriptions in Table 1. Blank cells had no area in that transition class.

	1	2	3	4	5	6	7	8	9	10	11	12	13	14	15	Total
1	19712	1345			14	1	47	10	5	112	6	8		2	28	21290
2	1115	61473	3		313	70	1858	570	178	1583	256	38	9	692	151	68309
3			2823		10	187	26		52	35	10	17	6	11	108	3285
4				2749	261	40			27					72	4	3153
5		27	12	3071	19336	1721	120	874	565	155	43	19	5	2120	116	28184
6		120	209	41	1156	28392	282	206	626	427	277	359	47	503	350	32995
7	9	2042	69		342	431	23197	230	634	2143	729	354	74	214	176	30644
8	2	177			51	55	594	7547	395	386	74	3	16	476	35	9811
9	10	173	30		154	399	706	883	46313	1232	569	626	353	712	180	52340
10	20	1304	57		199	665	2966	251	2160	82478	2353	1608	549	513	547	95670
11	4	437	31		53	248	1153	101	557	2559	30919	1626	607	277	263	38835
12		54	13		12	130	118	6	108	530	270	10312	163	93	101	11910
13		5	4		8	52	49	10	182	380	315	152	5737	39	57	6990
14	3	126	14		78	176	1049	654	495	411	162	73	43	4672	81	8037
15	428	4659	318	194	213	546	716	389	925	2858	542	228	224	340	13219	25799
Total	21303	71942	3583	6055	22200	33113	32881	11731	53222	95289	36525	15423	7833	10736	15416	437252

Table 3. July to November average precipitation (in mm/month) and total emissions (in Tg DM/year) over the Sumatra land area. Fire-affected area in forest (dryland, mangrove, peatswamp forests, or peatswamp) and non-forest (plantation, agriculture, urban, clearing, scrub) for 2006 (dry year) and 2010 (wet year), based on 2006 and 2009 land use maps, and 2006 and 2010 burned area mask, respectively. Precipitation data are from the GEOS-5 assimilated meteorology from the NASA Global Modeling and Assimilation Office (GMAO).

Year	Precipitation (mm/month)	Emissions (Tg DM/yr)	Fire Area in Forest (km^2)	Fire Area in Non-Forest (km^2)	Forest : Non-Forest Fire Area
2005	85.6	56.0			
2006	65.2	209.7	1.35E+04	1.68E+04	0.80
2007	81.9	26.2			
2008	86.7	46.9			
2009	77.8	69.1			
2010	94.6	14.1	1.76E+03	3.08E+03	0.57

Table 4. Description of future scenarios and associated assumptions about future trends in land use zoning, economic returns, and tax or subsidy policies.

Scenario	Description
Stable Prices	Assumes market, economic, political, and social conditions observed from 2006 to 2009 in Sumatra, Indonesia, and globally continue until 2030.
National Spatial Plan	Re-zones Stable Prices scenario using Indonesian government spatial plan, which includes conserved forests, working forests that cannot be cleared, and unrestricted zoning classes. New urban areas are added in 2009 since we do not have information on how these areas will be implemented over time. This plan was established by Government Regulation Act No. 26 2007 and Act. No. 26 2008, which established the National Spatial Plan (RTRWN) and were developed by the Ministry of Public Works (Kementerian Pekerjaan Umum).
Green Vision	Implements WWF sustainable development plan, which changes zoning for different land uses to conserve forested areas. Incorporates leakage effects by increasing revenues in areas where agriculture or plantation conversion is permitted.
Peat Protection	Places all peatswamp forest, mangrove forest, and peatswamp in protected area zones and blocks fires from occurring in these areas.
High Oil Palm	Increases annualized gross revenues for land uses containing oil palm by 30% (includes other plantation, non-rice agriculture with mixed bush, and clearing). Observed revenues for model training data from 2006-09 were during the global recession, so the model mimics a market where oil palm revenues increased at current rates.

Table 5. GFED fire types and corresponding land use classes.

GFED Fire Type	Included Land Use Classes
Deforestation	Primary and secondary dryland forest
Peatland	Primary and secondary mangrove forest; primary and secondary swamp forest; swamp
Woodland	Timber plantation; other plantation
Savanna	Scrub and savanna; clearing; urban
Agricultural waste burning	Non-rice agriculture with brush; non-rice agriculture; rice agriculture
Forest	None

Table 6. Proportion of pixels within each transition class associated with at least one MODIS FRP observation over 2005-09. Columns are 2006 classes and rows are 2009 classes. Refer to Table 1 for class names and Table 2 for areas within each transition. Blank cells had no area in that transition class with fire. Colors correspond with 2006 class groupings as in Figure 3.

	1	2	3	4	5	6	7	8	9	10	11	12	13	14	15	Mean
1	0.01	0.03			1	1	0.06	0.6	0.4	0.1	0.17	0		0.5	0	0.19
2	0.03	0.1	0.67		0.26	0.19	0.2	0.43	0.38	0.27	0.23	0.13	0.33	0.58	0.25	0.2
3			0.03		0.1	0.02	0.08		0.02	0.09	0	0.18	0	0.18	0.06	0.2
4				0.05	0.39	0.35			0.67					1	0	0.21
5		0.19	0.08	0.04	0.3	0.48	0.58	0.43	0.55	0.52	0.72	0.37	0.8	0.78	0.42	0.22
6		0.33	0.03	0.05	0.23	0.42	0.41	0.27	0.39	0.34	0.21	0.21	0.19	0.55	0.28	0.21
7	0	0.13	0.04		0.23	0.47	0.27	0.31	0.27	0.24	0.21	0.1	0.19	0.46	0.26	0.2
8	0	0.17			0.24	0.31	0.22	0.32	0.33	0.29	0.2	0	0.44	0.28	0.43	0.19
9	0.5	0.31	0.1		0.48	0.37	0.22	0.45	0.16	0.2	0.11	0.06	0.07	0.49	0.23	0.16
10	0.3	0.14	0.05		0.34	0.29	0.14	0.22	0.15	0.23	0.09	0.07	0.11	0.38	0.21	0.15
11	0	0.09	0.03		0.34	0.31	0.12	0.16	0.07	0.1	0.13	0.07	0.08	0.16	0.13	0.14
12		0.02	0.15		0.25	0.21	0.08	0.17	0.07	0.04	0.04	0.1	0.15	0.15	0.08	0.14
13		0.4	0		0.25	0.27	0.14	0.4	0.1	0.1	0.06	0.11	0.1	0.28	0.16	0.16
14	0	0.27	0.14		0.54	0.45	0.21	0.39	0.33	0.32	0.28	0.15	0.07	0.44	0.17	0.16
15	0.03	0.13	0.07	0.01	0.24	0.26	0.26	0.35	0.23	0.29	0.18	0.07	0.13	0.43	0.12	0.15
Mean	0.1	0.18	0.12	0.04	**0.35**	**0.36**	0.21	**0.35**	0.27	0.22	0.19	0.12	0.2	**0.44**	0.19	

Table 7. Cumulative total fire emissions (in Tg DM), by fire type, for five future scenarios over 2009-2030 (description of scenarios in Table 4).

Land Use Class	Stable Prices	Spatial Plan	Green Vision	Peat Protection	High Oil Palm
Primary dryland forest	1	1	1	1	1
Secondary dryland forest	69	71	70	69	69
Peatswamp	1223	1205	1334	0	1143
Savanna and bush scrub	371	369	367	356	309
Timber plantation	77	88	82	61	55
Other plantation	217	201	213	205	203
Non-rice agriculture, mixed bush	247	235	237	244	267
Non-rice agriculture	80	72	75	78	68
Rice agriculture	75	65	61	73	64
Clearing	307	283	253	257	1209
Urban	93	555	93	93	93
Total	**2761**	**3143**	**2786**	**1435**	**3480**

Figure 1. Oil palm and wood pulp production (in million tonnes) for all of Indonesia from 1990 to 2012 (accessed on 10/1/2013 at http://faostat3.fao.org/faostat-gateway/go/to/home/E).

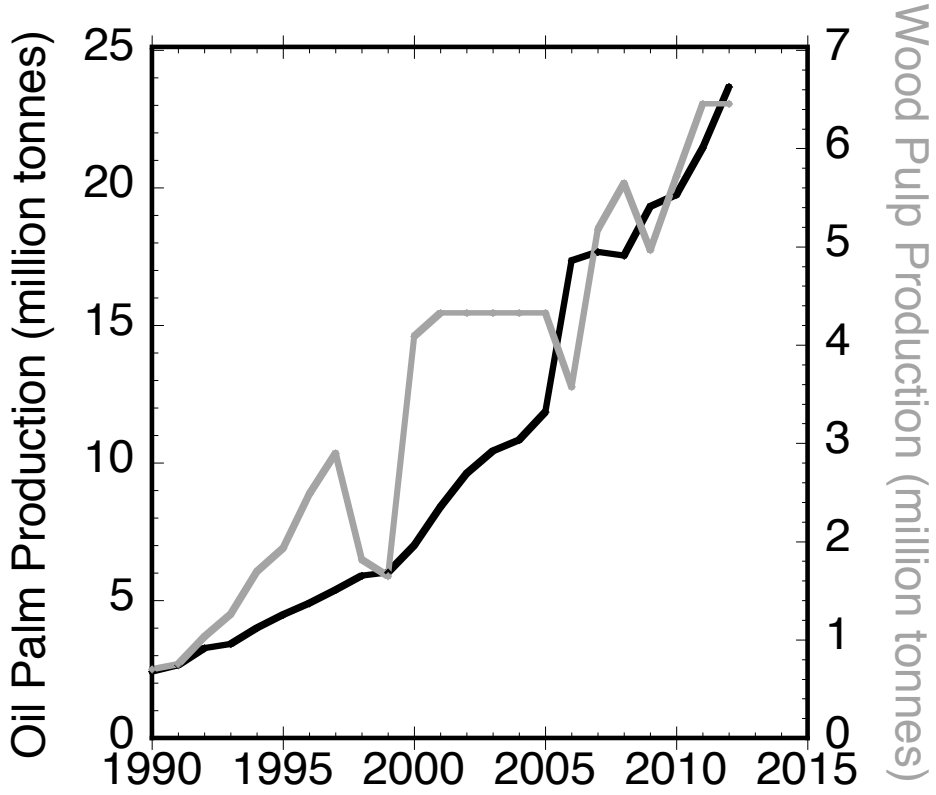

Figure 2. 2006 baseline land use map for Sumatra from the Indonesian Ministry of Forestry (MoF). Classes have been aggregated to 1-km^2 resolution and 15 primary classes.

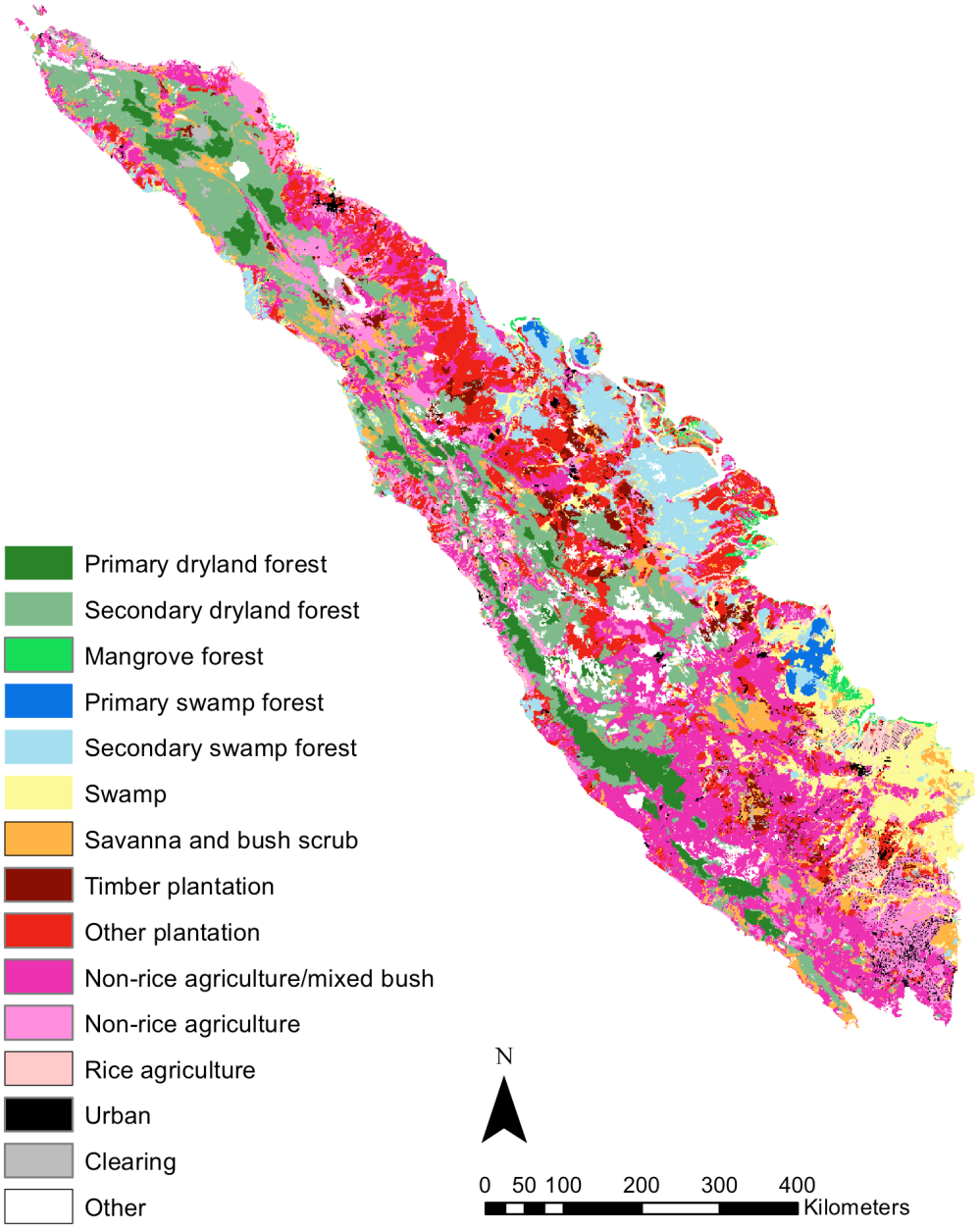

Figure 3. Combined maximum FRP (Aqua + Terra) for six selected transitions, normalized by the area of each land use transition type with fire observations (all transitions shown in Fig. S1). Normalized FRP given for selected transition (gray line) and sum of all other transitions (black line). Dryland forest includes primary and secondary dryland forests; peatswamp includes mangrove forests, peatswamp forests, and peatswamp; mixed scrub includes savanna and bush scrub, clearing, and urban; plantation includes timber and other plantations; agriculture includes non-rice agriculture with mixed bush, non-rice agriculture, and rice agriculture.

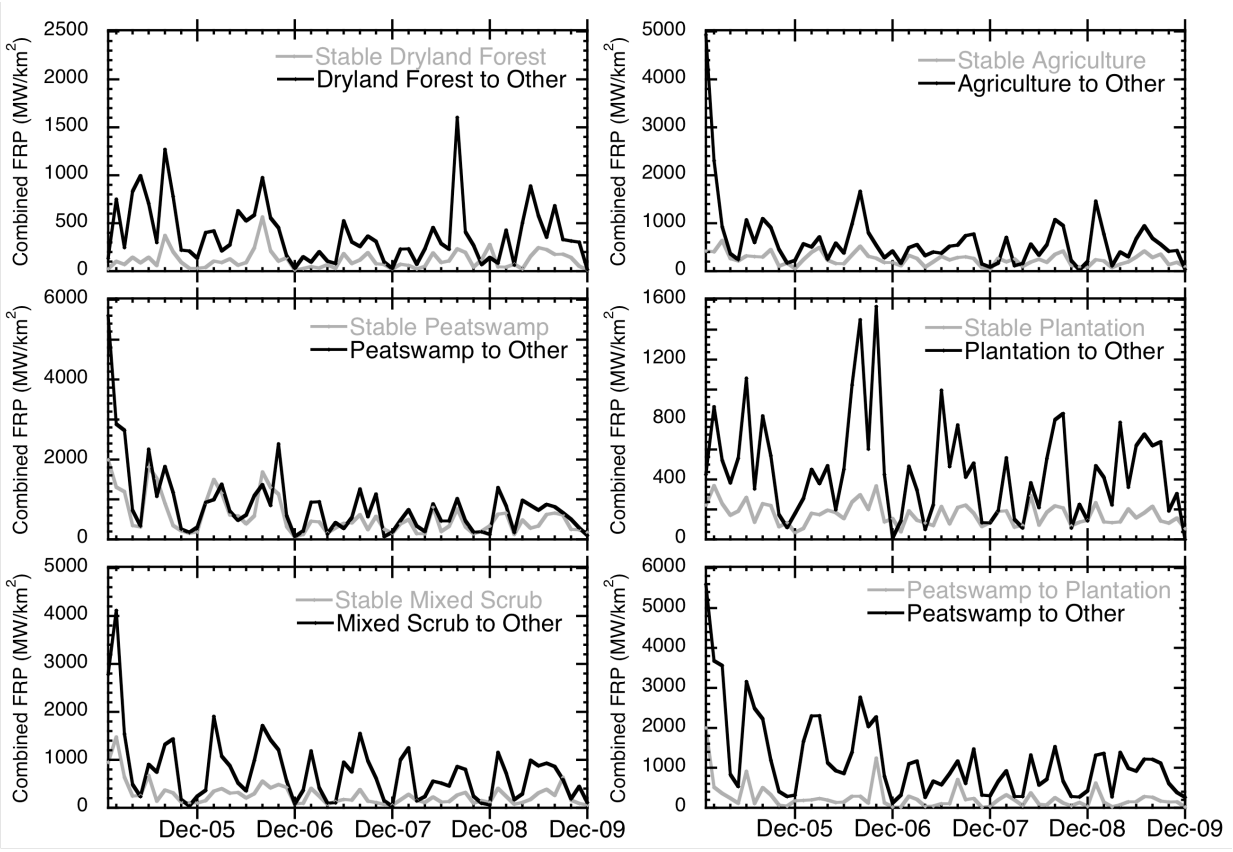

Figure 4. Fire mask from burned area product and active fire detections for 2006 (representative dry year) and 2010 (representative wet year). Area (km^2) from fire mask partitioned into specific land use groupings as in Table 1. Left column represents 2006 (transitions from these groupings based on 2006 land use); right column represents 2010 (transitions to these groupings based on 2009 land use).

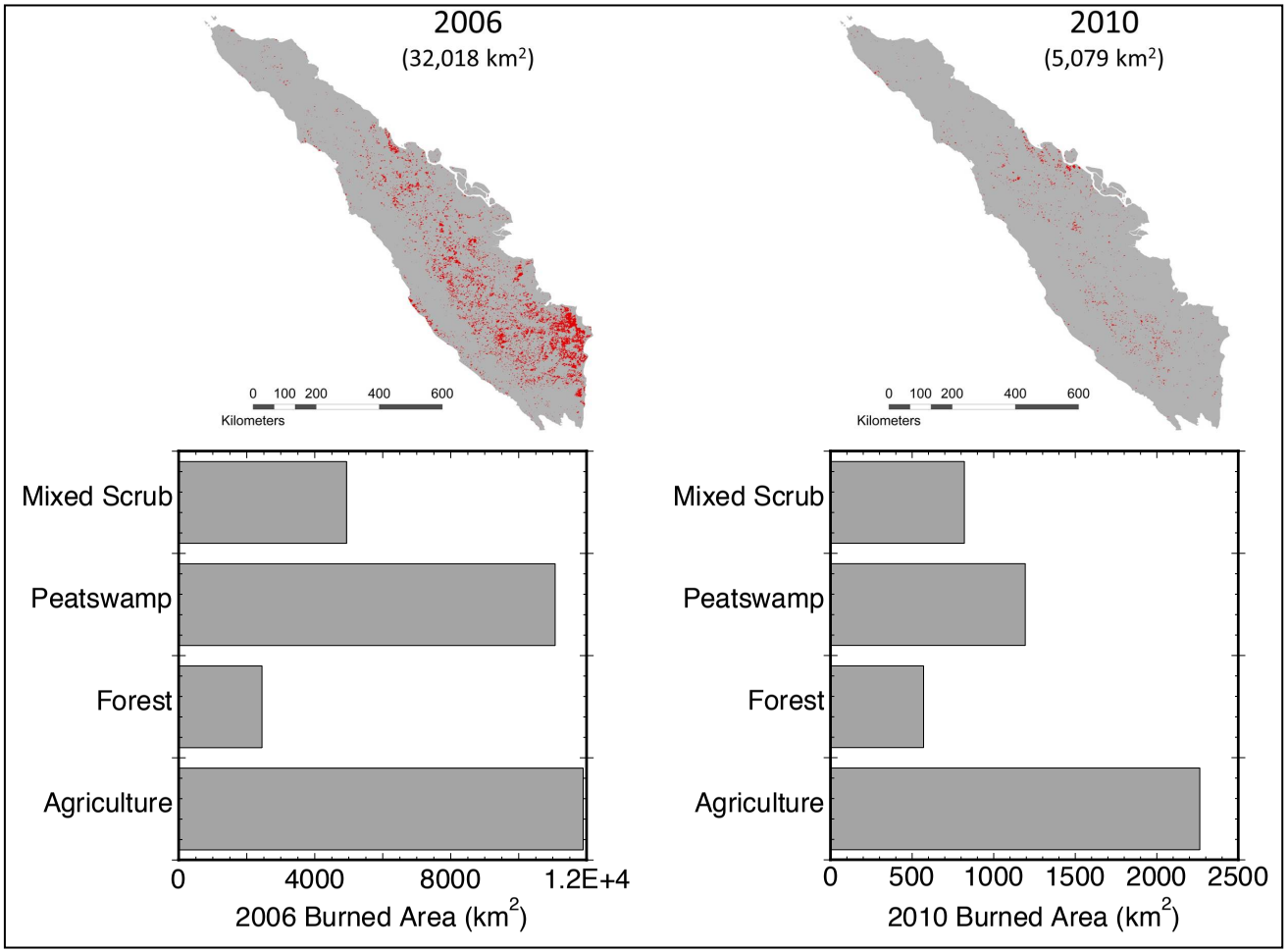

Figure 5. Sum of total Sumatra fire emissions for 2005 to 2009 (in Tg DM) from FRP-downscaled GFED emissions for land cover transition groupings described in Table 1. a) Annual sum, b) Sum for all years within a given month, and c) Emissions coming from original land use groupings in 2006 (x-axis) to land use groupings in 2009 (bars). Groupings as described in Figure 3 and Table 1.

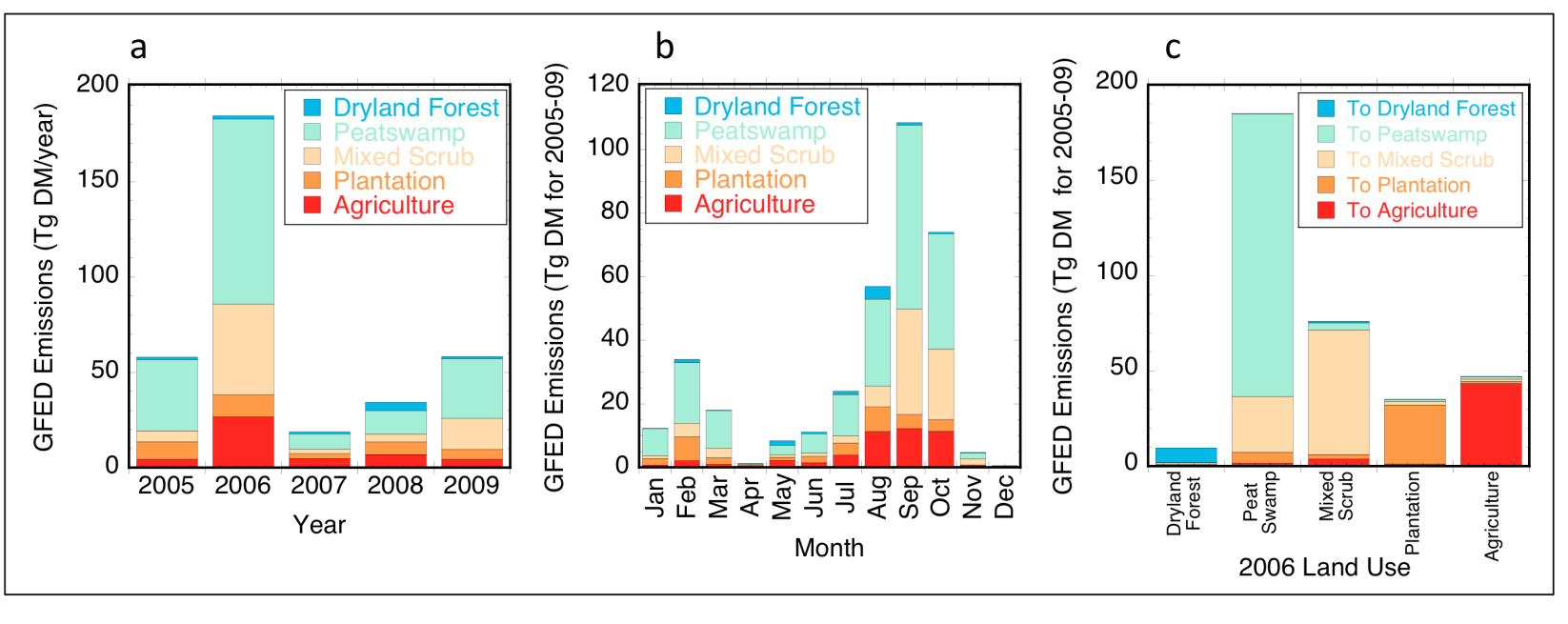

Figure 6. Total area (km^2) for Sumatra within each land use class, for 2006 to 2030: a) Stable Prices, b) National Spatial Plan, c) Green Vision, d) Peat Protection, and e) High Oil Palm. Land use groupings as in Table 1 except that all land use classes that contain oil palm (other plantation, non-rice agriculture with mixed brush, and clearing) are combined into Potential Oil Palm. Note change in scale of y-axis for Peat Protection (e).

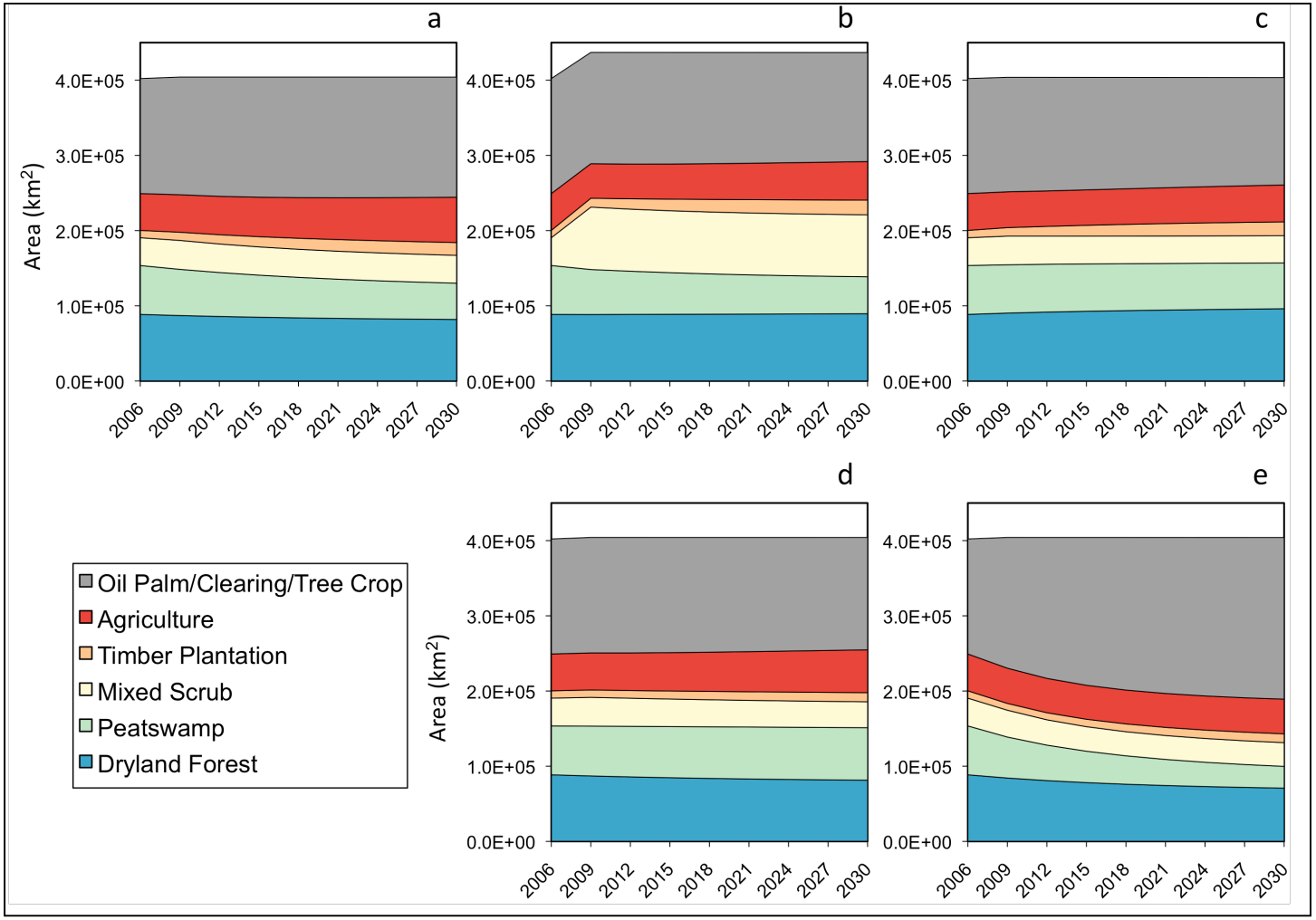

Figure 7. a) Fraction of forest cover – here defined as dryland forest, mangrove forest, peat forest, and peat – remaining in 2030 for five future scenarios (1) Stable Prices, 2) National Spatial Plan, 3) Green Vision, 4) Peat Protection, 5) High Oil Palm), and b) Cumulative total fire emissions for 2009 to 2030 (in Tg DM); darker colors represent more forest or higher emissions, respectively.

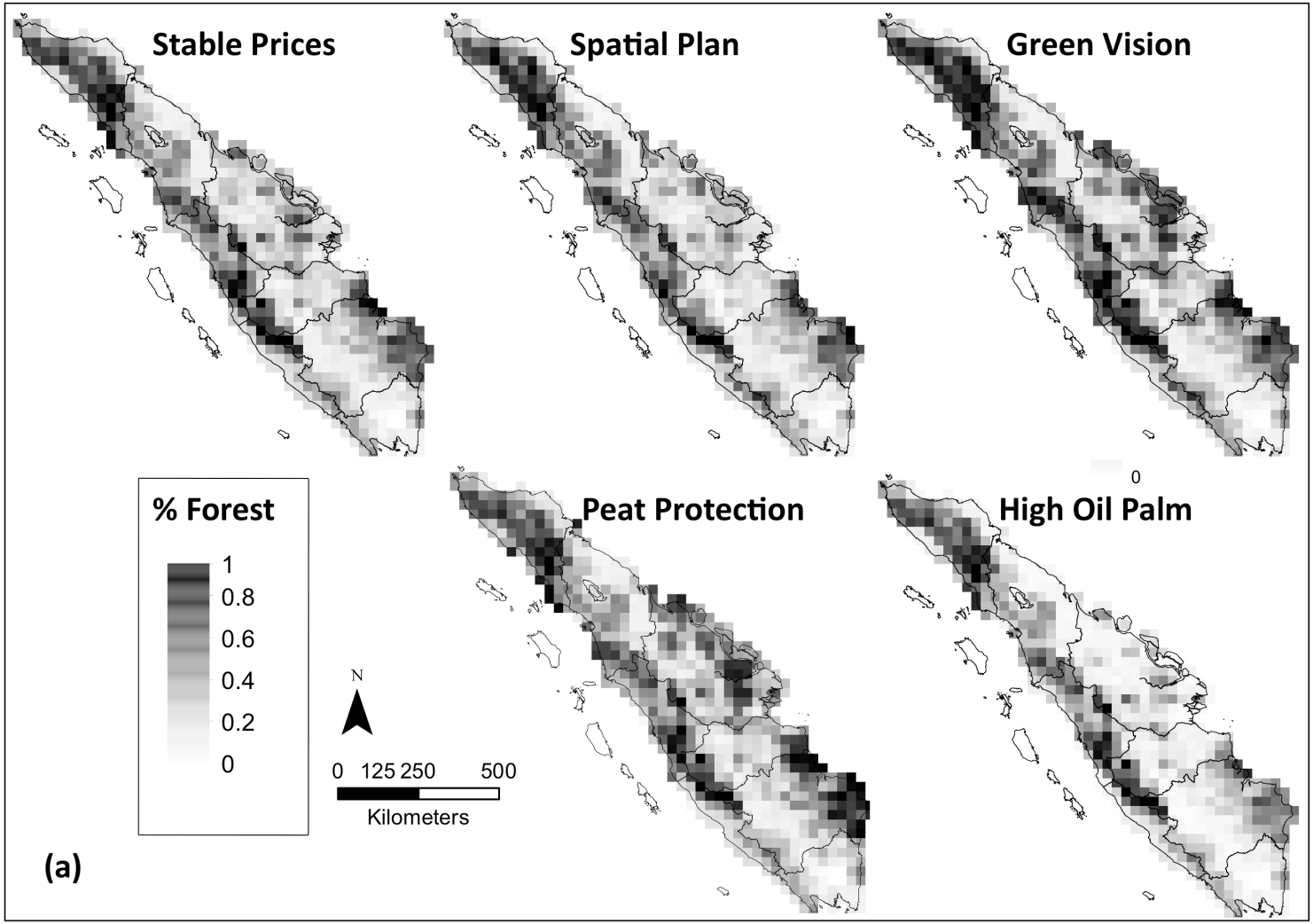

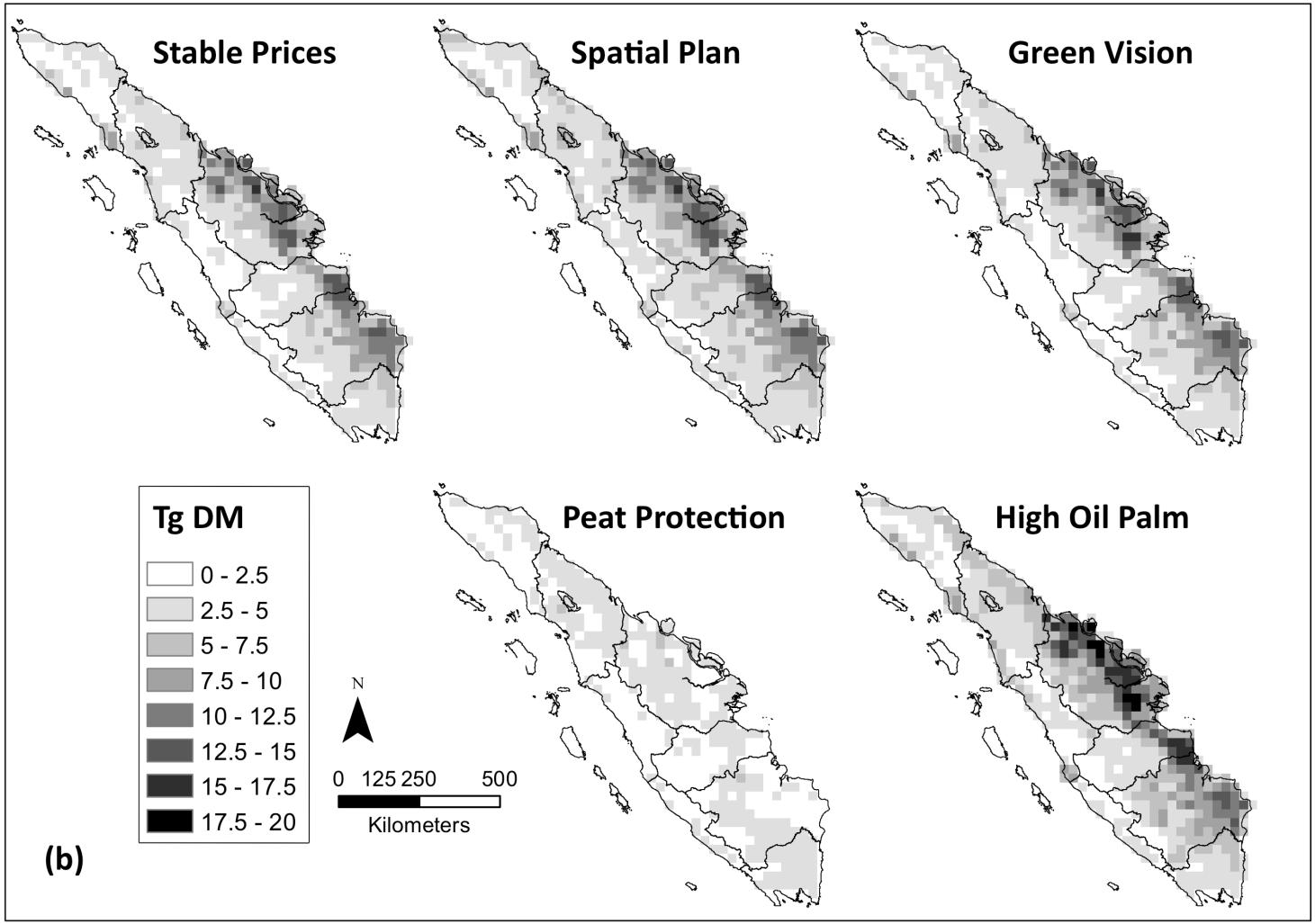
Stable Prices
Spatial Plan
Green Vision
Peat Protection
High Oil Palm
Tg DM
0 - 2.5
2.5 - 5
5 - 7.5
7.5 - 10
10 - 12.5
12.5 - 15
15 - 17.5
17.5 - 20
N
0 125 250 500
Kilometers
(b)

Figure 8. Total emissions (in Tg DM per three year timestep) for each scenario over 2009 to 2030.

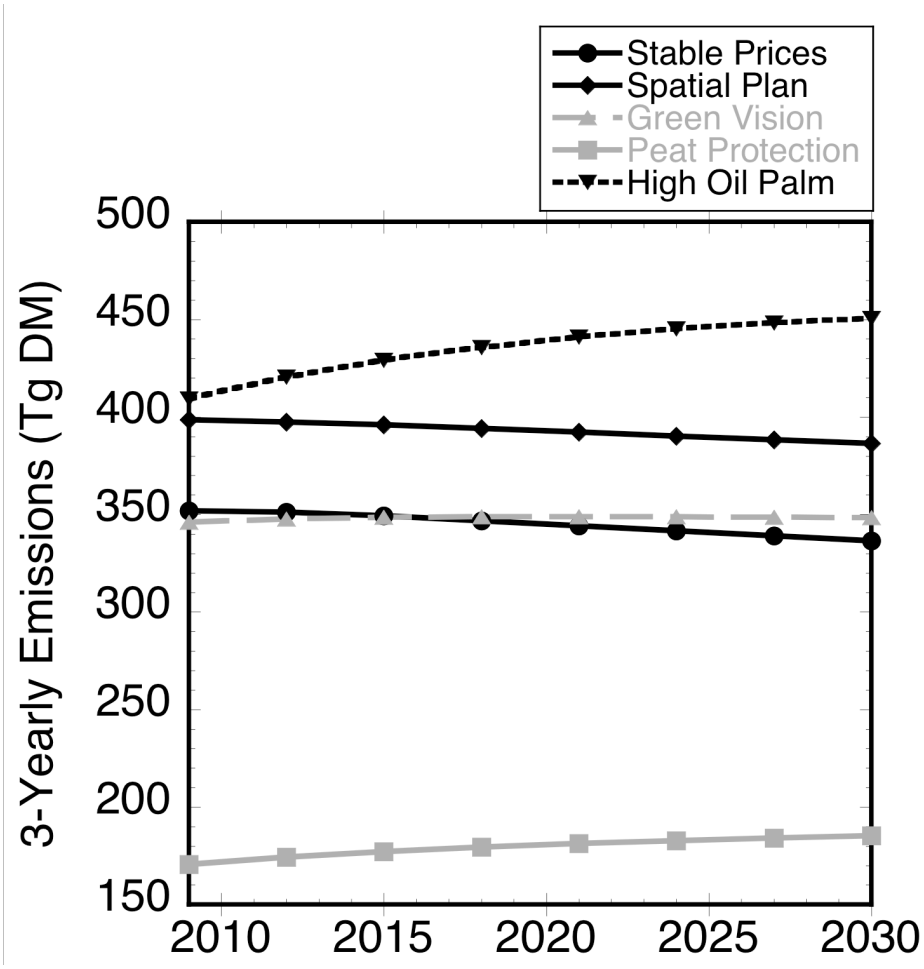

Figure 9. Emissions by fire type (Tg DM) for the High Oil Palm scenario when: a) partitioned according to relationships between fire emissions and meteorology observed over 2005 to 2009, b) assumed to be constant over each three-year time step, and c) sum of all fire types from (a) and (b). Fire type groupings as defined in Table 5, with DEF = deforestation, PET = peatland, SAV = savanna, WDL = woodland, and AGW = agricultural waste.

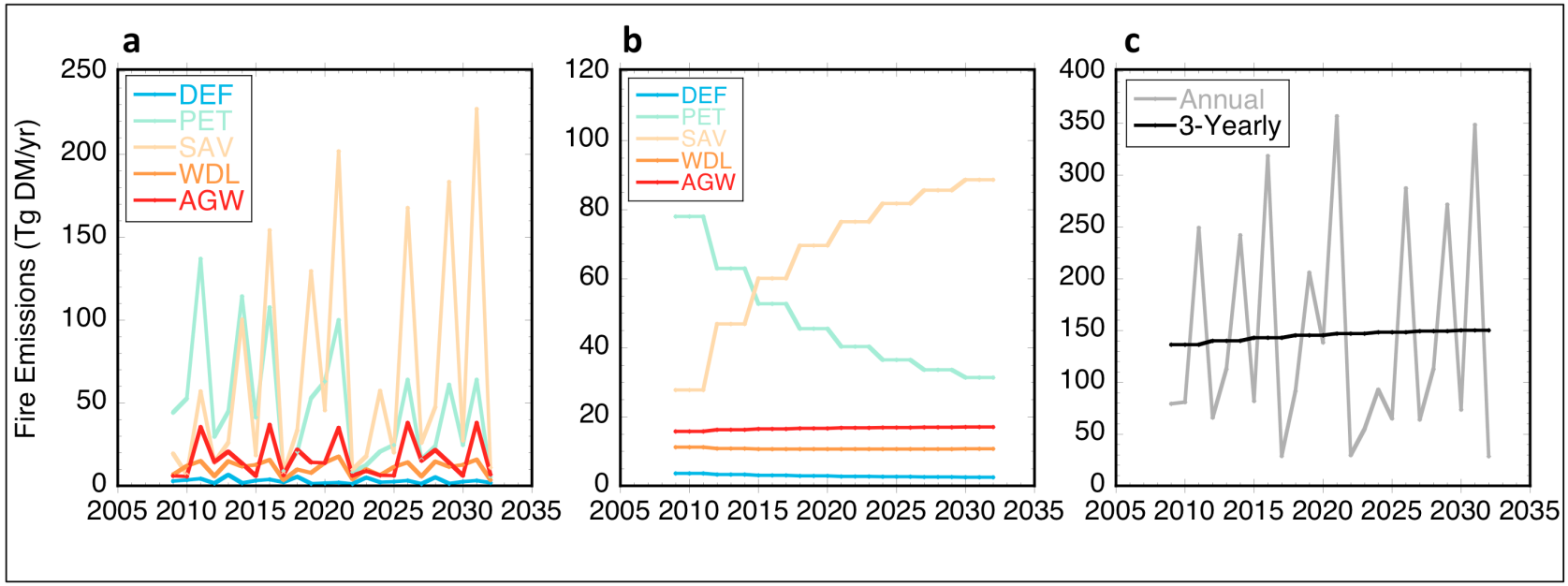

Supporting Information

Set-Up of Random Utility Model (RUM)

RUM land use change models require expected annual net revenue estimates for each potential land use on each pixel. However, spatially explicit annual net revenue data are difficult to attain for Indonesia. We could only calculate *district-level* expected annual *gross* revenues for each potential land use over the 2006 to 2009 time period. Therefore, we employed several model and data modifications to make our expected annual gross revenue values at the district level better proxies of the annual *net* revenue possibilities on each pixel. First, we included soil quality as an explanatory variable in the model such that soil quality has a separate effect on each land use category. If soil quality has an effect on agricultural revenues (and therefore affected agricultural choices between 2006 and 2009), our model will account for the soil's productivity effect and create diverse agricultural conversion probabilities within districts, despite a constant agricultural gross revenue value within the district. Second, we made the expected gross revenue from each land use possibility a separate explanatory variable. Therefore, the model could differentiate the impact that a marginal increase in gross revenues in each land use had on land use choice probabilities. Presumably, land uses will increase their probability of occurring for a given increase in gross revenues if lower than production costs, all else equal. Third, we included a dummy variable for each 2006 to 2009 land use transition possibility as a proxy for transition costs. This allows the model to codify which land use transitions are rare, all else equal. We assumed relative rarity means greater transition costs, all else equal [*Lubowski et al.*, 2006]. Fourth, we included each pixel's distance to the nearest city and coastal point as

an explanatory variable to control for the influence of distance to markets for both selling goods and buying production inputs. The effect of these distances on the cost of transporting a pixel's product to markets and importing productive inputs to the pixel also varied by land use choice, allowing us to estimate separate distance effects for each land use category. Finally, a pixel's expected net revenue from each land use possibility was affected by the pixel's zoning. For example, conversion of protected forest to oil palm plantation may result in fines and forced shutdowns in production (if the protected status is enforced), and therefore, negative net returns. An owner or user of a pixel in a protected area will consider the possibility of such punishment when making his land use choices. Therefore, we included each pixel's zoned use (including unrestricted, protected, logging concession, timber plantation, and tree-crop plantation types) in the RUM as well.

Since we do not know the exact crop distribution within each MoF land use category, revenue for the economic model was calculated at the provincial level as the weighted average of the most common crops within each category for 2004 to 2006 (in constant 2006 US$). Province-level yields and area of croplands and non-timber plantations were from the Indonesia Ministry of Agriculture and Budan Pusat Statistik (http://www.bps.go.id/eng/tnmn_pgn.php?kat=3), with average market prices per agricultural commodity from 2004 to 2006 (http://faostat.fao.org). Timber plantation yields were based on the harvestable volume per hectare of sawlog and pulpwood from the five largest company concession projects in Sumatra [*Maturana*, 2005]. Returns from long-term investments, such as oil palm or timber plantations, were annualized to account for unequal revenues over time.

The RUM of 2006 to 2009 pixel-level land use change on Sumatra was estimated with a multinomial logit specification [*Train*, 2009] found in the *mlogit* package for R [*Croissant*, 2010]. While the estimation procedure was performed over a random sample of pixels from the Sumatra landscape, we predicted *every* Sumatra pixel's 2006 to 2009 land use transition probabilities with the same data (e.g., soil quality, distance to city, gross revenue) we used to estimate the model. In other words, we estimated each pixel's likelihood of converting to each of the 10 possible land uses by 2009 given its 2006 land use (a pixel's vector of estimated transition probabilities where the sum of probabilities is one). Next, we grouped pixels from the same district that had identical initial (2006) land use, soil quality, and zoning categories to create an average transition possibility vector. This set of average transition possibility vectors is our "Stable Prices" transition matrix.

Table S1. Sensitivity analyses of area (km²) within each land use class in 2030 Stable Prices *scenario*: 1) Random parameterization of Random Utility Model (RUM) presented in the main paper, and 2) Grid parameterization of RUM.

Land Use Class	Random	Grid
Primary dryland forest	21175	19695
Secondary dryland forest	60673	59315
Peatswamp	48274	50198
Savanna and bush scrub	27877	36902
Timber plantation	17003	11620
Other plantation	50710	48918
Non-rice agriculture, mixed bush	93450	86140
Non-rice agriculture	29116	27933
Rice agriculture	31197	34223
Clearing	15591	20072
2009-30 Cumulative Emissions	**2761**	**2933**

Table S2. Sensitivity for cumulative total fire emissions (in Tg DM), by fire type, for Stable Prices scenario: 1) Stable Prices (presented in main results), 2) Overlaying 2006 to 2008 FRP only (instead of 2005 to 2009 in main results), 3) Scaling monthly emissions totals from our downscaled 1-km product to match observed monthly 0.25° GFED totals.

Land Use Class	Stable Prices	2006-08 FRP	Downscale Correction
Primary dryland forest	1	1	1
Secondary dryland forest	69	52	82
Peatswamp	1223	781	1410
Savanna and bush scrub	371	302	406
Timber plantation	77	61	90
Other plantation	217	119	263
Non-rice agriculture, mixed bush	247	208	282
Non-rice agriculture	80	60	92
Rice agriculture	75	62	83
Clearing	307	134	360
Urban	93	41	93
2009-30 Cumulative Emissions	**2761**	**1821**	**3162**

Table S3. Sensitivity analyses of area (km^2) within each land use class in 2030 and cumulative 2009-30 fire emissions (Tg DM) for Green Vision scenario: 1) Green Vision with no leakage effects (presented in main results), 2) Low Leakage with increases of 8% and 2.5% for local goods and global goods, respectively, and 3) High Leakage with increases of 15% and 10% for local goods and global goods, respectively.

Land Use Class	No Leakage	Low Leakage	High Leakage
Primary dryland forest	29113	28865	28522
Secondary dryland forest	67007	65121	62618
Peatswamp	60919	58259	52615
Savanna and bush scrub	27148	25745	24268
Timber plantation	18269	19132	22910
Other plantation	45461	43511	41930
Non-rice agriculture, mixed bush	84481	86871	87375
Non-rice agriculture	25608	31877	37930
Rice agriculture	23528	20668	15148
Clearing	12904	14380	21051
2009-30 Cumulative Emissions	**2786**	**2782**	**2861**

Table S4. Sensitivity analyses of area (km^2) within each land use class in 2030 and cumulative 2009-30 fire emissions (Tg DM) for Peat Protection scenario: 1) Peat Protection with no leakage effects (presented in main results), 2) Low Leakage with increase of 5% and 2.5% for local goods and global goods, respectively, and 3) High Leakage with increases of 15% and 8% for local goods and global goods, respectively.

Land Use Class	No Leakage	Low Leakage	High Leakage
Primary dryland forest	21298	21200	20996
Secondary dryland forest	60146	59186	57139
Peatswamp	69809	69270	68080
Savanna and bush scrub	25307	24601	23068
Timber plantation	12143	11949	11523
Other plantation	44926	43709	41094
Non-rice agriculture, mixed bush	90768	93103	97088
Non-rice agriculture	27299	31641	41488
Rice agriculture	29696	26980	21716
Clearing	13697	13451	12898
2009-30 Cumulative Emissions	**1435**	**1424**	**1401**

Table S5. Sensitivity analyses of area (km²) within each land use class in 2030 and cumulative 2009-30 fire emissions (Tg DM) for the National Spatial Plan scenario: 1) Government Plan with no leakage effects (presented in main results), 2) Low Leakage with increase of 5% and 2.5% for local goods and global goods, respectively, and 3) High Leakage with increases of 15% and 8% for local goods and global goods, respectively.

Land Use Class	No Leakage	Low Leakage	High Leakage
Primary dryland forest	24766	24641	24374
Secondary dryland forest	64722	63507	60859
Peatswamp	49138	47253	43017
Savanna and bush scrub	28003	27299	25709
Timber plantation	19519	19084	18036
Other plantation	44542	43808	42056
Non-rice agriculture, mixed bush	86106	87821	90325
Non-rice agriculture	25137	29051	37817
Rice agriculture	26159	23616	18668
Clearing	14403	16414	21634
2009-30 Cumulative Emissions	**3143**	**3159**	**3206**

Figure S1. Combined maximum FRP (Aqua + Terra), normalized by the area of each land use transition type with fire observations. Dryland forest includes primary and secondary dryland forests; Peatswamp includes mangrove forests, peatswamp forests, and peatswamp; Mixed scrub includes savanna and bush scrub, clearing, and urban; Plantation includes timber and other plantations; Agriculture includes non-rice agriculture with mixed bush, non-rice agriculture, and rice agriculture.

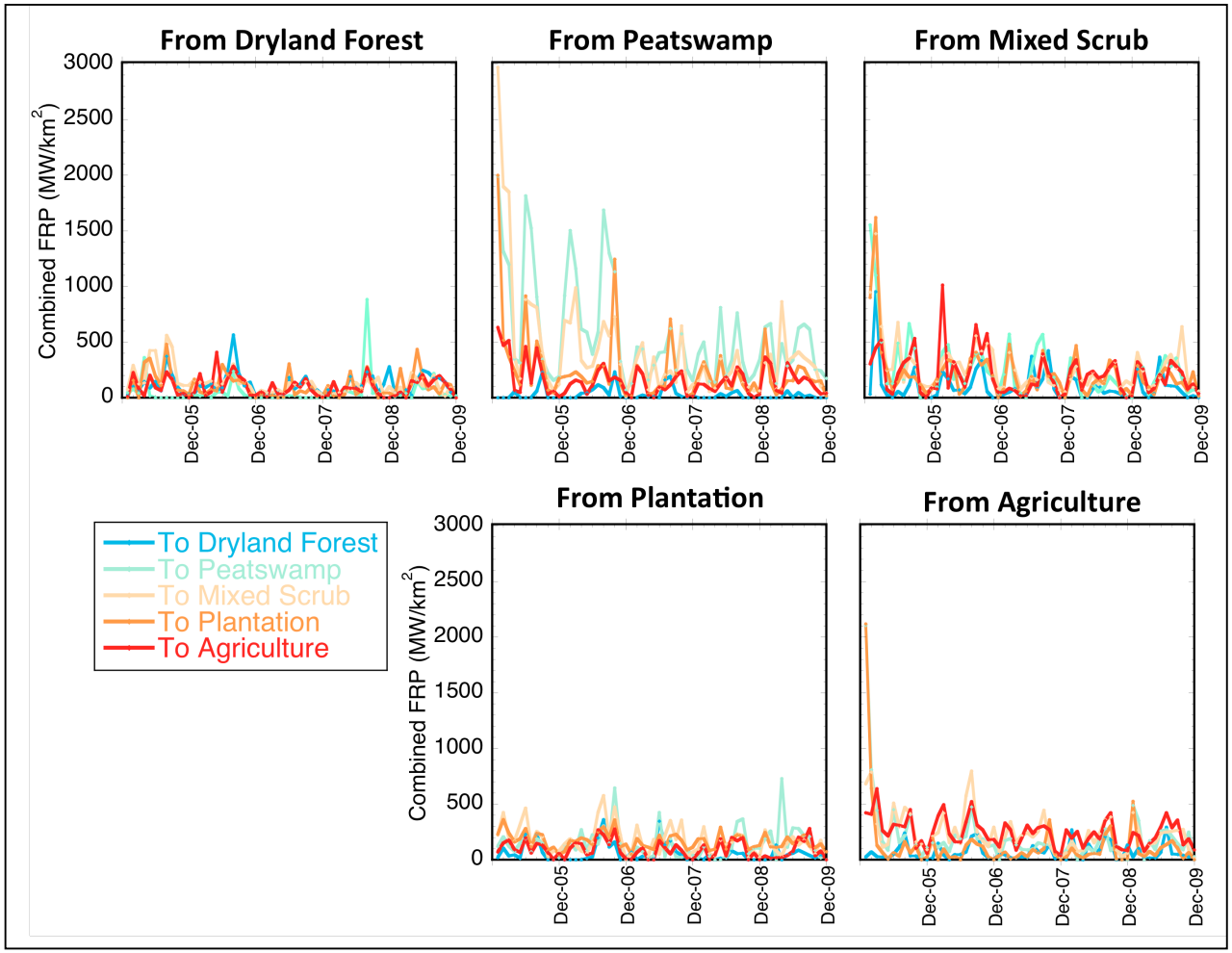

Figure S2. Total Sumatra monthly emissions (in Tg DM) for 2005 to 2009 for observed 0.25° GFED data (white) and for the downscaled 1-km emissions (gray).

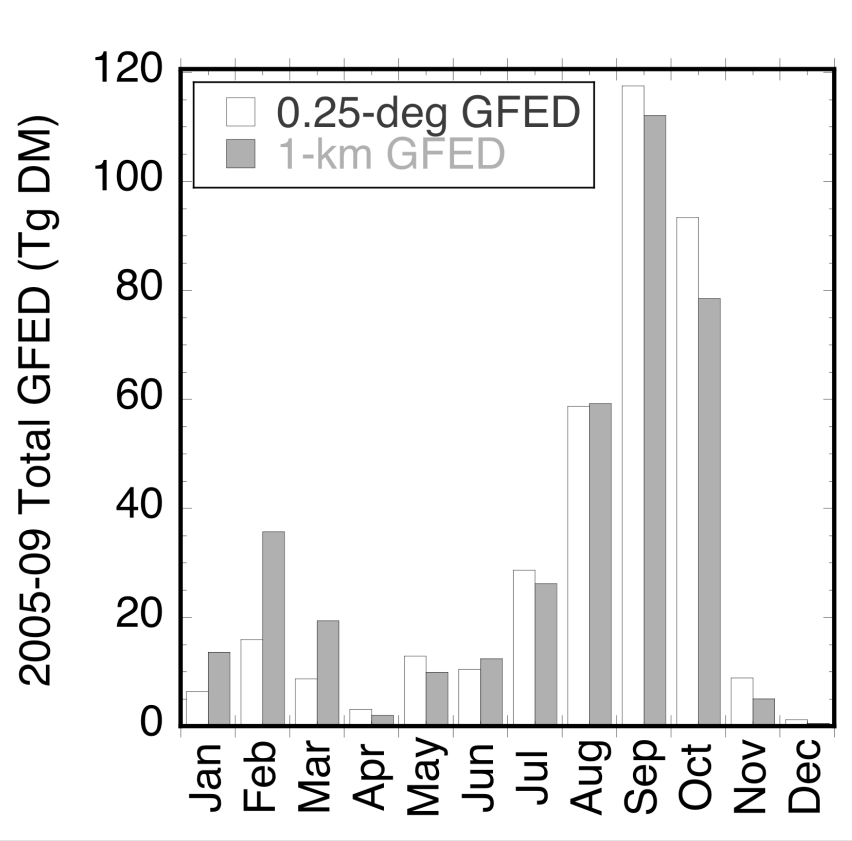

CHAPTER FIVE

Conclusions and Synthesis

The preceding chapters were linked by the general objectives of determining the spatial patterns of population exposure to outdoor air pollution from fire emissions, and how this exposure varies according to local climatic and ecosystem properties. These are fundamental considerations that must be taken into account when estimating future public health risks due to fires in the tropics and determining the best way to mitigate these negative impacts. A multidisciplinary approach, which combined satellite remote sensing, global atmospheric modeling, economic land use projections, and public health impacts, was critical to addressing these questions.

Chapter Two sought to understand how implementing GFED fire emissions inventories at differing temporal resolutions impacted model estimates of atmospheric composition, air quality, and climate. Results showed that model simulations of aerosols were more affected by using daily versus monthly resolution emissions than trace gases such as CO and O_3. Further exploration indicated that daily emissions datasets concentrated fire events over shorter time periods and allowed more realistic interactions with meteorology. This caused higher peak concentrations, which in turn can alter how models estimate population exposure over air quality thresholds. The effect was not constant throughout the tropics, but varied according to ecosystem properties, with larger differences between monthly and daily resolution fire emissions in regions dominated by intense, short-term deforestation fires as opposed to savanna regions that burn more

frequently with lower intensity. Overall, the temporal resolution of fire emissions can change how models estimate atmospheric composition, air quality, and atmospheric heating patterns attributable to fires. This is an important consideration when comparing studies that used different resolutions of fire input datasets, even if they are using the same overall emissions totals.

Understanding how population exposure to fire emissions in Equatorial Asia has changed over 1997 to 2008 was the focus of Chapter Three. Since only monthly resolution GFED emissions were available before 2000, this study was not able to utilize the daily resolution emissions described in the previous chapter. However, it was important to include the late 1990s in order to study the impact of the 1997-98 El Niño, which brought the most extreme drought conditions to Equatorial Asia since the 1980s. Results from two atmospheric model simulations showed how strong El Niño years can have fire contributions of up to 200 $\mu g/m^3$ $PM_{2.5}$ and 50 ppb O_3 near fire sources. This translated into 200 additional days per year over the World Health Organization 50 $\mu g/m^3$ 24-hour $PM_{2.5}$ air quality target, along with mortality increases that were in phase with dry conditions during the El Niño cycle. Overall, this chapter demonstrated that negative public health impacts are not only experienced by populations living near fire sources, but also by regional populations that are affected through the transport of fire pollution in the atmosphere.

Chapter Four focused on the Indonesian island of Sumatra, with the goals of quantifying fire emissions attributable to specific land use management and transition strategies and the effect of interannual climate variability on these relationships. Results showed that drier years had higher emissions contributions from unintentional fires

(emissions were not directly associated with conversion over the observed time period) and that peatswamp areas dominated the emissions totals for Sumatra, especially during periods with low precipitation. This confirms previous studies that have demonstrated how degraded peatswamp areas strongly contribute to total emissions and are also overwhelmingly associated with later conversion to plantations or agriculture. These results were then applied to five scenarios of development for Sumatra (present-day until 2030), which were developed through collaboration with economists and the World Wildlife Fund (WWF), in order to create projected fire emissions inventories. The future scenarios ranged from 1435-3480 Tg cumulative dry matter emissions over 2009 to 2030 and indicated that peatswamps are the most critical areas to target for conservation in order to reduce the public health burden in surrounding populations. These areas contributed 33-48% of total emissions in the four scenarios without strict peatswamp protection. In addition, since degraded peatswamps are highly susceptible to fires, these areas need to be protected from nearby fire sources, in addition to preventing further conversion of peatswamps to plantations or agriculture.

The work presented in Chapter Four is part of a broader project regarding the public health impacts associated with different development strategies for Sumatra; implementation of the future fire emissions inventories into the GEOS-Chem atmospheric model is currently in progress, as well as expanding our projections to other frontiers of plantation development in Indonesia, such as Kalimantan. In addition, there is planned work regarding specific policy interventions to help control fires in vulnerable land use management and transition types. We hope to build an online tool to assist policy makers

in decisions about the areas to target for conservation that would most effectively reduce exposure in nearby population centers.

While the results included in these chapters offer important insights into measuring the impacts of tropical fire emissions on regional population exposure, they also emphasize potential areas of future research. Chapter Two described how implementing monthly versus daily fire emissions in a global model can change our understanding of fire emissions behavior in the atmosphere, and future work should consider even finer temporal resolution (sub-daily) emissions and an alternative atmospheric model than was used in our study, such as GEOS-Chem, to confirm that our results are not limited to the GISS-E2-PUCCINI model. In Chapter Three, we used the best spatial resolution of atmospheric models available to us at the time (2 × 2.5°); future work could measure how finer resolution models that are currently in development can provide more refined estimates of population exposure. Finally, satellite observations of fire radiative power that were used to downscale GFED emissions in Chapter Four highlight the need for finer resolution emissions models in the tropics that can give more detailed estimates of the fire emissions associated with land use change and management strategies. This is currently in progress by the van der Werf research group at VU University in Amsterdam.

Results presented in the preceding chapters indicate that there are large differences in the public health burden due to fire emissions exposure related to interannual variations in meteorology; this warrants further research into the influence of future climate change on this relationship. First, global projections indicate that a warmer future climate will strongly influence fire activity during the 21st century, outweighing direct anthropogenic influence [*Pechony and Shindell*, 2010]. Second, although the trajectory of near-term

climate change in Equatorial Asia and its effect on El Niño is uncertain [*Collins et al.*, 2010], there is the potential to exacerbate the public health impact of fires if droughts become more frequent or intensified in the future, the latter as suggested by recent climate models predictions in the western Pacific Ocean [*Power et al.*, 2013]. Finally, in addition to future climate effects, shifts from communicable to non-communicable diseases in several high fire-affected regions would increase future baseline cardiovascular disease incidence rates, and therefore the overall magnitude of health impacts from exposure to air pollution from fire emissions [*Lim et al.*, 2012].

Taken together, the individual studies described in this dissertation provide important insights regarding how to measure the public health impact attributable to exposure to fire emissions and the spatiotemporal patterns of these effects. Global models are useful tools for estimating population exposure, but caution is necessary regarding setup parameters of the fire emissions inventories, which can affect model simulations of atmospheric composition and air quality, as well as intercomparisons among studies. The transport of fire emissions can expose broader regional populations, but also varies according to environmental constraints on fuel loads and interannual climate variability. By concentrating on direct human health impacts, these results provide additional motivation for protecting vulnerable ecosystems in the tropics by targeting the areas that will optimize public health exposure. As shown in this dissertation, estimating this impact on public health requires bringing together several disciplines; individually each component cannot address the full issue.

REFERENCES

Alexander, B., R. Park, D. Jacob, Q. Li, R. M. Yantosca, J. Savarino, C. C. W. Lee, and M. H. Thiemens (2005), Sulfate formation in sea-salt aerosols: constraints from oxygen isotopes, *J. Geophys. Res.*, *110*, D10307.

Andreae, M. O., and P. Merlet (2001), Emission of trace gases and aerosols from biomass burning, *Global Biogeochem. Cy.*, *15*(4), 955–966.

Anenberg, S. C., L. W. Horowitz, D. Q. Tong, and J. J. West (2010), An estimate of the global burden of anthropogenic ozone and fine particulate matter on premature human mortality using atmospheric modeling, *Environ. Health Persp.*, *118*(9), 1189–1195, doi:10.1289/ehp.0901220.

Atwood, S. A., J. S. Reid, S. M. Kreidenweis, L. E. Yu, S. V. Salinas, B. N. Chew, and R. Balasubramanian (2013), Analysis of source regions for smoke events in Singapore for the 2009 El Niño burning season, *Atmos. Environ.*, *78*(219-230), 1–35, doi:10.1016/j.atmosenv.2013.04.047.

Baccini, A. et al. (2012), Estimated carbon dioxide emissions from tropical deforestation improved by carbon-density maps, *Nature Clim. Change*, *2*(3), 182–185.

Ballhorn, U., F. Siegert, M. Mason, and S. Limin (2009), Derivation of burn scar depths and estimation of carbon emissions with LIDAR in Indonesian peatlands, *P. Natl. Acad. Sci. USA*, *106*(50), 21213.

Barano, T. et al. (2012), *A Green Vision for Sumatra*, The Natural Capital Project, WWF-US, and WWF-Indonesia.

Bell, M. L., F. Dominici, and J. M. Samet (2005), A meta-analysis of time-series studies of ozone and mortality with comparison to the National Morbidity, Mortality, and Air Pollution Study, *Epidemiology*, *16*(4), 436–445.

Benkovitz, C. M., M. T. Scholtz, J. Pacyna, L. Tarrason, J. Dignon, E. C. Voldner, P. A. Spiro, J. A. Logan, and T. E. Graedel (1996), Global gridded inventories of anthropogenic emissions of sulfur and nitrogen, *J. Geophys. Res.*, 29239–29253.

Bey, I., D. J. Jacob, R. M. Yantosca, J. A. Logan, B. Field, A. Fiore, Q. Li, H. Liu, L. J. Mickley, and M. G. Schultz (2001), Global modeling of tropospheric chemistry with assimilated meteorology- Model description and evaluation, *J. Geophys. Res.*, *106*(23), 23073–23095.

Boden, T. A., G. Marland, and R. J. Andres (2011), *Global, regional, and national fossil-fuel CO_2 emissions*, Carbon Dioxide Information Analysis Center, Oak Ridge National Laboratory, U.S. Department of Energy, Oak Ridge, Tenn., U.S.A.

Boersma, K. F., D. J. Jacob, H. J. Eskes, R. W. Pinder, J. Wang, and R. J. van der A (2008), Intercomparison of SCIAMACHY and OMI tropospheric NO_2 columns: Observing the diurnal evolution of chemistry and emissions from space, *J. Geophys. Res.*, *113*(D16), doi:10.1029/2007JD008816.

Bond, T. C., E. Bhardwaj, R. Dong, R. Jogani, S. Jung, C. Roden, D. G. Streets, and N. M. Trautmann (2007), Historical emissions of black and organic carbon aerosol from energy-related combustion, 1850–2000, *Global Biogeochem. Cy.*, *21*, GB2018, doi:10.1029/2006GB002840.

Bowman, D., J. Balch, P. Artaxo, W. J. Bond, J. M. Carlson, and M. A. Cochrane (2009), Fire in the Earth System, *Science*, *324*, 481–484.

Broich, M., M. Hansen, and F. Stolle (2011), Remotely sensed forest cover loss shows high spatial and temporal variation across Sumatera and Kalimantan, Indonesia 2000–2008, *Environ. Res. Lett.*, *6*, 014010.

Carlson, K. M., L. M. Curran, D. Ratnasari, A. M. Pittman, B. S. Soares-Filho, G. P. Asner, S. N. Trigg, D. A. Gaveau, D. Lawrence, and H. O. Rodrigues (2012), Committed carbon emissions, deforestation, and community land conversion from oil palm plantation expansion in West Kalimantan, Indonesia, *P. Natl. Acad. Sci. USA*, *109*, 7559–7564.

Carlson, K. M., L. M. Curran, G. P. Asner, A. M. Pittman, S. N. Trigg, and J. M. Adeney (2013), Carbon emissions from forest conversion by Kalimantan oil palm plantations, *Nature Clim. Change*, *3*, 283–287, doi:10.1038/nclimate1702.

Chen, Y., Q. Li, J. Randerson, E. Lyons, R. Kahn, D. Nelson, and D. Diner (2009), The sensitivity of CO and aerosol transport to the temporal and vertical distribution of North American boreal fire emissions, *Atmos. Chem. Phys.*, *9*(17), 6559–6580.

Christensen, J. H., and K. K. Kanicharla (2014), *Chapter 14: Climate phenomena and their relevance for future regional climate change*, IPCC AR5.

CIESIN (2005a), *Gridded Population of the World Version 3 (GPWv3): Population Grids. Palisades, NY: Socioeconomic Data and Applications Center (SEDAC), Columbia University.*, Palisades, NY. [online] Available from: http://sedac.ciesin.columbia.edu/gpw

CIESIN (2005b), *Gridded Population of the World: Future Estimates, 2015 (GPW2015): Population Grids. Palisades, NY: Socioeconomic Data and Applications Center (SEDAC), Columbia University.*, Palisades, NY. [online] Available from: http://sedac.ciesin.columbia.edu/gpw

Cohen, A. J., H. R. Anderson, B. Ostro, K. D. Pandey, M. Krzyzanowski, N. Kunzli, K. Gutschmidt, and C. A. I. Pope (2004), Urban air pollution, in *Comparative Quantification of Health Impacts: Global and Regional burden of Disease Due to Selected Major Risk Factors*, edited by M. Ezzati, A. D. Lopez, A. Rodgers, and C. J. L. Murray, pp. 1353–1434,

World Health Organization, Geneva.

Collins, M. (2005), El Niño- or La Niña-like climate change? *Clim. Dynam.*, *24*, 89–104.

Collins, M. et al. (2010), The impact of global warming on the tropical Pacific Ocean and El Niño, *Nat. Geosci.*, *3*(6), 391–397, doi:10.1038/ngeo868.

Croissant, Y. (2010), *Estimation of multinomial logit models in R: The mlogit Packages*, R package version 0.2-2. [online] Available from: http://cran. r-project. org/web/packages/mlogit/vignettes/mlogit.pdf

Crutzen, P. J., and M. O. Andreae (1990), Biomass burning in the tropics: Impact on atmospheric chemistry and biogeochemical cycles, *Science*, *250*, 1669–1678.

Dennis, R. A. et al. (2005), Fire, People and Pixels: Linking Social Science and Remote Sensing to Understand Underlying Causes and Impacts of Fires in Indonesia, *Hum. Ecol.*, *33*(4), 465–504, doi:10.1007/s10745-005-5156-z.

Dennis, R. A., and C. P. Colfer (2006), Impacts of land use and fire on the loss and degradation of lowland forest in 1983-2000 in East Kutai District, East Kalimantan, Indonesia, *Singapore J. Trop. Geo.*, *27*(1), 30–48, doi:10.1111/j.1467-9493.2006.00238.x.

Duncan, B. N., R. V. Martin, A. C. Staudt, R. Yevich, and J. A. Logan (2003), Interannual and seasonal variability of biomass burning emissions constrained by satellite observations, *J. Geophys. Res.*, *108 (D2)*.

Emmanuel, S. C. (2000), Impact to lung health of haze from forest fires: the Singapore experience, *Respirology*, *5*, 175–182.

Fairlie, T. D., D. J. Jacob, and R. J. Park (2007), The impact of transpacific transport of mineral dust in the United States, *Atmos. Environ.*, *41*(6), 1251–1266, doi:10.1016/j.atmosenv.2006.09.048.

Field, R. D., and S. S. P. Shen (2008), Predictability of carbon emissions from biomass burning in Indonesia from 1997 to 2006, *J. Geophys. Res.*, *113*, G04024, doi:10.1029/2008JG000694.

Field, R. D., G. R. van der Werf, and S. S. P. Shen (2009), Human amplification of drought-induced biomass burning in Indonesia since 1960, *Nat. Geosci.*, *2*(3), 185–188.

Frankenberg, E., D. McKee, and D. Thomas (2005), Health consequences of forest fires in Indonesia, *Demography*, *42*(1), 109–129.

Fuller, D. O., M. Hardiono, and E. Meijaard (2011), Deforestation Projections for Carbon-Rich Peat Swamp Forests of Central Kalimantan, Indonesia, *Environ. Manage.*, *48*(3), 436–447, doi:10.1007/s00267-011-9643-2.

Gaveau, D., L. Curran, G. D. Paoli, K. Carlson, P. Wells, A. Besse-Rimba, D. Ratnasari, and N. Leader-Williams (2012), Examining protected area effectiveness in Sumatra: importance of regulations governing unprotected lands, *Conserv. Lett.*, *5*, 142–148.

Giglio, L. (2007), Characterization of the tropical diurnal fire cycle using VIRS and MODIS observations, *Remote Sens. Environ.*, *108*(4), 407–421, doi:10.1016/j.rse.2006.11.018.

Giglio, L., J. T. Randerson, G. R. van der Werf, P. S. E. V. Kasibhatla, G. J. Collatz, D. C. Morton, and R. S. DeFries (2010), Assessing variability and long-term trends in burned area by merging multiple satellite fire products, *Biogeosciences*, *7*, 1171–1186.

Giglio, L., T. Loboda, D. Roy, B. Quayle, and C. Justice (2009), An active-fire based burned area mapping algorithm for the MODIS sensor, *Remote Sens. Environ.*, *113*(2), 408–420.

Goldammer, J. G. (2006), History of equatorial vegetation fires and fire research in Southeast Asia before the 1997–98 episode: A reconstruction of creeping environmental changes, *Mitig. Adapt. Strat. Glob. Change*, *12*(1), 13–32, doi:10.1007/s11027-006-9044-7.

Guenther, A., and C. Wiedinmyer (2007), *User's guide to the Model of Emissions of Gases and Aerosols from Nature (MEGAN)*, 2nd ed.

Guenther, A., C. Hewitt, D. Erickson, R. Fall, C. Geron, T. Graedel, P. Harley, L. Klinger, M. Lerdau, and W. McKay (1995), A global model of natural volatile organic compound emissions, *J. Geophys. Res.*, *100*(D5), 8873–8892.

Guenther, A., T. Karl, P. Harley, C. Wiedinmyer, P. Palmer, and C. Geron (2006), Estimates of global terrestrial isoprene emissions using MEGAN (Model of Emissions of Gases and Aerosols from Nature), *Atmos. Chem. Phys.*, *6*, 3181–3210.

Harris, N. L., K. Brown, M. Netzer, P. Gunarso, and T. J. Killeen (2013), *Projections of oil palm expansion in Indonesia, Malaysia and Papua New Guinea from 2010 to 2050*, edited by T. J. Killeen and J. Goon, RSPO, Kuala Lumpur.

Heald, C. L., D. J. Jacob, P. Palmer, M. Evans, G. W. Sachse, H. B. Singh, and D. R. Blake (2003), Biomass burning emission inventory with daily resolution: Application to aircraft observations of Asian outflow, *J. Geophys. Res.*, *108*(D21), 8811.

Heil, A., and J. G. Goldammer (2001), Smoke-haze pollution: A review of the 1997 episode in Southeast Asia, *Reg. Environ. Change*, *2*(1), 24–37.

Holben, B., T. Eck, I. Slutsker, D. Tanre, J. Buis, A. Setzer, E. Vermote, J. Reagan, Y. Kaufman, and T. Nakajima (1998), AERONET—A federated instrument network and data archive for aerosol characterization, *Remote Sens. Environ.*, *66*(1), 1–16.

Husar, R. B., J. D. Husar, and L. Martin (2000), Distribution of continental surface aerosol extinction based on visual range data, *Atmos. Env.*, *34*, 5067–5078.

Jaenicke, J., J. O. Rieley, C. Mott, P. Kimman, and F. Siegert (2008), Determination of the amount of carbon stored in Indonesian peatlands, *Geoderma*, *147*(3-4), 151–158, doi:10.1016/j.geoderma.2008.08.008.

Johnston, F. H., S. B. Henderson, Y. Chen, J. T. Randerson, M. Marlier, R. S. DeFries, P. Kinney, D. M. J. S. Bowman, and M. Brauer (2012), Estimated Global Mortality Attributable to Smoke from Landscape Fires, *Environ. Health Perspect.*, *120*(5), 695–701, doi:10.1289/ehp.1104422.

Jones, D. S. (2006), ASEAN and transboundary haze pollution in Southeast Asia, *Asia Eur. J.*, *4*(3), 431–446.

Kaiser, J. W. et al. (2012), Biomass burning emissions estimated with a global fire assimilation system based on observed fire radiative power, *Biogeosciences*, *9*(1), 527–554, doi:10.5194/bg-9-527-2012.

Koch, D., G. A. Schmidt, and C. V. Field (2006), Sulfur, sea salt, and radionuclide aerosols in GISS ModelE, *J. Geophys. Res.*, *111*(D06206), doi:10.1029/2004JD005550.

Koh, L. P., J. Miettinen, S. C. Liew, and J. Ghazoul (2011), Remotely sensed evidence of tropical peatland conversion to oil palm, *P. Natl. Acad. Sci. USA*, *108*, 5127–5132.

Krewski, D., M. Jerrett, R. Burnett, R. Ma, E. Hughes, Y. Shi, and M. Turner (2009), *Extended follow-up and spatial analysis of the American Cancer Society study linking particulate air pollution and mortality. HEI Research Report, 140*, Health Effects Institute, Boston.

Lamarque, J.-F. et al. (2010), Historical (1850–2000) gridded anthropogenic and biomass burning emissions of reactive gases and aerosols: methodology and application, *Atmos. Chem. Phys.*, *10*(15), 7017–7039, doi:10.5194/acp-10-7017-2010.

Langmann, B., B. Duncan, C. Textor, J. Trentmann, and G. R. van der Werf (2009), Vegetation fire emissions and their impact on air pollution and climate, *Atmos. Environ.*, *43*, 107–116.

Lawler, J., D. Lewis, E. Nelson, A. J. Plantinga, S. Polasky, J. Withey, D. Helmers, S. Martinuzzi, and V. Radeloff (n.d.), Projected land-use change impacts on ecosystem services in the U.S., in review, *P. Natl. Acad. Sci. USA*.

Lee, Y. H. et al. (2013), Evaluation of preindustrial to present-day black carbon and its albedo forcing from Atmospheric Chemistry and Climate Model Intercomparison Project (ACCMIP), *Atmos. Chem. Phys.*, *13*(5), 2607–2634, doi:10.5194/acp-13-2607-2013.

Lim, S. S. et al. (2012), A comparative risk assessment of burden of disease and injury attributable to 67 risk factors and risk factor clusters in 21 regions, 1990-2010: a systematic analysis for the Global Burden of Disease Study 2010, *The Lancet*, *380*, 2224–2260, doi:10.1016/S0140-6736(12)61766-8.

Lubowski, R. N., A. J. Plantinga, and R. N. Stavins (2006), Land-use change and carbon sinks: Econometric estimation of the carbon sequestration supply function, *J. Environ. Econ. Manage.*, *51*(2), 135–152, doi:10.1016/j.jeem.2005.08.001.

Margono, B. A., S. Turubanova, I. Zhuravleva, P. Potapov, A. Tyukavina, A. Baccini, S. Goetz, and M. C. Hansen (2012), Mapping and monitoring deforestation and forest degradation in Sumatra using Landsat time series data from 1990 to 2010, *Environ. Res. Lett.*, *7*, 034010, doi:10.1088/1748-9326/7/3/034010.

Marlier, M. E., R. S. DeFries, A. Voulgarakis, P. L. Kinney, J. T. Randerson, D. T. Shindell, Y. Chen, and G. Faluvegi (2013), El Niño and health risks from landscape fire emissions in southeast Asia, *Nature Clim. Change*, *3*, 131–136, doi:10.1038/nclimate1658.

Maturana, J. (2005), *Economic costs and benefits of allocating forest land for industrial tree plantation development in Indonesia*, CIFOR Working Paper No. 30, Bogor Barat, Indonesia.

Miettinen, J., A. Hooijer, C. Shi, D. Tollenaar, R. Vernimmen, S. C. Liew, C. Malins, and S. E. Page (2012a), Extent of industrial plantations on Southeast Asian peatlands in 2010 with analysis of historical expansion and future projections, *GCB Bioenergy*, doi:10.1111/j.1757-1707.2012.01172.x.

Miettinen, J., A. Hooijer, J. Wang, C. Shi, and S. C. Liew (2012b), Peatland degradation and conversion sequences and interrelations in Sumatra, *Reg. Environ. Change*, doi:10.1007/s10113-012-0290-9.

Miettinen, J., and S. C. Liew (2009), Burn-scar patterns and their effect on regional burnt-area mapping in insular South-East Asia, *Int. J. Wildland Fire*, *18*, 837–847, doi:10.1071/WF08102.

Miettinen, J., C. Shi, and S. C. Liew (2011), Deforestation rates in insular Southeast Asia between 2000 and 2010, *Glob. Change Biol.*, *17*, 2261–2270, doi:10.1111/j.1365-2486.2011.02398.x.

Miettinen, J., E. Hyer, A. S. Chia, L. K. Kwoh, and S. C. Liew (2013), Detection of vegetation fires and burnt areas by remote sensing in insular Southeast Asian conditions: current status of knowledge and future challenges, *Int. J. Remote Sensing*, *34*(12), 4344–4366, doi:10.1080/01431161.2013.777489.

MoF (2011), *Rekalkulasi Penutupan Lahan (Land Cover Recalculation) Indonesia Tahun 2009/2010 (Jakarta: Badan Planology Kehutanan Departemen Kehutanan Indonesia)*.

Mu, M., J. Randerson, G. R. van der Werf, L. Giglio, P. Kasibhatla, D. Morton, G. Collatz, R. DeFries, E. Hyer, and E. Prins (2011), Daily and hourly variability in global fire emissions and consequences for atmospheric model predictions of carbon monoxide, *J. Geophys. Res.*, *116*(D24303).

Naeher, L. P., M. Brauer, M. Lipsett, J. T. Zelikoff, C. D. Simpson, J. Q. Koenig, and K. R. Smith (2007), Woodsmoke health effects: a review, *Inhal. Toxicol.*, *19*(1), 67–106, doi:10.1080/08958370600985875.

Naidoo, R., T. Malcolm, and A. Tomasek (2009), Economic benefits of standing forests in highland areas of Borneo: quantification and policy impacts, *Conserv. Lett.*, *2*, 35–44.

NCDC (2010), *Global Surface Summary of Day*, 7 ed., National Climatic Data Center, Asheville. [online] Available from: http://www.ncdc.noaa.gov/cgi-bin/res40.pl?page=gsod.html

Nelson, E., D. Pennington, and J. Lewis (n.d.), Estimating Land Use Change in Sumatra, in preparation.

Olivier, J. G. J., and J. J. M. Berdowski (2001), Global emissions sources and sinks, in *The Climate System*, edited by J. Berdowski, R. Guicherit, and B. J. Heij, pp. 33–78, A.A. Balkema Publishers/Swets & Zeitlinger Publishers, Lisse, The Netherlands.

Ostro, B. (2004), *Outdoor air pollution: assessing the environmental burden of disease at national and local levels*, World Health Organization, Geneva.

Park, R. J., D. J. Jacob, B. D. Field, R. M. Yantosca, and M. Chin (2004), Natural and transboundary pollution influences on sulfate-nitrate-ammonium aerosols in the United States: implications for policy, *J. Geophys. Res.*, *109*, D15204, doi:10.1029/2003JD004473.

Pechony, O., and D. T. Shindell (2010), Driving forces of global wildfires over the past millennium and the forthcoming century, *P. Natl. Acad. Sci. USA*, *107*, 19167–19170.

Piccot, S. D., J. J. Watson, and J. W. Jones (1992), A global inventory of volatile organic compound emissions from anthropogenic sources, *J. Geophys. Res.*, *97*(D9), 9897–9912, doi:doi:10.1029/92JD00682.

Pope, C. A., R. T. Burnett, M. C. Turner, A. J. Cohen, D. Krewski, M. Jerrett, S. M. Gapstur, and M. J. Thun (2011), Lung cancer and cardiovascular disease mortality associated with ambient air pollution and cigarette smoke: shape of the exposure-response relationships, *Environ. Health Perspect.*, *119*, 1616–1621.

Power, S., F. Delage, C. Chung, G. Kociuba, and K. Keay (2013), Robust twenty-first-century projections of El Niño and related precipitation variability, *Nature*, *502*, 541–545, doi:10.1038/nature12580.

Price, C., J. Penner, and M. Prather (1997), NO_x from lightning 1. Global distribution based on lightning physics, *J. Geophys. Res.*, *102*(D5), 5929–5941, doi:10.1029/96JD03504.

Randerson, J. T., Y. Chen, G. R. van der Werf, B. M. Rogers, and D. C. Morton (2012), Global burned area and biomass burning emissions from small fires, *J. Geophys. Res.*, *117*(G4),

G04012, doi:10.1029/2012JG002128.

Rayner, N. A., D. E. Parker, E. B. Horton, C. K. Folland, L. V. Alexander, D. P. Rowell, E. C. Kent, and A. Kaplan (2003), Global analyses of sea surface temperature, sea ice, and night marine air temperature since the late nineteenth century, *J. Geophys. Res.*, *108*(D14), 4407, doi:10.1029/2002JD002670.

Reid, J. S. et al. (2009), Global Monitoring and Forecasting of Biomass-Burning Smoke: Description of and Lessons From the Fire Locating and Modeling of Burning Emissions (FLAMBE) Program, *IEEE Journal of Selected Topics in Applied Earth Observations and Remote Sensing*, *2*(3), 144–162, doi:10.1109/JSTARS.2009.2027443.

Rienecker, M. M. et al. (2011), MERRA: NASA's modern-era retrospective analysis for research and applications, *J. Climate*, *24*, 3624–3648, doi:10.1175/JCLI-D-11-00015.1.

Romijn, E., J. H. Ainembabazi, A. Wijaya, M. Herold, A. Angelsen, L. Verchot, and D. Murdiyarso (2013), Exploring different forest definitions and their impact on developing REDD+ reference emission levels: A case study for Indonesia, *Environ. Sci. Policy*, *33*, 246–259, doi:10.1016/j.envsci.2013.06.002.

Roosita, H., H. Waluyo, S. Bakar, B. E. Naiborhu, B. Karyaatmadja, D. Koespramoedyo, A. Karmarzuki, B. S. Sulistyanwan, E. Widodo, and C. Saleh (Eds.) (2010), *Roadmap towards ecosystem conservation of Sumatra: Sumatra Vision 2020*, Internal Affairs Department, Public Works Department, Forestry Department, Ministry of Environment, National Development and Planning Board, Coordinating Ministry of Economy Sector, Forum Tata Ruang Sumatera (ForTRUST).

Sakulyanontvittaya, T., T. Duhl, C. Wiedinmyer, D. Helmig, S. Matsunaga, M. Potosnak, J. Milford, and A. Guenther (2008), Monoterpene and sesquiterpene emission estimates for the United States, *Environ. Sci. Technol.*, *42*, 1623–1629.

Schmidt, A., B. Ostro, K. Carslaw, M. Wilson, T. Thordarson, G. W. Mann, and A. J. Simmons (2011), Excess mortality in Europe following a future Laki-style Icelandic eruption, *Proc. Natl. Acad. Sci. USA*, *108*(38), 15710–15715.

Shindell, D. T. et al. (2013a), Interactive ozone and methane chemistry in GISS-E2 historical and future climate simulations, *Atmos. Chem. Phys.*, *13*(5), 2653–2689, doi:10.5194/acp-13-2653-2013.

Shindell, D. T. et al. (2013b), Radiative forcing in the ACCMIP historical and future climate simulations, *Atmos. Chem. Phys.*, *13*(6), 2939–2974, doi:10.5194/acp-13-2939-2013.

Shindell, D. T., G. Faluvegi, N. Unger, E. Aguilar, G. A. Schmidt, D. M. Koch, S. E. Bauer, and R. L. Miller (2006), Simulations of preindustrial, present-day, and 2100 conditions in the NASA GISS composition and climate model G-PUCCINI, *Atmos. Chem. Phys.*, *6*, 4427–4459.

Siegert, F., G. Ruecker, A. Hinrichs, and A. A. Hoffmann (2001), Increased damage from fires in logged forests during droughts caused by El Niño, *Nature*, *414*(6862), 437–440.

Stolle, F., K. M. Chomitz, E. F. Lambin, and T. P. Tomich (2003), Land use and vegetation fires in Jambi Province, Sumatra, Indonesia, *For. Ecol. Manage.*, *179*(1), 277–292.

Textor, C., M. Schulz, S. Guibert, S. Kinne, Y. Balkanski, S. Bauer, and E. al (2007), The effect of harmonized emissions on aerosol properties in global models - an AeroCom experiment, *Atmos. Chem. Phys.*, *7*, 4489–4501.

Tosca, M. G., J. T. Randerson, C. S. Zender, D. L. Nelson, D. J. Diner, and J. A. Logan (2011), Dynamics of fire plumes and smoke clouds associated with peat and deforestation fires in Indonesia, *J. Geophys. Res.*, *116*, D08207, doi:10.1029/2010JD015148.

Tosca, M. G., J. T. Randerson, C. S. Zender, M. G. Flanner, and P. J. Rasch (2010), Do biomass burning aerosols intensify drought in Equatorial Asia during El Niño? *Atmos. Chem. Phys.*, *10*, 3515–3528.

Train, K. (2009), *Discrete choice methods with simulation*, Cambridge University Press.

UN (2011), *World Population Prospects: The 2010 Revision, CD-ROM Edition.*, Department of Economic and Social Affairs Population Division.

van der Werf, G. R. et al. (2008), Climate regulation of fire emissions and deforestation in equatorial Asia, *P. Natl. Acad. Sci. USA*, *105*, 20350–20355.

van der Werf, G. R., J. T. Randerson, L. Giglio, G. J. Collatz, M. Mu, P. S. Kasibhatla, D. C. Morton, R. S. DeFries, Y. Jin, and T. T. Van Leeuwen (2010), Global fire emissions and the contribution of deforestation, savanna, forest, agricultural, and peat fires (1997–2009), *Atmos. Chem. Phys.*, *10*(23), 11707–11735, doi:10.5194/acp-10-11707-2010.

Van Donkelaar, A., R. V. Martin, M. Brauer, R. Kahn, R. Levy, C. Verduzco, and P. Villeneuve (2010), Global estimates of ambient fine particulate matter concentrations from satellite-based aerosol optical depth: development and application, *Environ. Health Perspect.*, *118*, 847–855.

Voulgarakis, A. et al. (2013), Analysis of present day and future OH and methane lifetime in the ACCMIP simulations, *Atmos. Chem. Phys.*, *13*, 2563–2587, doi:10.5194/acpd-12-22945-2012.

Voulgarakis, A., P. J. Telford, A. M. Aghedo, P. Braesicke, G. Faluvegi, N. L. Abraham, K. W. Bowman, J. A. Pyle, and D. T. Shindell (2011), Global multi-year O_3-CO correlation patterns from models and TES satellite observations, *Atmos. Chem. Phys.*, *11*(12), 5819–5838, doi:10.5194/acp-11-5819-2011.

Wang, J., and S. A. Christopher (2006), Mesoscale modeling of Central American smoke transport to the United States: 2. Smoke radiative impact on regional surface energy

budget and boundary layer evolution, *J. Geophys. Res.*, *111*(D14S92), doi:10.1029/2005JD006720.

Wang, Y., D. J. Jacob, and J. A. Logan (1998), Global simulation of tropospheric O3-NO x-hydrocarbon chemistry 1. Model formulation, *J. Geophys. Res.*, *103*(D9), 10713–10725.

Wiedinmyer, C., S. K. Akagi, R. J. Yokelson, L. K. Emmons, J. A. Al-Saadi, J. J. Orlando, and A. J. Soja (2011), The Fire INventory from NCAR (FINN): a high resolution global model to estimate the emissions from open burning, *Geosci. Model Dev.*, *4*(3), 625–641, doi:10.5194/gmd-4-625-2011.

Wolter, K. (Ed.) (n.d.), *Multivariate El Niño Index*. [online] Available from: http://www.esrl.noaa.gov/psd/enso/mei/table.html (Accessed 30 October 2011)

Wooster, M. J., G. L. W. Perry, and A. Zoumas (2012), Fire, drought and El Niño relationships on Borneo (Southeast Asia) in the pre-MODIS era (1980–2000), *Biogeosciences*, *9*, 317–340, doi:10.5194/bgd-8-975-2011.

Wooster, M. J., G. Roberts, G. L. W. Perry, and Y. J. Kaufman (2005), Retrieval of biomass combustion rates and totals from fire radiative power observations: FRP derivation and calibration relationships between biomass consumption and fire radiative energy release, *J. Geophys. Res.*, *110*(D24), D24311, doi:10.1029/2005JD006318.

World Health Organization (2006), *WHO air quality guidelines for particulate matter, ozone, nitrogen dioxide and sulfur dioxide*, World Health Organization, Geneva.

World Health Organization, Department of Measurement and Health Information (2011), *Death estimates for 2008 by cause for WHO Member States*. [online] Available from: http://www.who.int/healthinfo/global_burden_disease/estimates_country/en/index.html

Wu, L., H. Su, and J. H. Jiang (2011), Regional simulations of deep convection and biomass burning over South America: 2. Biomass burning aerosol effects on clouds and precipitation, *J. Geophys. Res.*, *116*(D17), doi:10.1029/2011JD016106.

Yevich, R., and J. A. Logan (2003), An assessment of biofuel use and burning of agricultural waste in the developing world, *Global Biogeochem. Cy.*, *17*(4), 1095.